PHOTOEMISSION OF ANILINE OLIGOMER FILMS ON IRON OXIDE

PHOTOELECTRON SPECTROSCOPY INVESTIGATION OF OLIGOANILINE-IRON OXIDE INTERFACES FOR UNDERSTANDING CORROSION INHIBITION

BY

MARK GREINER, B.SC.

A Thesis

Submitted to the School of Graduate Studies

in Partial Fulfillment of the Requirements

for the Degree

Master of Science

McMaster University

MASTER OF SCIENCE (2007) McMaster University
(Chemistry) Hamilton, Ontario

TITLE: Photoelectron Spectroscopy Investigation of Oligoaniline-Iron Oxide Interfaces for Understanding Corrosion Inhibition

AUTHOR: Mark Greiner, B.Sc. (McMaster University)

SUPERVISOR: Peter Kruse

NUMBER OF PAGES: xi, 109

Abstract

Polyaniline (PANI) is capable of inhibiting corrosion on iron by inducing the formation of a passive oxide film. The mechanism by which PANI does this is unknown to the scientific community. We have used photoemission spectroscopy of thin films of a model PANI oligomer to investigate the PCAT-iron interaction.

The oligomer chosen was a phenyl-capped aniline tetramer (PCAT). Thin films of PCAT were prepared by in-vacuum physical vapor deposition to obtain extremely thin films of thickness ranging from ~5Å to over 10nm.

Films were investigated with a photoemission electron microscope (PEEM) using synchrotron radiation to obtain spatially resolved valence band photoemission spectra. Analysis of PEEM results suggest that PCAT is capable of migrating several microns along the substrate surface, and causes a decrease in substrate work function wherever present.

High-resolution core level and valence band photoemission spectroscopy using a laboratory-based photon source was used to characterize the substrate and PCAT properties near the PCAT-substrate interface. Characterization of an in-situ thin film deposition reveals that the iron substrate exhibits band bending in it oxide as well as a decrease in work function by 0.7eV upon adsorption of PCAT.

Acknowledgements

I would like to show my appreciation to my supervisor, Peter Kruse, for giving me the opportunity to perform this research. He has always been supportive of creative thinking and pioneering science. The skills I have acquired from working under him will be invaluable to my future as a scientist.

I would also like to thank the committee members for giving their time to referee this report and the oral defense. They have busy schedules and their commitment of time is very much appreciated.

I extend my gratitude to all those who assisted in the technical aspects of performing the experiments, especially Kirk Green, Andy Duft, Uday Lanke, Stephen Urquhart, Kevin Tsai, Dan Grozea, and Zheng Hong Lu. I would also like to thank Leighton Coatsworth, Peter Norton, and Brad Robinson for their equipment donations.

I appreciate all the help and support given by friends and lab mates; Sherdeep Singh, Ferdinand Gonzaga, Kevin Moonoosawmy, Miguel Festin, Warren Barden, Subir Gosh, Hany El-Sayed, Sung Kyun Lee, Goxiu Wei, and Gavin Pereira.

Finally, I would like to thank my family; my parents, my two brothers, my sister and Renita, who offered endless encouragement and support, even through the most difficult of times.

Table of Contents

List of acronyms

ACAT	Amino-Capped Aniline Trimer
AFM	Atomic Force Microscopy
CLS	Canadian Light Source
DOS	Density of States
DSC	Differential Scanning Calorimetry
EBSD	Electron Back-Scatter Diffraction
EDX	Energy-Dispersive X-rays
EELS	Electron Energy Loss Spectroscopy
FOV	Field of View
HOMO	Highest Occupied Molecular Orbital
ISC	Inorganic Semi-Conductor
LEED	Low-Energy Electron Diffraction
LUMO	Lowest Unoccupied Molecular Orbital
NMP	N-Methyl Pyrolidinone
NRA	Nuclear Reaction Analysis
OLED	Organic Light-Emitting Diode
OSC	Organic Semi-Conductor
PANI	Polyaniline
PCAD	Phenyl-Capped Aniline Dimer
PCAT	Phenyl-Capped Aniline Tetramer
PEEM	PhotoEmission Electron Microscopy
PES	Photoelectron Spectroscopy

PGM	Plane Grating Monochromator
PVD	Physical Vapor Deposition
QCM	Quartz Crystal Monitor
RBS	Rutherford Back-Scattering
SEM	Secondary Electron Microscopy
SIMS	Secondary Ion Mass Spectrometry
SKPM	Scanning Kelvin Probe Microscopy
SM	Spectro-Microscopy
STM	Scanning Tunneling Microscopy
TEM	Transmission Electron Microscopy
TP-MS	Temperature-Programmed Mass Spectrometry
UPS	Ultraviolet Photoemission Spectroscopy
XAS	X-ray Absorption Spectroscopy
XPS	X-ray Photoemission Spectroscopy
XRD	X-Ray Diffraction

List of figures and tables

Chapter 1 - Introduction

It was discovered in 1984 that the conductive polymer polyaniline (PANI) inhibits corrosion of iron when applied as an additive to surface coatings.[1] In the twenty three years since the discovery there have only been about 300 to 400 published works based on the topic, and while a few explanations of have been proposed still very little is known about why PANI inhibits corrosion. Most of the results are merely descriptive accounts or new formulations of PANI-epoxy coatings. Some have attempted to quantify PANI's corrosion inhibiting power using electrochemical measurements however these results have been irreproducible, with several studies giving contradictory results.[2] It seems that the PANI-Fe system is too complicated for routine electrochemical measurements, since it involves Fe, several iron oxides and oxy-hydroxides, several different oxidation forms of PANI and several different degrees of protonation of PANI.[2,3]

In spite of the difficulties inherent to studying this system there have been a few very interesting observations that make it seem worthwhile to examine. One such observation is that polypyrrole has also been found to inhibit corrosion.[2,4] Since both these polymers are nitrogen-containing, electro-active, and corrosion inhibiting one may wonder whether the three properties are interrelated.

Another interesting observation is that polyaniline coatings can remain corrosion inhibitive even when the coating has been scratched through to the underlying metal.[2,5,6,7,8,9] Conventional organic coatings used for corrosion control do not exhibit this property. They merely encapsulate the metal to isolate it from the corrosive surroundings.[10] If a conventional organic coating is damaged to expose the metal,

corrosion will initiate at the exposed metal surface, leading to rust growth across the metal-organic interface, and eventual de-lamination of the organic coating.

The observation that polyaniline can inhibit corrosion even when it is not fully covering the metal indicates it is chemically interacting with the metal, and draws similarities to the zinc coating on galvanized steel, which acts as a sacrificial anode when the underlying steel is exposed.[10] This property could potentially make PANI of great practical use in corrosion control, since it would exhibit similar corrosion protection as galvanizing, but would be much easier and cheaper to apply to metal surfaces. The ability of polyaniline to protect a metal even where it is not directly covering the metal will from here on be referred to as the 'remote effect'.

In addition to the 'remote effect' which gives PANI some practical importance, and indicates a chemical interaction between PANI and iron, there is another reported observation which makes the PANI-Fe system interesting to study. This observation is possibly the most significant result towards an understanding of the mechanism by which PANI inhibits corrosion. What was observed is the formation of a grey, passive iron oxide film underneath a PANI coating.[11] This observation shows that PANI induces the formation of a passive oxide and it is likely the result of some sort of chemical interaction between PANI and Fe or iron oxide.

As a result of the first observation of the passive oxide and several subsequent studies confirming the phenomenon, there is now a general consensus that the formation of this oxide is the reason for PANI's corrosion inhibition, however exactly how PANI induces the formation of the oxide is still in debate.[12,13,14] The group who first observed the passive oxide suggested that PANI catalyses the formation of the oxide by cycling

through it various oxidation forms while on the iron surface.[11] The belief is that PANI in its most oxidized form (emeraldine green) becomes reduced by oxidizing iron to its passive state. Then, while in its reduced state (pernigraniline purple) PANI becomes oxidized by atmospheric oxygen, to be recycled into its emeraldine form. While there is evidence to support this theory, such as the various colors observed during salt spray tests of PANI coatings on Fe[14] it is insufficient to explain the formation of a passive oxide.

Iron naturally forms an oxide when exposed to ambient conditions.[15] This oxide however is not passive (i.e. it is still prone to continual corrosion). Under certain electrochemical conditions an oxide can be grown that protects against further oxidation of Fe.[16] This can be done by applying an anodic potential to iron in an aqueous alkaline bath. If the potential is not sufficiently anodic then the iron will not passivate, it will simply continue to grow oxide (i.e. it will rust). Once the passivating potential is reached an oxide layer will form which prevents further oxidation.[15] This is called the passive oxide as opposed to the native oxide (i.e. the oxide naturally formed in ambient atmosphere). Little is actually known about the chemical and structural differences between the native[15,17-21] and passive[22-25] oxides of iron. In fact experiments have not been able to distinguish any structural differences.

Now it is evident where the 'catalytic oxidation' model of PANI's corrosion inhibition is lacking. If PANI were to merely catalyze constant oxidation of iron then it would just cause iron to continuously rust. Polyaniline must do something more in order to form the passive oxide instead of the 'native' oxide. Since electrochemical experiments show that iron passivates when the potential is sufficiently anodic it may be that PANI's

presence on the iron surface pushes iron's electrochemical potential into the passive regime.[26]

The phenomenon of chemical potential shifts at interfaces is well known from the research and development of semiconductor hetero-junction devices.[27,28] In fact recent research in semi-conducting organic hetero-junction devices such as organic light emitting diodes (OLED's) have also demonstrated several cases of chemical potential shifts at interfaces.[29-31] These studies were mostly aimed at interfaces between semi-conducting molecular organic (SCMO) materials and low work-function metals, and some studies on interfaces between SCMO's and inorganic semiconductors. Coincidentally the PANI-Fe system involves an interface between a conducting organic and an inorganic semi-conducting oxide (Fe_2O_3/Fe_3O_4).

While at first glance one might think that the interface of under consideration in the PANI-Fe system is a SCMO-metal interface, while in fact the system is a SCMO-inorganic semi-conducting oxide. Since all the studies reporting corrosion inhibition properties of PANI were carried out either in atmospheric or aqueous conditions,[1-9,11-15] the interface of interest is between PANI and the surface oxides of iron. Under atmospheric and aqueous conditions Fe is coated with an oxide, which is believed to be composed of an inner layer of Fe_3O_4 (a.k.a. magnetite) and an outer layer of Fe_2O_3 (hematite or maghemite depending on the crystal structure).[15,17-21] Magnetite is a semi-metal with a band gap of 0.1eV,[15] while hematite and maghemite are large-band-gap semi-conductors with band gaps around 2.2eV.[15]

The goals of the current work were to investigate the possibility of potential shifts at the PANI-Fe interface. Due to the similarities between this interface and the well-

studied interfaces of semi-conducting organic hetero-junction devices we chose to examine the PANI-Fe system using the same techniques used for studying the fundamental properties of hetero-junctions in OLED research.[29-31] These techniques are based around investigation of vacuum-prepared films with in-situ photoelectron spectroscopies such as X-ray photoelectron spectroscopy (XPS) and ultraviolet photoelectron spectroscopy (UPS). We also chose to use a technique which incorporates photoelectron spectroscopy with microscopic spatial mapping called photoelectron emission microscopy (PEEM). With this technique we hoped to identify spectroscopic evidence of the 'remote effect'.

Chapter 2 – Background

The following sections will discuss in more detail the known properties of the components in the system under study, some of the theory of interface electronic structure, as well as some of the phenomena observed in this system and the techniques used to study interfaces.

2.1 – The iron oxides which form on iron surfaces

There are several oxides and oxy-hydroxides which can form on iron either by solid state reactions or by precipitation of oxidized iron species. Here only the oxides commonly found on air-oxidized iron surfaces and electrochemically passivated surfaces will be discussed. These oxides are FeO (wüstite), Fe_3O_4 (magnetite), α-Fe_2O_3 (hematite), and γ-Fe_2O_3 (maghemite). The above are listed in order of oxidation of iron species going from least oxidized to most oxidized. Wüstite contains iron only in its +2 oxidation state, magnetite contains both +2 and +3 oxidation states of iron, and both hematite and maghemite contain iron only in its +3 state.

Name	Formula	Crystal structure	Oxygen packing	Fe oxidation state	Band gap (eV)
Wüstite	FeO	Rock salt	ccp	II	2.3
Magnetite	Fe_3O_4	Inverse spinel	ccp	II and III	0.1
Maghemite	γ-Fe_2O_3	Defect spinel	ccp	III	2.0
Hematite	α-Fe_2O_3	Corundum	hcp	III	2.2

Table 2.1 – Summary of iron oxide properties[15]

Wüstite, hematite and maghemite are all large-band-gap semiconductors, while magnetite is considered a semimetal. The band gaps of the oxides FeO, α-Fe_2O_3, and γ-Fe_2O_3 are 2.3, 2.2 and 2.0eV respectively, while the band gap of Fe_3O_4 is only 0.1eV.[15]

The crystal structures of FeO, Fe_3O_4 and γ-Fe_2O_3 are quite similar. All of them consist of a cubic close packed (ccp) O^{2-} lattice.[15] Wüstite (FeO) has the rock salt (NaCl) structure, where all the octahedral sites of the ccp O^{2-} lattice are occupied by Fe^{2+} and none of the tetrahedral sites are occupied.[15] Magnetite (Fe_3O_4) has the inverse spinel structure. The unit cell consists of a ccp array of 32 O^{2-} ions. This unit cell has 32 octahedral sites and 64 tetrahedral sites. In magnetite eight of the tetrahedral sites are occupied by Fe^{3+}, eight of the octahedral sites are occupied by Fe^{3+} and eight of the octahedral sites are occupied by Fe^{2+}.[22]

Maghemite (γ-Fe_2O_3) has a defect spinel structure, whose unit cell also consists of a ccp array of 32 O^{2-} ions. In maghemite eight tetrahedral sites are occupied by Fe^{3+} and the octahedral sites are randomly occupied, with on average 13.33 of the sites in the unit cell occupied by Fe^{3+}.[22]

Hematite (α-Fe_2O_3) in contrast, has the corundum crystal structure, with a hexagonal close packed (hcp) O^{2-} lattice, where two thirds of the octahedral sites are occupied by Fe^{3+}.[15]

The explanation of iron oxide electronic properties has been somewhat of a challenge for theorists. Band theory incorrectly predicts the large-band-gap oxides to be metallic, while localized molecular orbital picture does not explain the semi-conducting properties of these oxides.[32,33] It is believed that the problem lies in electron correlation effects and the difficulty for modern calculations to deal with these effects.[32-34] The large band gap oxides were originally believed to be Mott-Hubbard insulators, but recently there has been evidence to suggest that they are charge transfer insulators.[34,35] Magnetite

however is believed to be a semi-metal due to efficient electron hopping between nearby Fe^{2+} and Fe^{3+} sites.[15]

A simple descriptive picture of hematite has been derived from crystal field theory which indicates that the conduction band of hematite is composed of a band of empty Fe d orbitals, and a valence band consisting mainly of filled crystal field Fe3d-O2p orbitals, with some admixture of fill O 2p non-bonding orbitals.[15] For all the oxides it is believed that the Fe 3d electrons are mostly located on Fe centers.[15]

More recent theories about the electronic properties of iron oxides use a combination of band theory with crystal field theory and coulomb correlation energy from Mott-Hubbard theory.[35] This theory treats the oxygen component of the electronic structure as band-like, while it uses crystal-field theory to treat the iron component. This model accurately accounts for valence photoelectron spectra and asserts that large-band-gap iron oxides are in fact charge-transfer insulators.

2.2 – The layered structure of native and passive oxide films

The concept of a layered oxide on iron surfaces is fairly well established. It is was first proposed that the metal side of the film, where the oxygen chemical potential is small the oxide contains iron in its lower oxidation state, Fe^{2+}, and on the atmosphere side of the film, where the oxygen chemical potential is large the oxide contains iron is in its higher oxidation state, Fe^{3+} (see figure 2.1).[15] Therefore a model of the layered oxide was proposed, which has FeO on the metal side, Fe_3O_4 in the middle of the film, and either α- or γ-Fe_2O_3 on the atmosphere side. Over the years there has been plenty of evidence to support this model[21,37,38] however some subtleties still remain in dispute.

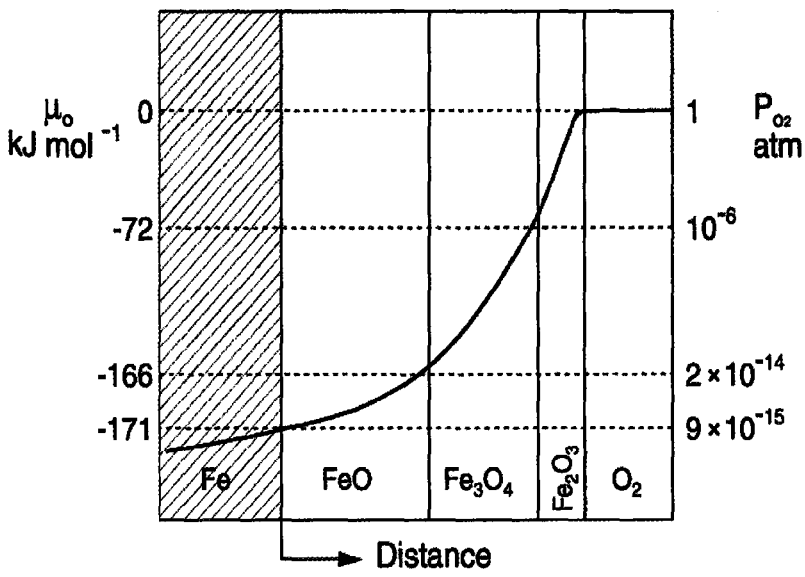

***Figure 2.1** – Plot of oxygen chemical potential through an oxide layer formed on the surface of iron at 1000°C [ref. 15]*

Most of the fundamental studies of the oxide film structure have been performed in vacuum by dosing iron surfaces with small pressures of oxygen,[37,38] and the results may not necessarily translate to a film formed in ambient atmosphere, however there is indication that the structures are fundamentally the same. Various techniques ranging from XPS,[18,19,20,40] UPS,[41,47] AFM,[42] STM,[20,43,44,49,50] TEM[36,45] low energy electron diffraction (LEED),[44,49] nuclear reaction analysis (NRA),[19,38] secondary ion mass spectrometry (SIMS),[46,48] and Rutherford backscattering (RBS)[38] have been used to examine this oxide. One can piece together the results of various studies to form a model of the layered oxide, which might form in air. It would consist of an inner monolayer of FeO, followed by a thicker layer of Fe_3O_4 and an outer layer of γ-Fe_2O_3 as shown in figure 2.2.

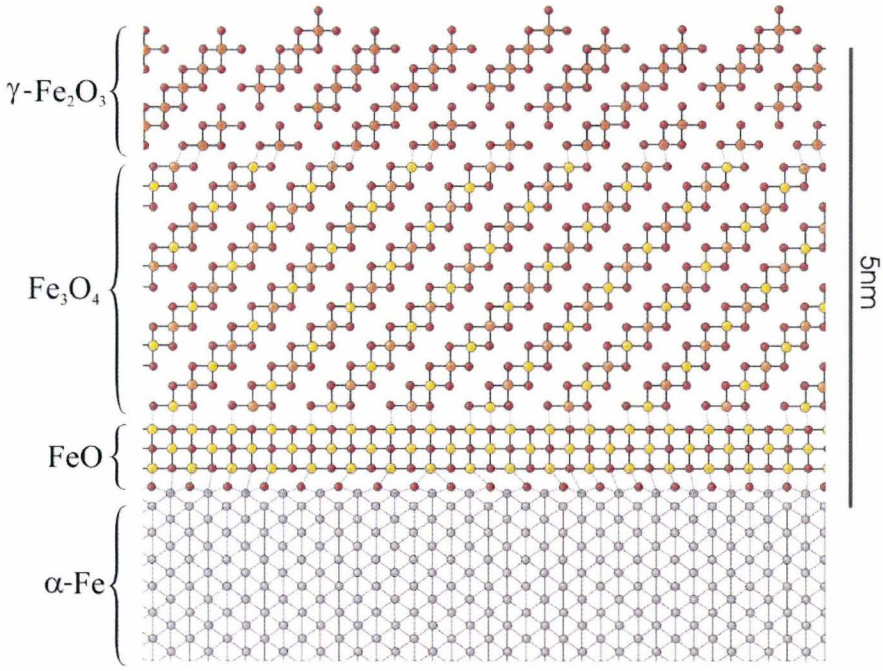

Figure 2.2 *– The proposed layered structure for the electrochemically formed passive oxide. Only the (100) plane of the oxides are shown. The lattice parameters are all drawn proportional to each other. The mis-match in lattice parameter is likely the cause of the nano-crystallinity.*

The relative thicknesses of the Fe_3O_4 and γ-Fe_2O_3 layers are unknown, but some have suggested that the ratio of their thicknesses remains constant.[15] The overall thickness depends on the temperature under which the oxide forms, possibly also on the relative humidity, but the film thickness saturates at room temperature when it reaches a thickness of only about 2-3nm.[51] The oxide is also nano-crystalline with no orientational preference parallel to the iron substrate, but possibly some order in the direction perpendicular to the substrate.

The structure of the electrochemically-formed passive oxide has been studied more conclusively than the air-formed oxide.[22,23,25,52] The bench-mark passive oxide is the one that is formed anodically in borate buffer.[23,25,53] While this oxide has been studied with many of the same techniques used to study the air-formed oxide, the most conclusive study yet used glancing angle X-ray diffraction, and actually determined the crystal structure and epitaxial relationship of the passive oxide.[23,25] Their study showed an inner layer of Fe_3O_4 and an outer layer similar to γ-Fe_2O_3 but with some disorder. There is still the possibility of an extremely thin FeO layer at the metal-oxide interface, which would have gone unnoticed in the XRD study. The film was nano-crytalline, with a slight orientational preference parallel to the substrate surface. The film was about 4nm thick and crystallite diameters were about 5-8nm in diameter.

While quite a bit is known about the layered structure of thin oxides that form on iron there is still much to be determined. The difference between the air-formed oxide and the electrochemically-formed passive oxide is still not clear. One should do a careful comparative study of their structures using glancing angle XRD in combination with neutron reflectometry, since it seems that XPS and SIMS have been unable to draw a structural distinction between the two oxides.

2.3 – Electronic structure of surfaces and interfaces

In order to explain the electronic properties of the oxide-PANI interface it is useful to use some concepts derived from surface and interface physics. A few of these useful concepts will be briefly reviewed in the following sections.

2.3.1 - The work function

The work function is a property that is unique to condensed phases. It is defined as the energy required to take an electron from the Fermi level to the vacuum *just outside* the surface of a solid.[30] The meaning of the term 'just outside' implies that the electron has escaped the potential well of the solid, but is not infinitely far from the surface. The energy of an electron at rest an infinite distance away from a surface is considered an invariant energy reference.[28,31] A distinction has evolved between the vacuum level 'just outside' a surface, which is material dependant, and the vacuum level at infinity, which is not. The fact that there is this distinction between the vacuum level definitions is because the surface vacuum level is experimentally measurable, while it is believed that the infinity vacuum level is not measurable.[28] The reason why the surface vacuum level and the infinity vacuum level are different is the result of the formation of surface dipoles at the termination of the bulk.[30]

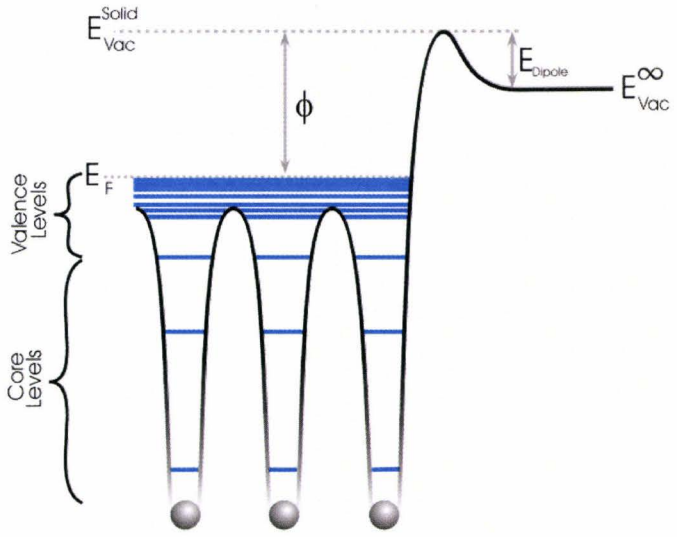

Figure 2.3 *– Schematic diagram of the energetics of a surface dipole, where Φ is the work function, E_F is the Fermi energy, E_{vac}^{∞} is the energy of an electron at rest in infinite vacuum, E_{vac}^{solid} is the 'local' vacuum level of the solid, and E_{dipole} is the potential of the surface dipole.*

Surface atoms are different from bulk atoms because they are not surrounded by as many neighbors as atoms in the bulk. As a result of the termination of the bulk, electron orbitals decay exponentially into the vacuum.[30] Since these atoms have no neighbors on the vacuum side, there are no positive cores to compensate for the electron density outside of the surface. Therefore a dipole is formed at the surface, with a negative pole on the vacuum side and a positive pole on the bulk side.[30] This surface dipole creates an energy barrier for electrons leaving a solid, as depicted in figure 2.3.

The strength of the dipole and height of its barrier will differ for different crystal faces, since the packing of the faces are different.[28] Furthermore the strengths of dipoles depend on the bonding in the solid. A covalent solid will have large dipoles compared to metals and may even reconstruct their surfaces to become more stable.[27] Covalent solids with polar bonds such as oxides would have very large surface dipoles,[54] although this scenario has not been explored very extensively from a work function point of view.

Following the explanation of a surface dipole it is appropriate to define work function in a different manner. Work function is the energy required for an electron from the Fermi level to overcome the surface dipole barrier with zero kinetic energy.

2.3.3 - Solid-state hetero-junctions

We will now consider what happens to a surface's energy profile when two surfaces are joined together to make a junction. We will start by reviewing some well-studied systems and finish by carrying over some of the conclusions of these studies to the organic semiconductor/inorganic semiconductor hetero-junction.

The first hetero-junction to consider is the metal-metal junction of two dissimilar metals. One can imagine two metals *A* and *B* separated by infinite distance as illustrated in figure 2.4(a). Here the metals both have their own unique work functions and Fermi levels, and they share a common infinity vacuum level.[27] When the two metals come into contact they adjust their electron populations to reach thermodynamic equilibrium (figure 2.4b and c). Thermodynamic equilibrium is reached when the chemical potential per electron is uniform throughout the solid, which is equivalent to saying that their Fermi levels are aligned.[55] This is achieved by electrons moving from the metal with the smaller work function (*A*) to the metal with the larger work function (*B*).[27,55] Now metal *A* becomes positively charged and metal *B* becomes negatively charged.

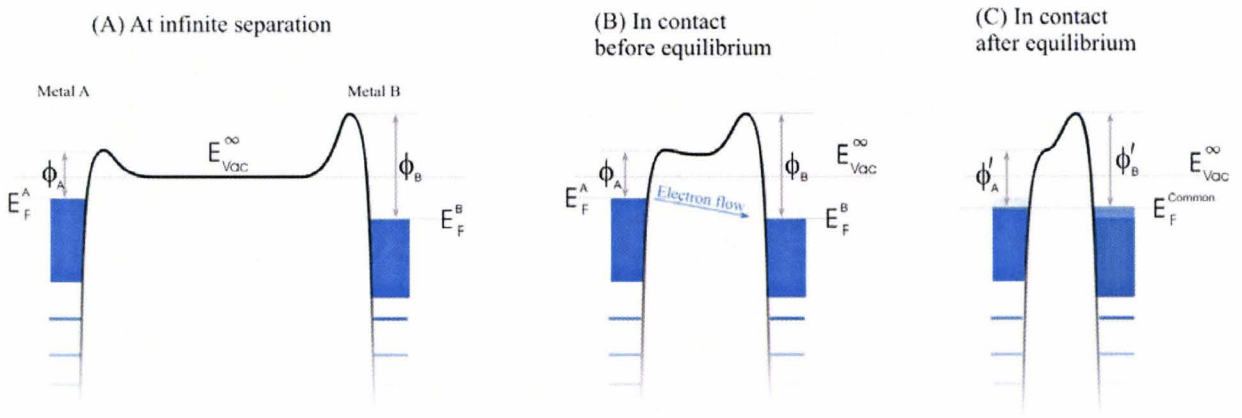

Figure 2.4 *– In (a) the metals are at infinite separation. They are not influenced by each other. Their Fermi levels are different and their work functions are different. In (b) the metals have come into contact but have not reached equilibrium. Electrons flow from the valence band of the metal with the smaller work function to the conduction band of the metal with the larger work function. In (c) the metals have reached equilibrium. Their Fermi levels have become aligned and their effective work functions are now different from what they were as isolated metals.*

The metal/metal hetero-junction scenario shows that when two conductive solids come into contact they make their electron chemical potentials equal to each other. When

a metal and a semiconductor come into contact their Fermi levels also align by transfer of charge from one solid to another.[27] The charge transferred across the interface results in an interface dipole, whose electric field is screened by the rearrangement of charge.[27] In the metal, due to the high carrier densities the electric field is screened within a fraction of an Ångstrom.[56] Since semi-conductors have orders of magnitude lower carrier densities than metals, the electric field from the dipole is screened out over some tens of nanometers into the bulk.[56] This screening over a relatively large distance is called the space-charge region, and results in a field gradient through the region, which consequently shifts the electron energy levels within this region. The shifting of energy levels in the space-charge region is called band bending.

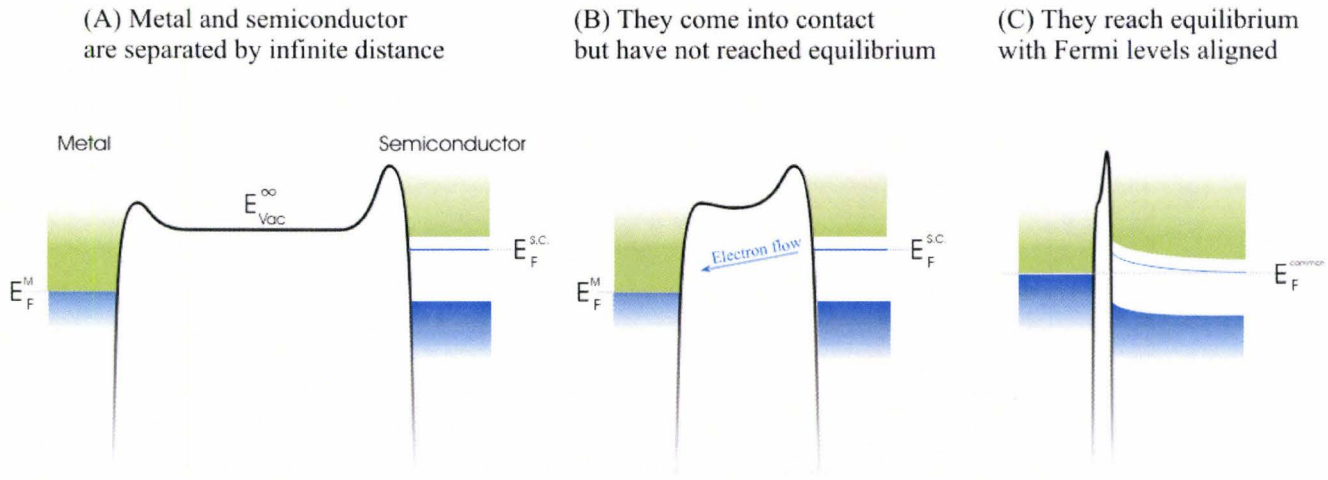

Figure 2.5 – Schematic energy level diagram of the formation of a metal/n-type semi-conductor junction. The unoccupied bands are in green and the occupied bands are in blue. The horizontal blue line in the semiconductor represents donor states.

As an example of a metal/semiconductor hetero-junction we will consider the metal/n-type semiconductor junction as shown in figure 2.5. When the two solids come into contact, electrons flow from the donor levels of the semi-conductor into the conduction band of the metal.[27] This charge flow allows Fermi levels to align, however it

leave ionized donor states behind in the semiconductor near the interface, causing an upward band bending near the interface.

When a p-type and an n-type semiconductor come into contact the situation is similar except that there is a space-charge region on both sides of the junction.[27,28] This scenario is shown in figure 2.6. Here we see that the Fermi levels have aligned via charge transfer from the n-type to the p-type semiconductor. As a result of the low carrier densities the field produced by the charge transfer across the junction is screened out over some distance through the semiconductors, resulting in band bending.

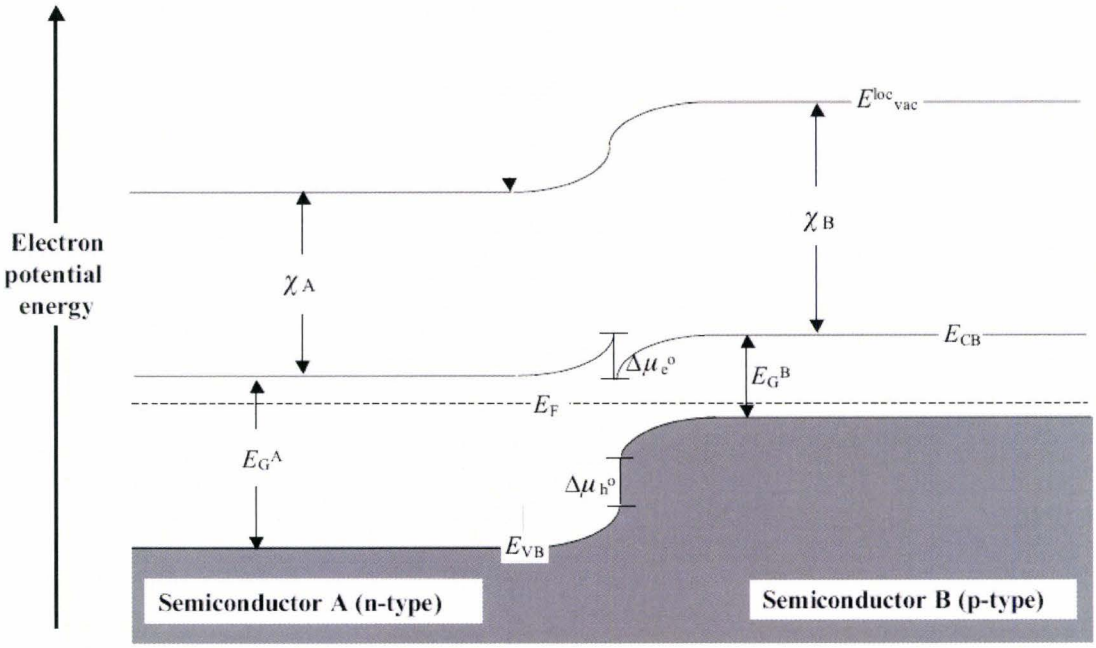

Figure 2.6 *– Energy level diagram for a p-n junction [Ref. 28].*

The three types of hetero-junction mentioned above have been studied thoroughly in the field of solid-state device physics. More recently these concepts have migrated over to the study of conducting organic junction devices.[31] The energetics of metal/molecular-organic and inorganic-semiconductor/organic-semi-conductor interfaces

for the development of organic light emitting diodes (OLED's) and solar energy conversion.[31] By using the previously developed theories from solid state hetero-junctions they have found some similarities as well as some unique phenomena.

When an organic semiconductor forms a junction with a metal then just as in the inorganic semiconductor case there is the possibility of charge transfer across the interface.[29,31] If this is the case, and charge carrier densities are large enough in the organic solid then there will be band bending in the organic layer, however there is also the possibility of localized charge transfer between the metal and organic, leading to localized covalent bonding at the interface and trapped charges.[31] If carrier concentrations are not large enough in the organic material for band bending then the surface potential of the metal can be screened by the organic material by polarization of the organic molecules near the interface.

Interfaces between inorganic semiconductors and organic semiconductors have not been thoroughly studied as of yet, however one can imagine that there is the possibility of band bending in the inorganic semiconductor (ISC) and the organic semiconductor (OSC), as well as the possibility of localized interfacial bonding.

The behavior of electron energy levels at interfaces can be generalized as follows. When a junction is formed each material is perturbed by the change in electrochemical potential caused by the presence of the other. In order to neutralize the effect of the other solid each one either transfers charge or rearranges charge in order to screen the potential of the other. These effects lead to a change in electron energies near an interface.

2.3.2 - Work function changes due to adsorption of molecules

It is a general phenomenon that the work function of a solid changes as a result of adsorption of a molecule. The electric field due to a surface dipole can extend several nanometers away from the surface, so when a molecule adsorbs it experiences the field of the surface dipole. Molecules with permanent dipoles align with the surface dipole, while those without a permanent dipole will become polarized in the presence of the surface dipole field. As a result of molecular dipole alignment, molecules can stabilize the substrate's surface dipole to cause a reduction of the surface energy barrier, as depicted in figure 3.4. The net result is that there is usually a change in the work function of the substrate. If the substrate is a semiconductor there is also the possibility of band bending near the surface. These phenomena can be measured experimentally using photoelectron spectroscopy as described in section 3.1.

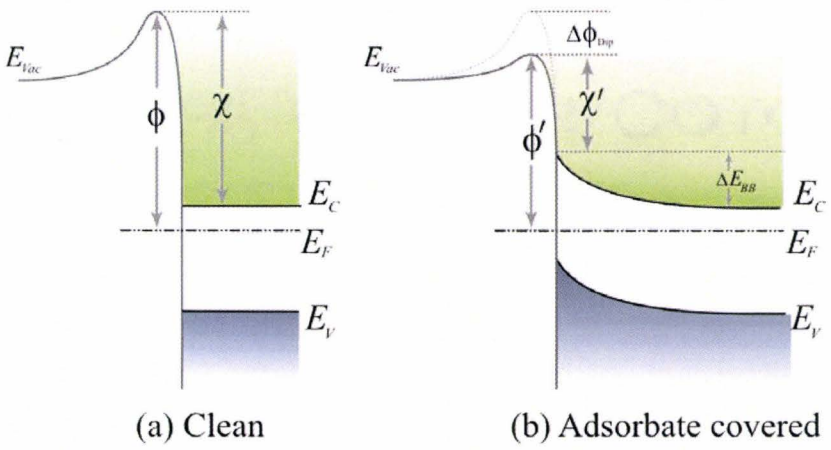

Figure 2.7 *– Schematic representation of how a substrate's surface electronic structure changes upon adsorption.* E_{Vac} *is the vacuum level at infinity,* E_c *is the conduction band minimum,* E_v *is the valence band maximum,* E_F *is the Fermi level,* χ *is the electron affinity, and* Φ *is the work function.*

Chapter 3 – Description of experimental techniques

3.1 – Photoelectron spectroscopy

3.1.1 –The physical process of photoemission

Photoemission (a.k.a. the photoelectric effect) occurs when a photon transfers energy to an electron trapped in the potential well of an atom, molecule or solid, such that the electron obtains enough energy to escape from the potential well. The electron is propelled into the vacuum with some kinetic energy. The kinetic energy of the photo-ejected electron is given by the following equation.[57]

eq. 3.1 $$E_{kin} = \hbar\omega - \phi - E_B + E_{dipole}$$

Here, E_{kin} is the kinetic energy of the photo-ejected electron, $\hbar\omega$ represents the energy of a photon with frequency $\omega/2\pi$, E_B is the binding energy of the photo-ejected electron in question (with the Fermi energy taken to be zero), ϕ is the work function and E_{dipole} is the energy of the surface dipole barrier with respect to the infinite vacuum level. The terms E_B and E_{dipole} are only used when the sample is a solid.

Photoelectron spectroscopy (PES) is a technique which analyzes the kinetic energy of photo-ejected electrons. By knowing the energy of the light used to eject the electrons as well as the work function of the sample, one can obtain a spectrum where the peaks approximately represent single-electron orbital energies (although this approximation is not always valid).[57] A schematic of the photo-ionization process and how peaks in a spectrum derive from electronic states is shown in figure 3.1.

Electrons can be ejected from valence states (i.e. those involved in chemical bonding) or from core states. The valence electrons will have the smallest binding energies (between 0 to 10eV below the Fermi level) and the core electrons will have

larger binding energies (ranging from ~20 to about 115 000eV). If one wishes to probe only the valence states then ultraviolet (UV) radiation is used and the analysis method is called ultraviolet photoelectron spectroscopy (UPS). If one wishes to probe deeper states then X-ray radiation is used and the analysis is called X-ray photoelectron spectroscopy (XPS).

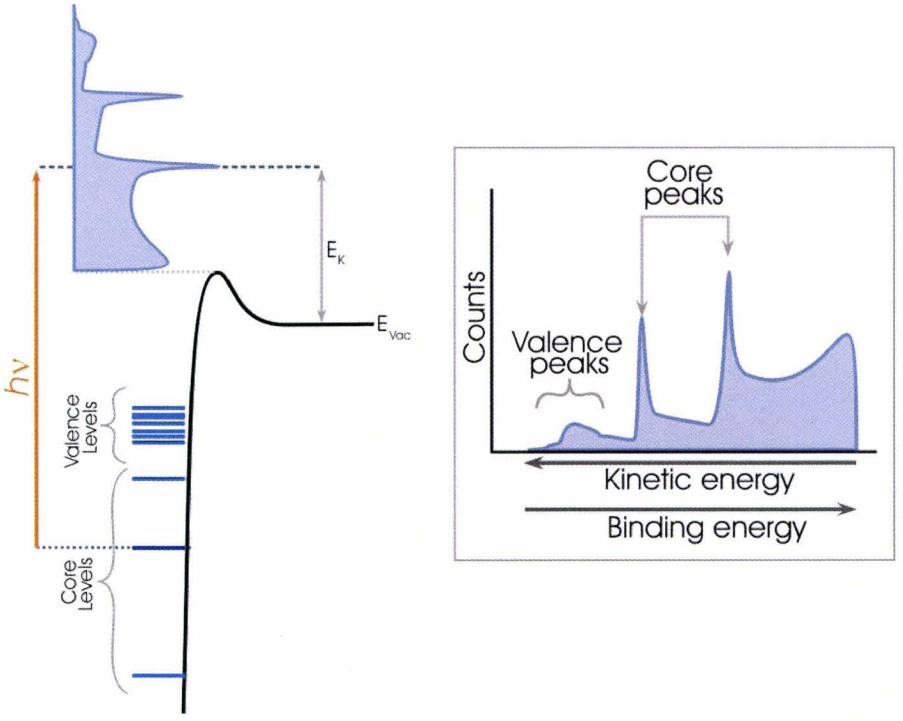

Figure 3.1 *– Schematic illustration of energy levels and the surface energy barrier of a solid, and how the photo-emission process leads to a spectrum*

Since valence electrons are the ones participating in bonding one would expect that they would be the most sensitive to bonding environment, and would therefore be most useful for extracting chemical information. While it is true that valence states are the most sensitive to chemical environment, UPS is not always useful for gathering

information about bonding. This is because UPS spectra are often composed of many highly convoluted peaks, due to the high energy density of valence states, which can make UPS spectra very difficult to interpret. In the gas phase UPS can show several sharp and distinct peaks, representative of the HOMO and near-HOMO energy levels. In the solid state UPS can be representative of the density of states (DOS) below the Fermi energy, which makes it a valuable technique for solid-state physics.

Core electrons do not participate in chemical bonding but their energies are still affected by their chemical surroundings, and while valence states are often very close in energy to one another, core peaks are often very well separated, and highly characteristic of a particular element. As a result of the good peak separation, XPS spectra are less convoluted than UPS spectra, and it much easier to identify peaks and attribute them to electronic states in an XPS spectrum than it is in a UPS spectrum. Since XPS spectra give chemical information and are easier to read, XPS is more widely used than UPS. Without assigning each peak in a UPS spectrum, one can still extract some valuable information, such as the difference between the Fermi level and the highest energy valence state of a solid, or the energy of the HOMO in a molecule. The spectra can also give a rough idea of the density of occupied states near the Fermi level.

3.1.2 – Electron escape depths

Photons can penetrate several microns into a solid before being scattered. Electrons, on the other hand will be scattered every few Ångstroms to a few nanometers that they travel through a solid.[58] A scattering event can be elastic or inelastic; however inelastic scattering is more likely.[55] As an electron suffers more inelastic scattering events

it eventually looses so much of its kinetic energy that it can no longer escape the work function of the solid, and will therefore not reach the photoelectron detector. So even though electrons are photo-ejected several microns deep within a sample, only those ejected from the first few nanometers will reach the electron detector.

Electron scattering in this scenario is believed to be caused by valence charges in a solid redistributing in response to an electron in transit.[59] Energy can be transferred from the electron in transit as a result of this charge redistribution. The two main mechanisms of energy transfer are via plasmon excitation and via single electron excitation.[55,59] A plasmon is a quantized oscillation in charge density within the valence band of a solid.[60] When an electron is inelastically scattered by a plasmon some of the electron's kinetic energy is used to put the plasmon in an excited state.[55] Single electron excitations scattering is when an electron traveling through a solid transfers some of its energy to a single electron, putting that electron in an excited state.[55] Both plasmon and single particle scattering processes are material dependant and they are also electron energy dependant.

The average distance an electron can travel through a solid before being inelastically scattered is described by the mean free path of the electron, λ.[61] The mean free path of an electron through a solid depends on the energy of the electron as well as the scattering properties of the solid.[55]

Theoretical calculations of mean-free-path for an electron traveling within a solid show that for energies below the plasmon energy of the solid, inelastic scattering is dictated by single-electron excitations.[55] At energies above the plasmon energy, plasmon scattering dominates.[55] Figure 3.2 (a) shows a plot of mean free path versus electron

energy for the two different scattering processes. A collection of experimentally determined electron attenuation lengths are shown in figure 3.2 (b). The spread of values may be due to the material dependence of attenuation length or due to measurement uncertainties however in general the theoretically predicted trend is followed.

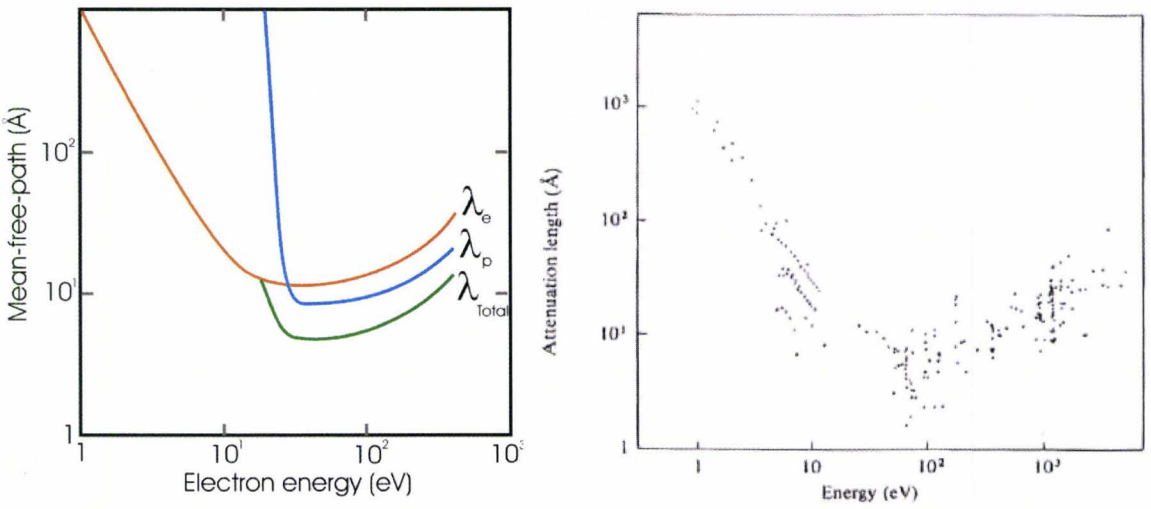

Figure 3.2 *– (a) Calculated inelastic mean free paths of electrons in a solid, based on the single electron quasi-free model of a solid. (b) A collection of measured attenuation lengths of several solids [Ref. 55].*

Mean free path has a slightly different definition from attenuation length, and experimentally attenuation length is of more use, however they both follow the same trend.[61] They both show that between the energies of 10 and 100 eV, electron penetration through a solid reaches a minimum between 1 and 10Å. At energies as high as thousands of electronvolts attenuation lengths are between 10 and 100Å, and at very low energies of around 1eV attenuation lengths can be as large as ~1000Å. Most electrons of interest in XPS and UPS measurements have kinetic energies between 10 and 1000eV and therefore

only move on average a few tens of Ångstroms or less before being inelastically scattered.

While electrons may suffer an inelastic collision within a few Ångstroms of travel, they are not necessarily going to lose so much kinetic energy that they can no longer escape the solid after only one or two inelastic collisions. However, once an electron suffers an inelastic collision it no longer carries a kinetic energy that is representative of its photoemission mechanism.[57] Since collisional energy transfers are not quantized (or at least not measurably so) inelastically scattered electrons leave the solid with a continuous distribution of energies, while electrons which have not suffered a collision exit the solid with a kinetic energy representative of the quantized electronic state from which the electron was ejected.[57] This means that the electrons which carry the chemical information and give rise to the distinct peaks in a spectrum can only come from within the attenuation

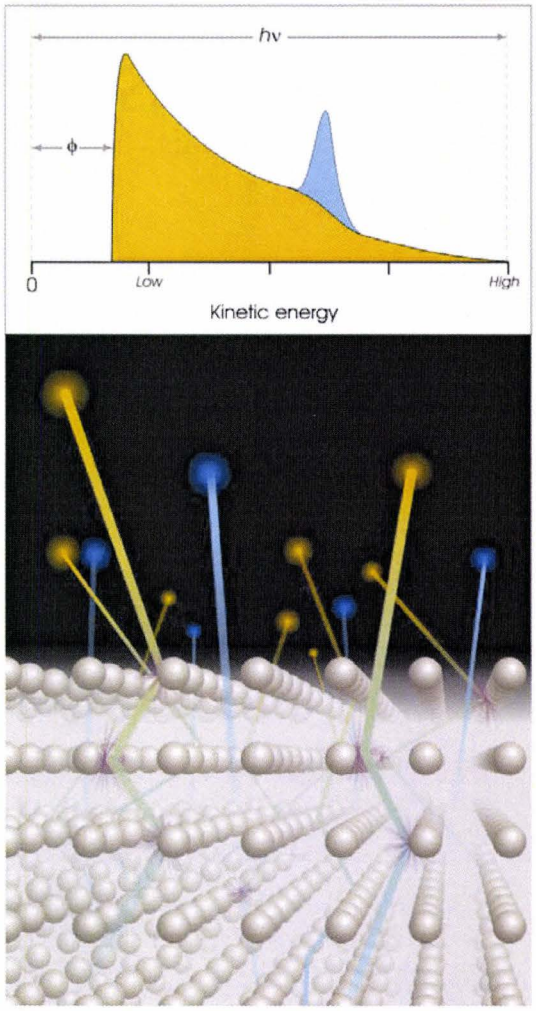

Figure 3.3 *– (top) illustration of a hypothetical photoemission spectrum, where the inelastic part is in orange and the elastic part is in blue. (bottom) Artist's rendition of electron scattering within a solid.*

length deep within a sample. The general qualitative properties of a spectrum are several distinct peaks overlaid on a broad continuous background, which increases intensity towards lower kinetic energies and then cuts off a few eV above zero kinetic energy (as depicted in figure 3.3).

3.1.3 – Qualitative and quantitative properties of photoelectron spectra

As mentioned above, photoelectron spectra consist of several distinct peaks overlaid on a broad background of increasing intensity towards low kinetic energies. The inelastic background increases in intensity in steps after each photoionization threshold is reached. The increase in inelastic electrons after each photoionization threshold is due to the fact that there are more electrons being produced once the threshold has been reached, and therefore more electrons being inelastically scattered.

The inelastically scattered electrons in the lowest-energy regime (between 0 and ~50eV) are considered the 'secondary electrons' and the large increase in intensity in this regime is due to the rapid increase in inelastic mean free path at low energies.[57] The energy at which their intensity cuts off is representative of the sample's work function, as shown in figure 3.3. One can obtain a quantitative value for the work function by taking the range of kinetic energies for which photoelectrons are observed and subtracting this value from the photon energy. The resulting value is the work function.

As mentioned in section 3.1.1, the kinetic energy of a photo-ejected electron is related to the binding energy of that electron by equation 3.1. One can therefore convert the x-axis from kinetic energy to binding energy by subtracting the kinetic energy and work function from the photon energy. The binding energy of an electron approximately

represents the orbital energy of the electron in its initial state. In a photoemission experiment one measures the difference in energy between the initial state (an *N*-electron system) and the final state (an (*N*-1)-electron system).[57] In a system of non-interacting electrons, the energies for these two states are simply the sums of the energies of one-electron wavefunctions.[55]

initial state: $$E_N = \varepsilon_1 + \varepsilon_2 + \varepsilon_3 + ... + \varepsilon_{v-1} + \varepsilon_v + \varepsilon_{v+1} + ... + \varepsilon_N \qquad \text{eq. 3.2}$$

finial state: $$E_{N-1} = \varepsilon_1 + \varepsilon_2 + \varepsilon_3 + ... + \varepsilon_{v-1} + \varepsilon_{v+1} + ... + \varepsilon_N \qquad \text{eq. 3.3}$$

Here an electron has been removed from the state denoted by subscript v and therefore the final-state energy equation lacks the term ε_v. The difference in energy between the initial state and the final state is called the binding energy and in the one-electron picture it is equivalent to the energy of the state from which the electron was ejected, as shown in the following equation.[55]

$$E_B = E_{N-1} - E_N = -\varepsilon_v \qquad \text{eq. 3.4}$$

Equation 3.4 is referred to Koopmans' theorem. It is exactly true for the one-electron approximation of equations 3.2 and 3.3, however it is also true when electron correlations are taken into account because the electron interaction energies of the *N* electrons are cancelled out when the electron interactions from the *N*-1 electrons are subtracted. The orbital energy then does not represent a single-electron orbital, but rather it represents the energy of a true interacting electron orbital.

When a hole is formed by the removal of one electron, the remaining *N*-1 electrons re-adjust themselves in response to the presence of the hole.[57] The final state 'relaxes' by electrons re-adjusting 'screen' the hole.[57] Due to the complex interactions of electrons these relaxation processes are not easy to calculate, however whatever errors

involved in the calculations of electron interactions for the final state are also involved in the initial state calculation, so most of the errors cancel each other out in Koopmans' theorem and it remains accurate except for very highly correlated systems such as transition metal oxides.[34]

Aside from electron re-organization in response to the photohole final states can also involve excitation of a plasmon or phonon.[57] The part of the relaxation energy required to excite the plasmon or phonon is then no longer given to the photo-ejected electron, and it reaches the detector with less kinetic energy, giving rise to additional peaks not predicted by Koopmans' theorem, called 'satellites'. Satelites appear in a photo-electron spectrum as broad peaks with lower intensity and on the lower kinetic energy side of than the main photoelectron peak.[57] Satellites often complicate a spectrum however not all elements exhibit them, and they are more common when there is strong electron correlation.

Although many-body effects can give rise to their own spectroscopic features (as in satellites) and complicate the interpretation of peaks in terms of single-electron model, binding energies are still indicative of an element's bonding environment and are therefore still carry valuable chemical information. When an atom participates in a chemical bond the electron configuration of the neighboring atom influences the local electrostatic potential of the core levels and thereby changes their binding energies.[57] If an atom is involved in a bond where its valence electrons are pulled away from it (i.e. if the atom is oxidized) then there is less electron-electron repulsion compared to the zero oxidation state and as a result the binding energies are greater.[57] In the reverse scenario, if the atom is involved in a bond where it is pulling more electrons towards itself (i.e. the

atom is reduced) then the increased electron-electron repulsions decrease the binding energies. Therefore XPS can distinguish between different oxidation states of the same element. Furthermore it can distinguish between bonds to different elements, for example the O1s binding energy for O in an Fe-O bond will be different from the O1s in an H-O bond.[62]

3.2 Photoemission electron microscopy

A photoemission electron microscope (PEEM) works by illuminating a sample with relatively high-energy light to photo-eject electrons, then using electric or magnetic field lenses the photo-electrons are focused into an channel-plate electron multiplier and then onto a phosphore screen.[63,64] The electrons can be focused into a real-space image which represents the spatial distribution of photo-emission intensity. A schematic illustration of a PEEM is shown in figure 3.4.

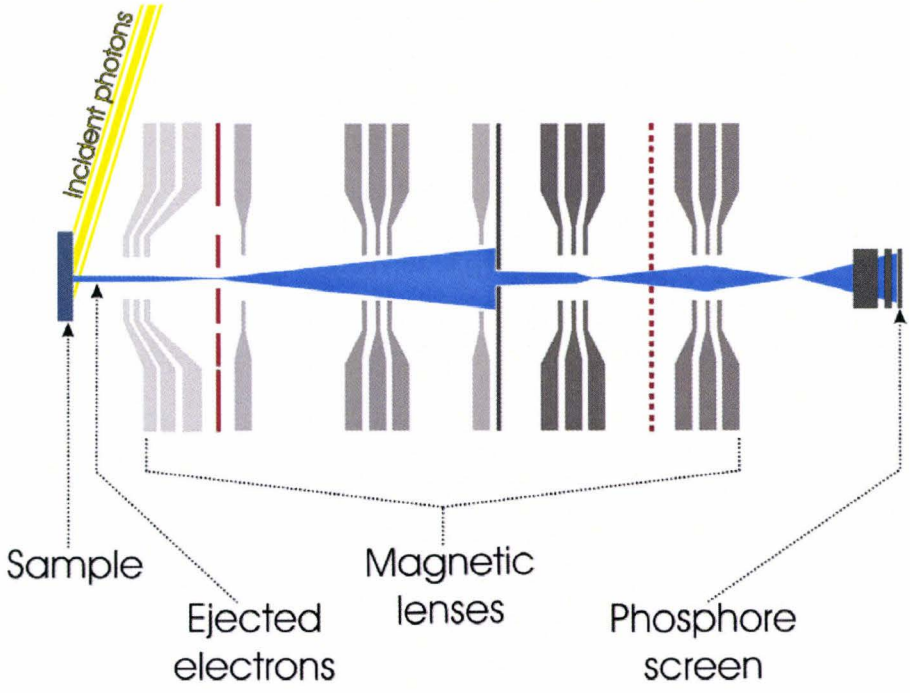

Figure 3.4 *– Schematic diagram of a photoemission electron microscope.[Ref. 65]*

As described in the photoelectron spectroscopy section, when electrons are photo-ejected from a surface they come off with a distribution of kinetic energies as shown in figure 3.5 below.

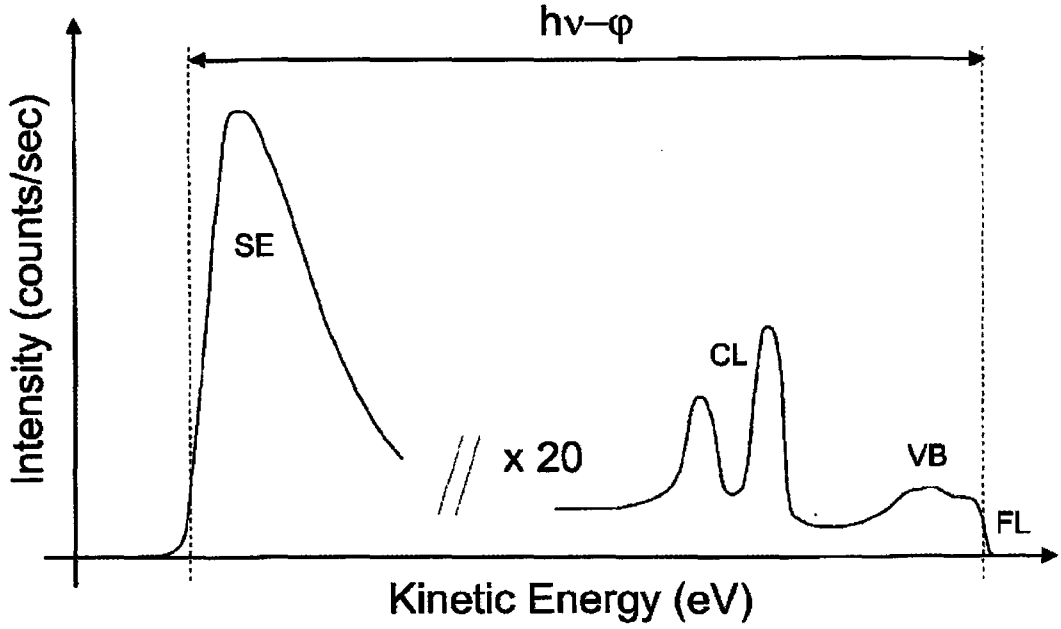

Figure 3.5 *– Illustration of stereotypical photo-electron kinetic energy distribution for electrons coming off a surface being photo-excited by X-ray photons. SE represents 'secondary electrons', CL represents 'core levels', VB represents 'valence band', FL is 'Fermi level', hν is the energy of the photons and φ is the work function of the sample. [Ref. 63]*

The microscope can be set to collect all the photo-electrons being emitted in 'total-yield' mode, or if an energy filter is incorporated into the instrument the PEEM can be set to collect only the photoelectrons coming off with a specific kinetic energy in 'energy filtered' mode.[63]

Figure 3.6 illustrates how contrast occurs in PEEM images.[63] The top circles represent PEEM images of a material 1 embedded in the center of material 2. The

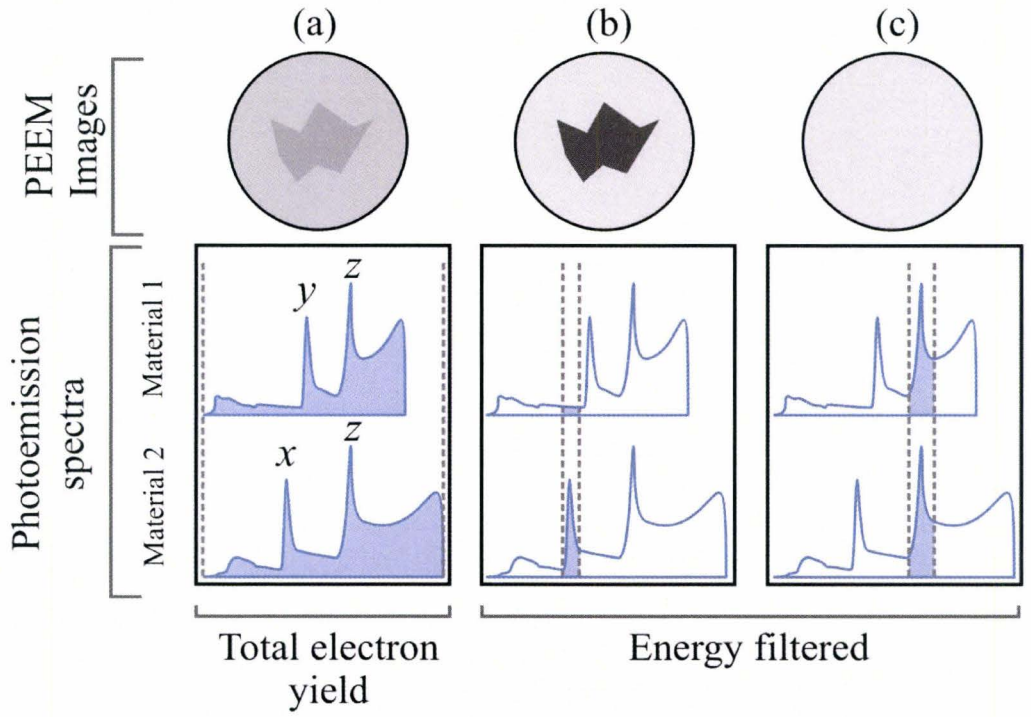

Figure 3.6 *– Illustration of how contrast is obtained in PEEM imaging using (a) 'total yield' mode and (b) and (c) 'energy filtered' mode.*

photoemission spectra of the two materials are different. Material 1 has a larger work function than material 2. Resonant photoemission peak denoted by *x* is unique to material 2, peak *y* is unique to material 1, and *z* is common to both materials. In (a), the microscope is operating in 'total yield' mode, so all kinetic energies are being collected. For this case the PEEM image shows a slight contrast between the two materials due to their different work functions. Figure 3.6 (b) and (c) represent 'energy filtered' mode. In (b) the kinetic energy window encompasses the resonant photoemission peak *x*. Since *x* is unique to material 1, it appears much brighter in the PEEM image. In (c) the energy window encompasses resonant feature *z*, but since it is common to both materials the PEEM images shows no contrast.

The above example illustrates how PEEM images might look if one were to use a photon source of high enough energy to photo-ionize core levels; however it is common for routine imaging purposes to use a low-energy photon source such as a mercury lamp, which has maximum photon energy of about 4.9eV. This scenario is illustrated in figure 3.7. Since the photon energy of this source is so low it is only capable of ejecting valence electrons, the spectrum is completely dominated by the secondary electron intensity, and all valence features become washed out.[63] In this case the image contrast will be due to overall photoemission cross sections or work function differences.

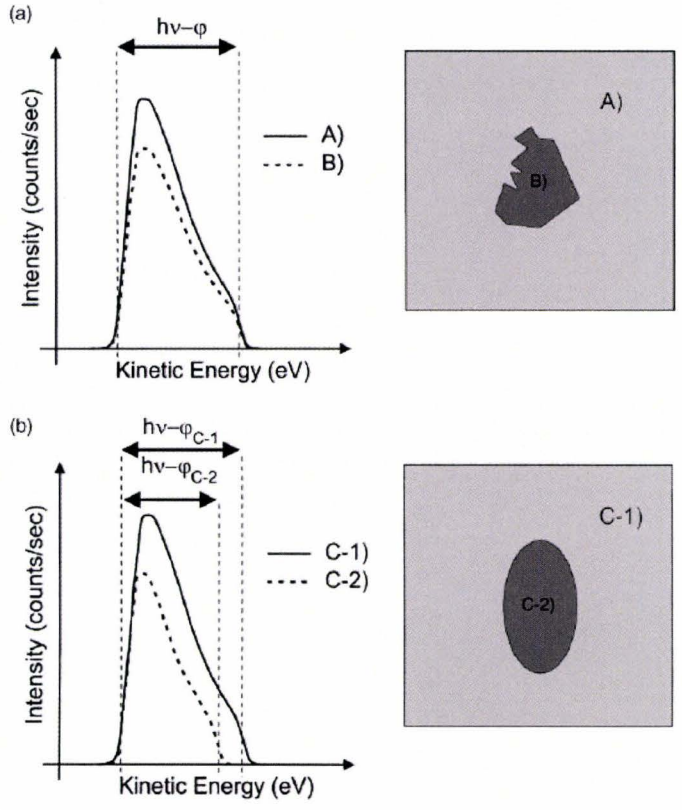

Figure 3.7 *– Illustration of how PEEM image contrast is affected by (a) photoemission cross section and (b) work function of two materials when the sample is excited by a Hg-lamp (hν ~4.9eV). [Ref. 63]*

Regions with large work functions will appear darker than regions with small work functions (provided the chemical composition or the photoelectron yield is otherwise the same for the two regions). This type of scenario is seen in the case of polycrystalline metals, where various crystallographic orientations are exhibited on the surface of the metal, as shown in figure 3.8. The largest grain contrast is obtained when imaging in 'total yield' mode, using an Hg-lamp for excitation.

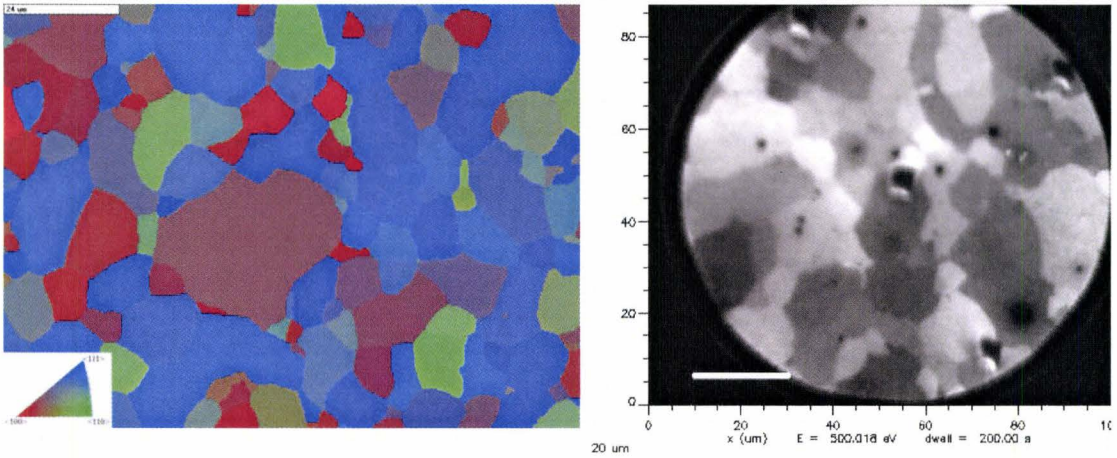

***Figure 3.8** – Electron backscatter diffraction map (left) and PEEM image (right) of polycrystalline iron substrates.*

While 'total yield' mode is useful for obtaining microscopic images with high contrast, incorporating an energy filter can allow one to obtain spatially-mapped photoelectron spectra to go with the images. This is done by filtering out all of the photo-electrons except for those within a narrow window of kinetic energies.[63] Then only the photo-electrons with the chosen kinetic energy will reach the detector. The resulting image will be a map of where the electrons of that particular kinetic energy came from. By sweeping this kinetic energy window across the whole spectrum and collecting an

image at each step, one obtains a stack of images. In a stack of images, each pixel has a corresponding intensity-vs.-kinetic energy spectrum.

In our experiments we used an Elmitec PEEM III with a hemispherical energy analyzer (which is a band-pass filter) incorporated. In this instrument the sample is held at -20kV relative to the objective lens, so that the photo-ejected electrons are accelerated through the lens system with 20,000eV of kinetic energy. The lenses focus the electrons into an image, while contrast apertures remove electrons that are not useful for image reconstruction. Removal of these electrons reduces the signal intensity. The electrons then pass through the energy filter. The energy filter involves bending the electron paths, so that electrons with different energies travel different path lengths, resulting in a spatial dispersion of electron energies, as illustrated in figure 3.9.[63] The electrons then pass through a small aperture (a.k.a. energy slit), which cuts out all but a small window of kinetic energies. The remaining electrons are then re-focused onto the channel multiplier as a real-space projection.

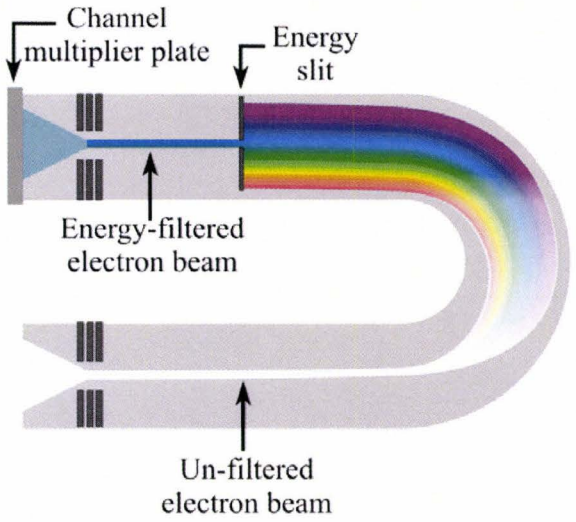

Figure 3.9 *– Schematic of hemispherical energy analyzer in PEEM III*

The energy resolution limit for this filter is 0.5eV. The higher the energy resolution the fewer electrons allowed through the filter to the detector. This means that at each kinetic energy increment in the XPS or UPS spectrum an image needs to be constructed from a very small signal, which leads to very long collection times.

In spite of the inconvenience of very long collection times, the prospect of having spatially resolved XPS/UPS makes this technique very valuable. In a conventional photoelectron spectrometer the collected signal is a mixture of photoelectrons from a large area of the sample (usually around 400μm^2). If the sample is not homogeneous across the surface of the sample then different spectra are convoluted together and the interpretation of the results is uncertain. When the spectra can be spatially assigned the information becomes a lot more valuable. In our experiments we hoped to see spectroscopic evidence of a 'remote effect' (i.e. we hoped to see a spectroscopic signature of PCAT-Fe interaction some distance away from the edge of a PCAT film). In this case the spatial resolution was essential.

For the PEEM we were using, the field of view (FOV) could be varied from as large as 100μm to as small as 1μm, however at a small FOV the collection times necessary for a good signal-to-noise stack can become very long and sometimes even impractical. Although the ultimate resolution of a PEEM is limited by the spherical aberrations, chromatic aberrations and the diffraction error,[63] we found that in order to collect a stack the collection time became the limiting feature long before any of these physical limitations became a factor. In principle the spatial resolution of a PEEM (using magnetic lenses, synchrotron radiation and provided the sample is flat enough) can reach 50-100nm. While we were able to obtain single images with a resolution around 150nm if

we used all the photoelectrons available, when we incorporated the energy slit to acquire stacks our best resolution was around 500nm using the 50μm FOV.

3.3 – Interface characterization by in-situ step-by-step depositions

The interface energetic, as discussed in section 2.3.3, are not easily studied because interfaces in such devices are always buried under bulk material. In order to study interfaces with electron spectroscopy, where electron attenuation lengths are on the order of Ångstroms, the interface can only be probed through a thin film of one of the materials composing the hetero-junction. Therefore, the technique devised to study these interfaces with electron spectroscopy involves coating one material with the other in very small increments (a few Ångstroms at a time if possible) and measuring photoelectron spectra after each deposition. As the film thickens the overlayer spectra eventually become representative of the overlayer bulk. In doing this type of experiment, one therefore sees how the overlayer spectra are different near the interface as compared to the bulk spectra. In addition to the overlayer spectra, for the first few depositions the substrate photoemission signals are still observable, so changes in the substrate spectra caused by adsorption of the overlayer molecules can also be observed.

This type of analysis has been used many times in characterizing organic-metal interfaces. It can yield many pieces of information about the nature of the overlayer-substrate interaction. For example it can reveal band bending in the substrate or overlayer, covalent bond formation at the interface, work function changes to the substrate, interface dipole formation, Fermi level alignment, and HOMO-valence bend off-sets. How these properties can be derived from the spectra will be discussed below.

A Schematic of how photoemission spectra change during an in-situ step-by-step deposition is shown in figure 3.10.

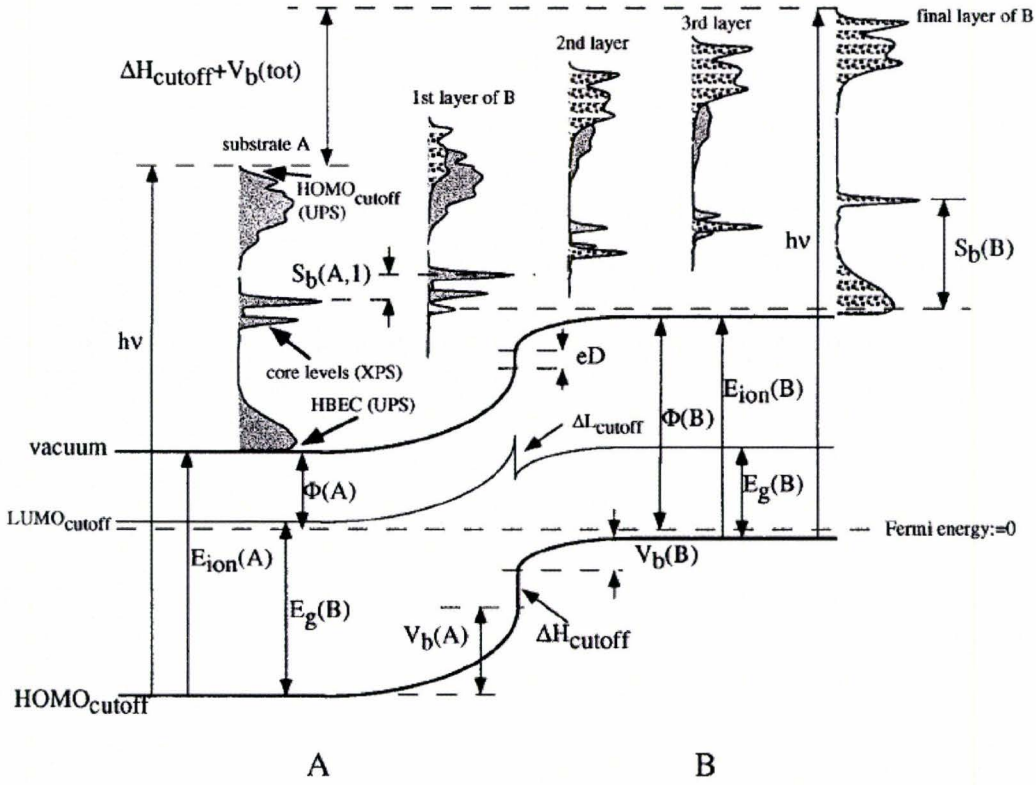

Figure 3.10 *– Schematic of orbital line-up and corresponding photoemission spectra for an in-situ step-by-step deposition. [Ref. 86]*

In this figure, the substrate (A) energy levels and photoemission spectra are shown on the left, and the overlayer (B) on the right. In this scenario there is band bending in both the substrate and the overlayer, as well as a dipole layer at the interface. The band bending in the substrate is found by following the substrate core levels throughout the deposition. In figure 3.10, after the first deposition we see that the core levels in the spectra have shifted upwards by an amount $S_b(A,1)$. This shift indicates an electric field or space-charge region in the substrate as a result of the interface with the

overlayer. This band bending also causes a corresponding shift in the valence features and in the substrate work function as well.

As the overlayer thickness increases the substrate signal becomes buried, while the overlayer signal grows in. By monitoring the shift in core levels of the overlayer during the deposition one can determine if there is band bending (i.e. space-charge region) in the overlayer. From figure 3.10 we see there is a band bending in the overlayer by the amount $S_b(B)$. One can then determine the interface dipole by taking the total change in work function, which is determined by the difference in the position of the secondary cutoff for the clean substrate spectrum and the thick overlayer spectrum, and subtracting from it the total band bending. The resulting value is the energy shift caused by the interface dipole (eD in figure 3.10).

An example of photoemission spectra of a deposition series exhibiting band bending is shown in figures 3.11 and 3.12.

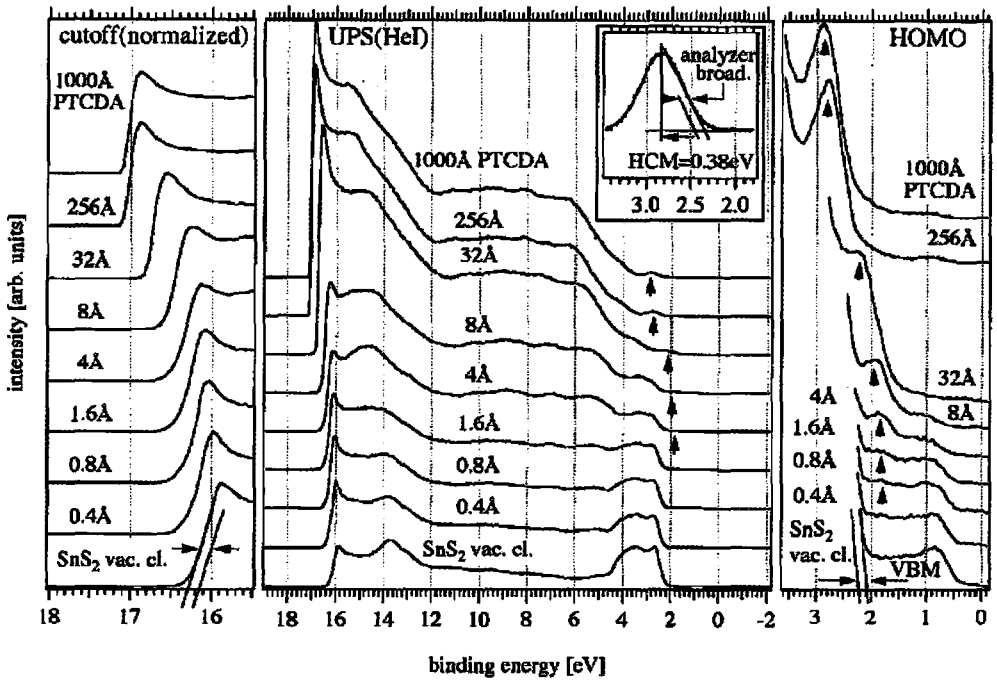

***Figure 3.11** – UPS spectra of an in-situ deposition of PTCDA on SnS_2. [Ref. 87]*

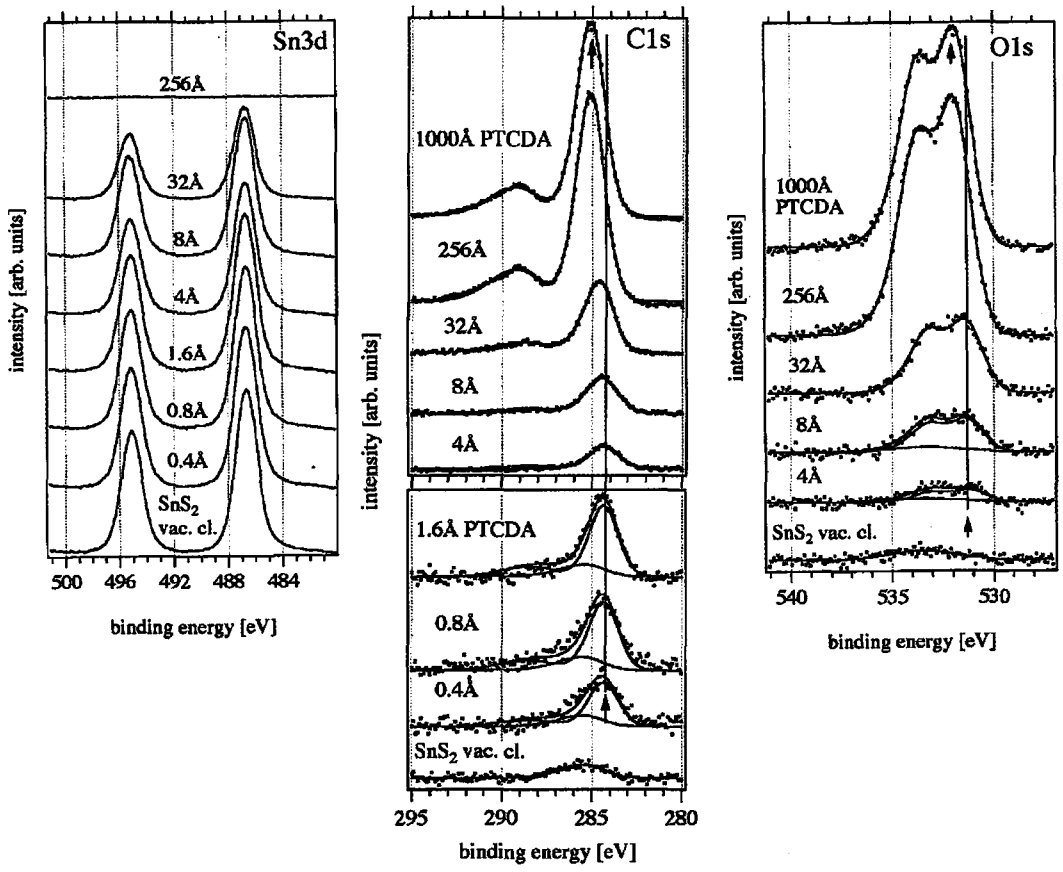

***Figure 3.12** – XPS spectra for step-by-step deposition of PTCDA on SnS_2. [Ref. 87]*

In figure 3.11 one can see that the valence spectrum of the substrate transitions to that of the overlayer. In the left panel one can see that during the transition the secondary cut-off shifts by about 0.9eV to higher binding energy, which is indicative of a change in work function. The valence region also shows the appearance of a new valence state at the interface, indicated by the arrows in the right panel of figure 3.11. The existence of interface state is known from inorganic semiconductor/metal interfaces, where they are called metal-induced gap states (MIGS).[27]

In figure 3.12 the XPS spectra for the same deposition series are shown. The left panel shows the spectra of the substrate. From the lack of any shifting in the substrate

signal one can conclude that there is no band bending in the substrate. The overlayer spectra however (central and right panels in figure 3.12) show a shift to higher binding energy during the deposition. This indicates a band-bending or space-charge region in the overlayer. Based on the direction of the shift, one can conclude that the band bending is caused by an electron depletion region as seen for p-type semiconductor-metal hetero-junctions.

While such an analysis can reveal band bending and energetic alignment at an interface, it can also show the existence of a localized covalent bond at reactive interfaces. Such an event would show up as an extra peak in the core spectra at the interface, and would become buried as the overlayer becomes thicker, as shown in figure 3.13.

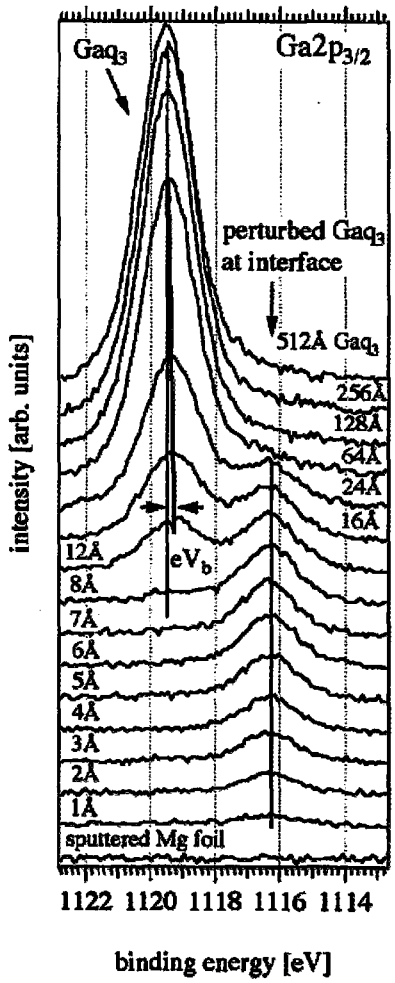

***Figure 3.13** – XPS spectra for a deposition series of Gaq_3 on Mg, showing the formation of a bond at the interface. [Ref. 88]*

The technique of photoemission characterization of a step-by-step deposition of PCAT on an oxide-covered iron substrate should lend some insight into similarities between the PCAT-oxide system and conventional semi-conducting organic/metal interfaces. Furthermore, it should show whether there is any unique behavior at the interface, and will determine whether there is a localized chemical interaction at the interface or whether the interface properties are governed by bulk characteristics.

Chapter 4 – Experimental

4.1.1 – Sample preparation requirements

Sample preparation and verification of sample preparation techniques was the most time consuming of all the efforts involved in these experiments, however it was also absolutely necessary in order for the results to have any value at all. In order for the XPS/UPS characterization step-by-step deposition of PCAT on Fe to be successful the films had to be deposited in sub-nanometer increments. This required very precise control over how much material we are depositing at one time and that the material be deposited uniformly across the surface. Furthermore, in order for our results to be unambiguously interpreted we had to be able to deposit PCAT on Fe in-situ in order to eliminate the possibility that atmospheric contamination was the cause for any observed phenomena. These requirements meant that we had to use some sort in in-vacuo deposition technique. The most simple of such techniques is physical vapor deposition, whereby a solid sample is simply heated in vacuum causing a small fraction of the solid to sublime. The vaporous substance then travels to the sample, held a few centimeters away from the evaporation source, where the vapor condenses onto the cold surface of the substrate.

4.1.2 - Design of the film deposition chamber

In order to avoid the incorporation of atmosphere-borne contamination into a film as well as oxidation of the evaporant upon heating, it is necessary to perform depositions under vacuum conditions. While ultrahigh vacuum is desired (10^{-9}-10^{-11} Torr) high vacuum is adequate (10^{-6}-10^{-9} Torr). In order to achieve this pressure during film deposition, the sample and evaporant must be housed within a heavy stainless steel

chamber, which is isolated from the atmosphere and continuously pumped on by several pumps. Generally a membrane pump or oil pump was used for the low vacuum range (10^{-3} Torr), turbo-molecular pumps were used to take the pressure to high vacuum range (10^{-7} Torr), and ion pumps and titanium sublimation pumps were used to bring the system to higher vacuum (10^{-9} Torr). Since it can take several days to weeks to obtain this pressure, the main chamber where the film deposition takes place was isolated from the sample entrance chamber (a.k.a. load lock) by a gate valve. This way the small load lock could be vented to atmosphere in order to load in a sample without venting the entire chamber. Due to its small size, the load lock can be evacuated relatively quickly.

Having one's sample inside a vacuum chamber severely restricts the ability to move and manipulate the sample. Careful planning and designing of the vacuum chamber was necessary in order to be able to transfer a sample into and out of a chamber as well as to have the capability of monitoring the thickness of film deposited, and heat and measure the temperature of the sample during deposition.

The sample would be mounted on a sample holder with a built-in heating filament and thermocouples. The sample could be moved from the load lock to the deposition stage using a magnetically-coupled transfer arm. The forks on the end of the arm fit into the groves on the side of the sample holder. The sample holder could then be placed into the sample stage, however alignment needed to be just right in order for the thermocouple and sample heater electrical contacts to be made.

In order to monitor the thickness of film being deposited on a sample a quartz oscillating thickness monitor was mounted close to where the sample is positioned during

deposition. The thickness monitor is capable of detecting the deposition of extremely thin films; it can detect a change in average film thickness of 0.1Å.

An evaporation source (a.k.a. Knudsen-cell or K-cell) was mounted on the chamber opposite the evaporation stage, with the opening of the K-cell a few centimeters away from the sample. A movable shutter was placed between the sample and the evaporation source so that one could obtain abrupt starts and stops to depositions.

The previously described chamber was designed to be stationary and to be used for routine depositions and optimization of deposition parameters. A smaller and more portable deposition chamber was constructed to be moved to XPS/UPS facilities and attached to the XPS/UPS chamber for in-situ depositions. This chamber, being small did not have a loading chamber, or the capabilities of sample heating and temperature measurement. It did however have a thickness monitor as well as a gate valve for attachment to and isolation from the XPS chamber.

4.1.3 – Finding a suitable aniline oligomer

The physical vapor deposition technique is capable of producing films with thicknesses on the Ångstrom scale.[66] It was originally used for evaporating metals. It can also be used for making thin films of organics however many organics cannot be sublimed because they decompose before they make it into the vapor phase. There have previously been a few attempts at subliming polyanilines.[67-74] Those who have tried, claim that the polyaniline decomposes into small oligomeric fragments when heated in vacuum then re-polymerizes on the surface of the substrate.[67,71-73] Although there is some evidence to support this, the precise chemical structure of whatever gets deposited on the

substrate is not well known therefore it would be difficult to draw conclusions about what would be causing any observed effects.

An alternative is to use oligomeric polyanilines such as trimers or pentamers. Polyaniline oligomers are known to possess the same redox states as polyaniline.[75] Furthermore oligoanilines are also known to exhibit electrical conductivity[75-79] and corrosion inhibitive properties,[80] just as polyaniline does. Therefore oligoanilines are suitable model compounds for studying the Fe/PANI interface via in-situ XPS/UPS measurements on thin films.

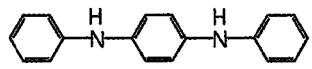

Phenyl-capped aniline dimmer (PCAD) with molecular weight 260.13amu.

We had attempted to use a phenyl-capped aniline dimmer (PCAD, a.k.a. N,N'-diphenyl phenylenediamine), however the substance had a detectible vapor pressure as soon as it was placed in vacuum. This makes it unsuitable because we will not have control over how much is being deposited on the surface of the substrate, and possibly it will not stick to the substrate. Furthermore the high vapor pressure of the molecule will cause the contamination of the analytical instruments. Due to the short mean free paths of electrons, photoelectron spectrometers need to be operated at pressures no higher than $\sim 3\times10^{-8}$ Torr. Even the small amount of PCAD placed into the evaporation chamber for evaporation would have caused the pressure to go no lower than about 10^{-5} Torr (this is an estimate as we never tried to put it in our vacuum chamber once temperature-

programmed mass spectrometry showed it had a significant vapor pressure at room temperature).

Amino-capped aniline trimer (ACAT) with molecular weight 288.14amu

We also tried an amino-capped aniline trimer (ACAT). This compound did not have a detectible background vapor pressure. It would form a vapor when heated close to 180°C. Attempts were made to evaporate this material onto iron substrates. When heated to above 180°C the quartz crystal monitor (QCM) detected the deposition of a film. On visual inspection of the film it had a slight purple color, and since the powdered form of ACAT is purple one might assume that the molecule was successfully deposited without decomposition. When investigated using AFM and SEM the film appeared to be a homogeneous coverage of micro-droplets as seen in figure 4.1.

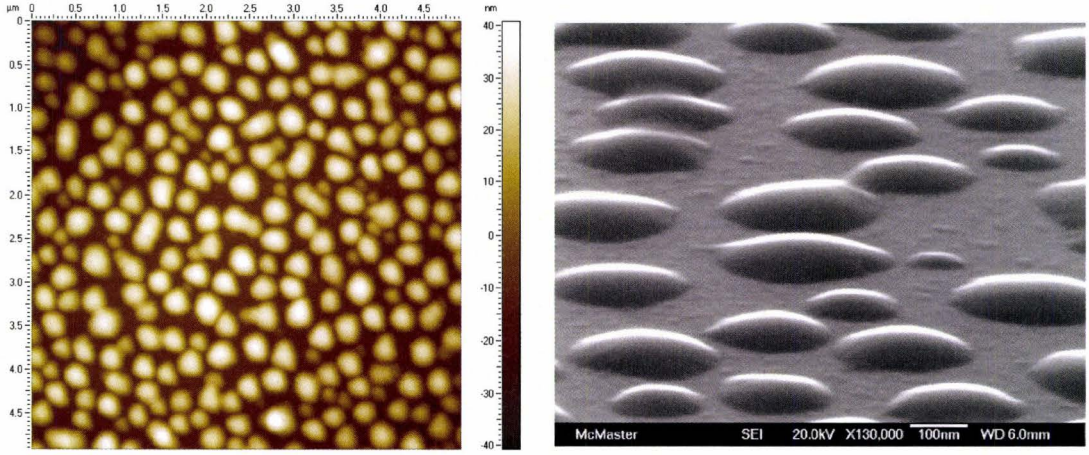

Figure 4.1 *- AFM and SEM images of a thin film formed as a result of condensation of the vapor produced by heating ACAT to 180°C.*

The evaporation behavior however changed after repeated evaporations. After being heated a few times the temperature required for evaporation would continuously rise. This was an indication that decomposition might be occurring, since a phase change would always happen at the same temperature. To investigate the matter further, differential scanning calorimetry measurements (DSC) were performed. These results showed a significant exothermic event occurring at around 180°C, which seemed like a phase change however upon heating the same sample subsequent times this feature would not re-appear (see figure 4.2). We then performed temperature-programmed mass spectrometry (TP-MS) and found that the vapor formed when heating for the first time to 180°C was rich in the desired compound as indicated by the large peak at ~290.1amu. Upon subsequent heating cycles the molecular peak would not return and only decomposition products would be present.

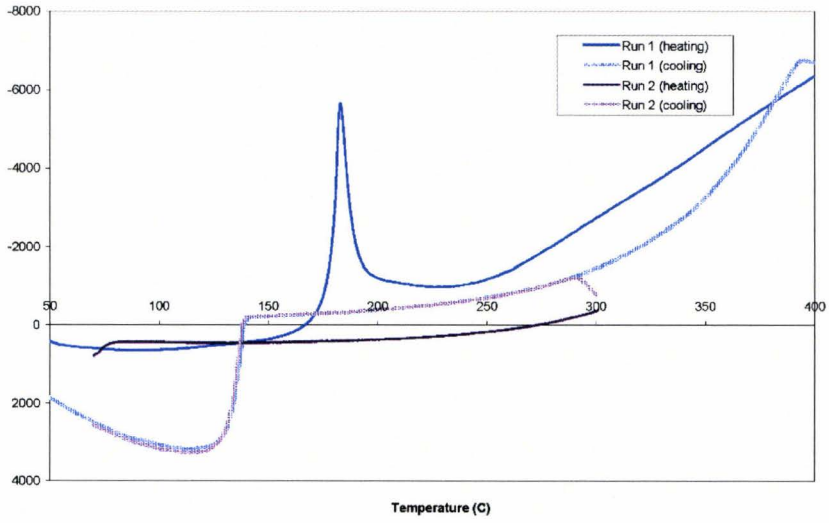

Figure 4.2 *– DSC curves for several heating cycles of ACAT.*

Since the peak of interest did show up on the first heating cycle, one would assume that the first deposition performed with a fresh batch of ACAT would yield a film of the desired material. In order to test this we evaporated a film onto a quartz slide instead of an iron substrate. The film-coated slide was then used to measure UV-vis absorption spectrum of the deposited-material, which was compared with the UV-vis spectrum of a solution-cast film of ACAT on a quartz slide. The two UV-vis spectra were distinctly different as seen in figure 4.3. The film was then washed from the slide and tested with mass spectrometry for comparison with neat ACAT. The spectra showed that the ACAT molecule was not present in the film (figure 4.4). This was the final piece of evidence to conclude that ACAT was decomposing when being heated and therefore could not be used to make vapor-deposited thin films.

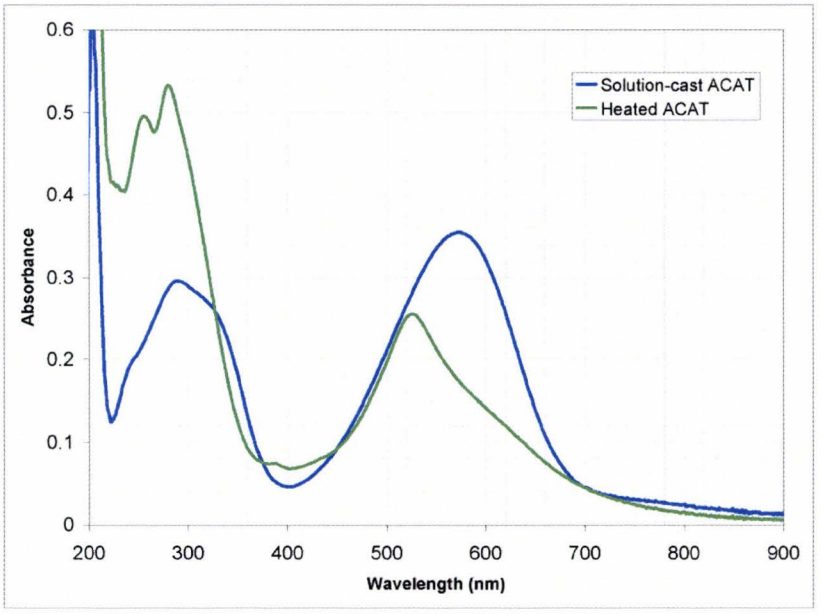

Figure 4.3 *– UV-vis absorption spectra of a solution-cast ACAT film and a film formed from heating of ACAT.*

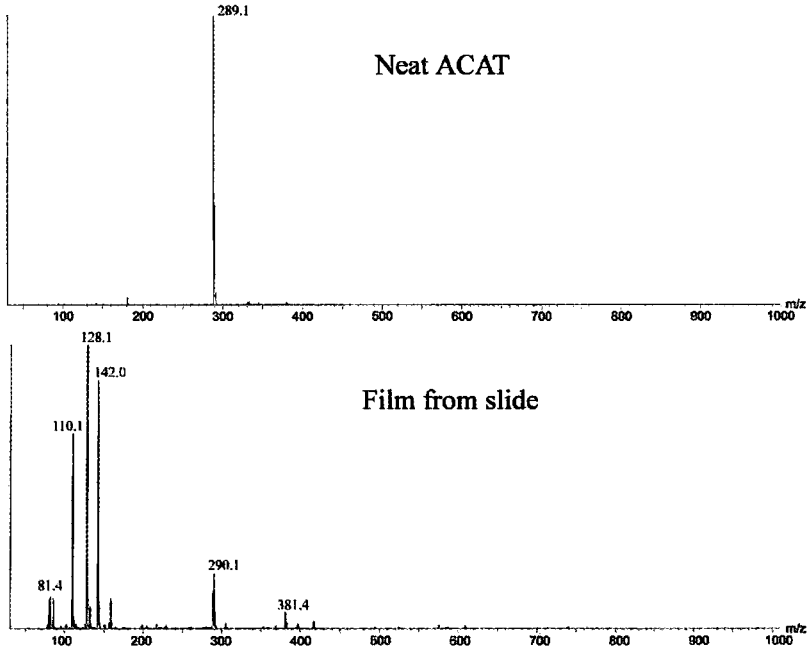

Figure 4.4 *– Mass spectra from neat ACAT and from film washed from quartz slide. The film on the quartz slide had been made by heating ACAT in vacuum.*

A different oligomer was then attempted. A phenyl-capped aniline tetramer (PCAT) was discovered in the literature, which was sublimable,[81] which had been found to inhibit corrosion[82] and whose crystal structure was also known.[83] Unfortunately PCAT is not commercially available however a thorough description of a synthetic procedure is available.[84] The compound was synthesized and purified according to the procedure.

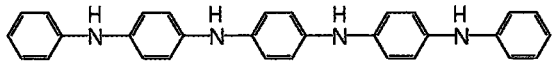

Phenyl-capped aniline tetramer (PCAT) with molecular weight 442.22 amu

Temperature-programmed mass spectrometry measurements were performed to test whether PCAT actually sublimes. The spectra showed that as the material is heated some small amounts of hydrocarbon impurities come off (see figure 4.5). Then at around 240°C the PCAT peak (244amu) came off at high purity. When the sample was

subsequently heated the contamination peaks would not return, but the PCAT peak showed up again at 240°C. This was good evidence that PCAT will sublime.

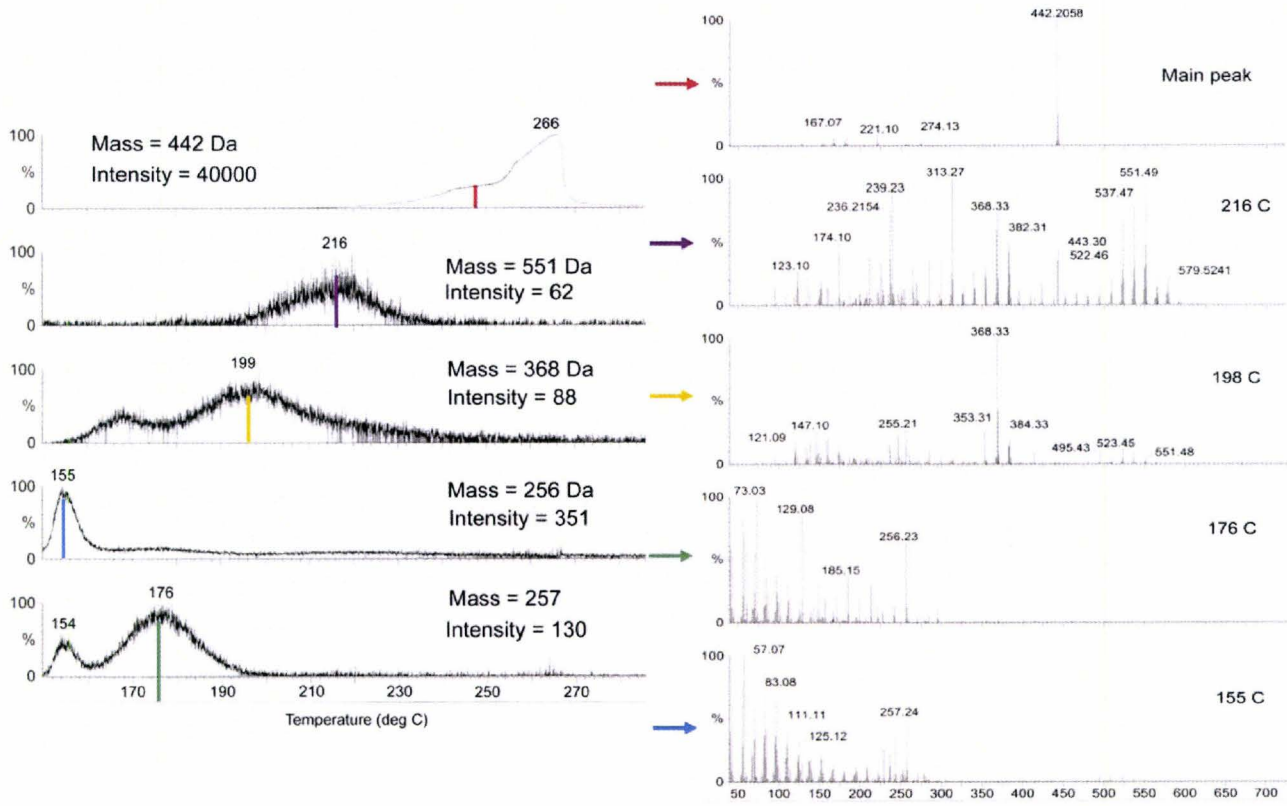

Figure 4.5 *– TP-MS of PCAT. On the left are chromatographs for the indicated masses (note the variation in intensity scale). On the right are the mass spectra taken at the indicated temperatures during the temperature program.*

A PCAT film was then evaporated onto a quartz slide, and UV-vis absorption spectra were taken of the film and compared with solution-cast films. The spectra were similar, except that the solution-cast film had an additional peak at around 600nm (figure 4.6). Polyaniline spectra found in the literature[85] showed that the oxidized form of PANI has a broad absorption around 630nm and a sharp absorption peak at around 310nm. The solution-cast spectrum exhibited similar features, with a broad absorption around 600nm and a sharp absorption around 305nm. The shift in absorbance values between the PANI spectra from the literature and the solution-cast PCAT spectrum is likely because the absorption wavelength for the short-chain polymer would be slightly different.

The UV-vis spectrum of the reduced form of PANI does not exhibit the broad absorbance peak and the sharp absorbance peak is shifted to ~340nm. The vapor-deposited film also did not have an absorbance at 600nm and had a sharp absorbance around 330nm. These results would indicate that there is some of the oxidized form of PCAT present in the as-prepared PCAT powder, but when heated to 240°C only the reduced form of PCAT sublimes and is deposited onto the substrate.

The vapor-deposited PCAT film was then washed from the slide and tested with mass spectrometry for comparison with the spectrum of neat PCAT. The spectra were identical. Given the several pieces of evidence indicating that PCAT sublimes before it decomposes, we concluded that this indeed was the case, and that this molecule was suitable for PVD film deposition and in-situ XPS/UPS experiments.

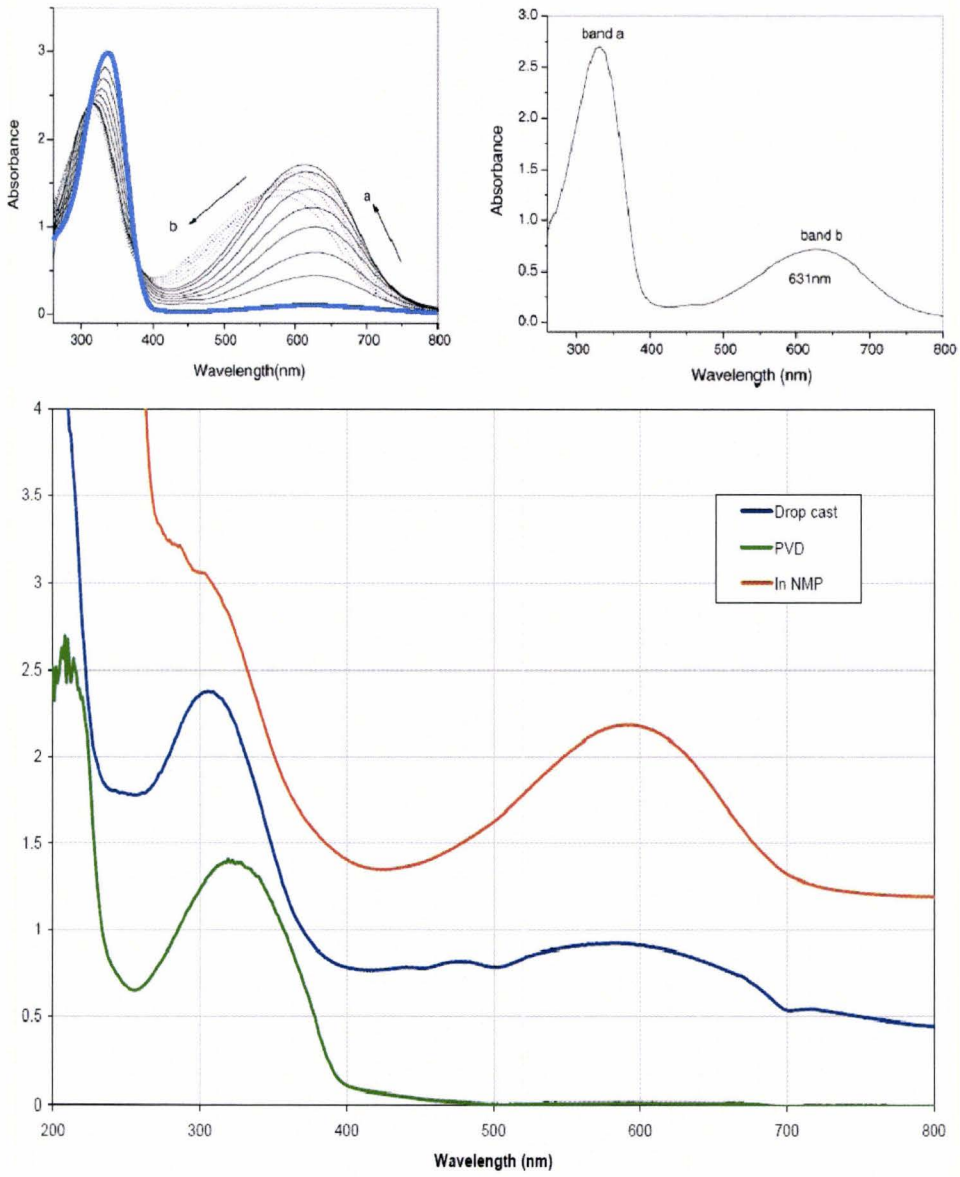

Figure 4.6 *- (top left) UV-vis spectra for various oxidation forms of PANI. The curve highlighted in blue is the fully reduced form. (Top right) [Ref. 85] The UV-vis spectrum of fully oxidized PANI. (Bottom) UV-vis spectra of PCAT dissolved in NMP (orange), PCAT drop-cast onto a quartz slide (blue) and film on quartz slide from heating PCAT (green).*

4.1.4 – Preparation of the substrate

The substrates used were low-carbon steel, essentially pure iron in its alpha phase, with a very small amount of impurities as determined by EDX. The material as received was in the form of 50mm × 100mm plates of thickness 0.5mm. The surfaces of the plates were formed during the crude manufacturing process. Therefore they were rough on the micron scale, and ill-defined in terms of morphology and presence of surface contamination. An SEM image of an as-received substrate is shown in figure 4.7. Due to the rough morphology and inhomogeneity of the surface it would not be suitable as-is for use in PEEM due to field emission from sharp protrusions when the 20kV required for PEEM is applied. Furthermore, XPS measurements give signals that represent an average over an area of approximately 400μm^2, so the surface should be homogeneous over this large of an area.

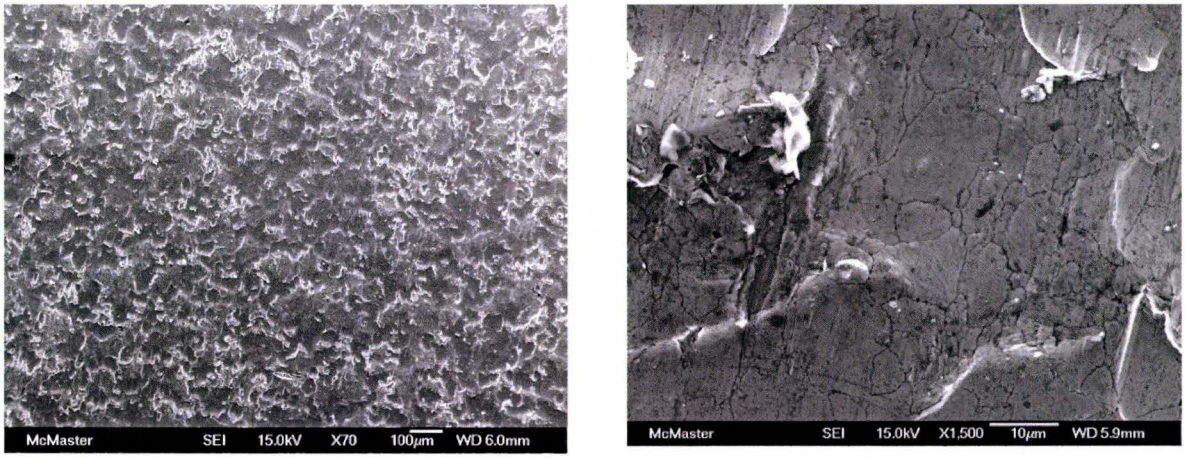

Figure 4.7 *– SEM images of un-treated (as-received) iron substrates. The rough surface topography was a result of the cold-rolling manufacturing process.*

The first step in making the samples suitable for analysis was cutting the sheets into 10mm×10mm squares and then mechanically polishing them to a mirror finish. The polishing was accomplished using an automatic polisher, starting with coarse grit silicon nitride emery paper and polishing with progressively finer grit paper. The final three polishing steps required micro-particle emulsions. First an emulsion of 3μm diamond particles combined with lubricating oil was used, followed by a 1μm diamond particle emulsion. Then an aqueous dispersion of 0.05μm alumina particles was used as the final polishing step. After the final polishing step all samples were washed with soap and water, and ultrasonically cleaned in acetone and methanol. The samples had a mirror finish when viewed with the eye. When viewed with SEM very little surface topography was evident as seen in figure 4.8.

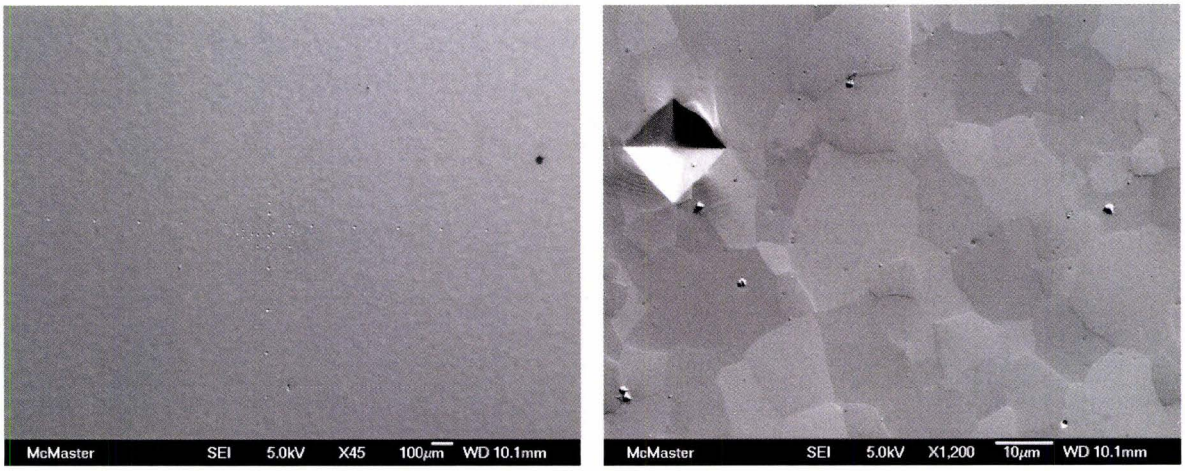

Figure 4.8 *– SEM images of mechanically polished iron substrates. The diamond-shaped feature on the top-left of the image on the right is an indent made by a Vicker's indenter, which was used to define a coordinate system on the substrates. In the image on the right the grains are discernable by the various contrasts of the different grains.*

The largest contributor to surface morphology comes from the grain structure of the material. The different crystallographic orientations of the various grains wear away at slightly different rates during mechanical polishing. While a flatter surface may be achievable if one could discover an anisotropic chemo-mechanical polishing procedure, the morphology we had attained was adequate.

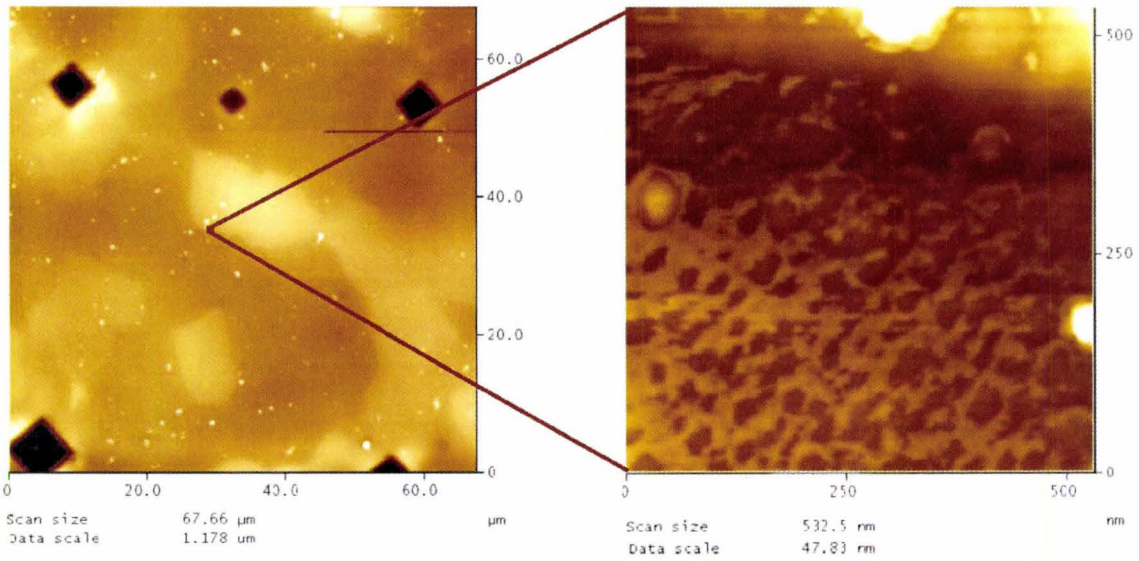

Figure 4.9 *– AFM images of a polished iron substrate. The left image has a 66.7µm scan size and the right image has a 0.532µm scan size. The grains are apparent in the left image. The right image shows the morphology of the oxide surface.*

A closer investigation into the surface morphology using AFM showed that each grain was relatively flat on the micron scale, with a slight curvature to them (see figure 4.9, left). The height difference from grain to grain was observed to be as large as 100nm and on average was around 50nm. Since the grains were on average around 15-20µm in diameter this meant that every 15 000nm there was a step of only 50nm. This is an aspect ratio of 300:1 which is reasonably good for our purposes. Upon zooming in closer one can discern morphology on a different scale (figure 4.9, right). This morphology was

attributed to the oxide on the surface. The morphology was disordered porous, with pore diameters around 20nm and pore depths of around 2nm.

There were also some particulates which did not seem very prominent under the SEM, but were very obvious when viewed with AFM. These could vary in size from 50nm to over 700nm in diameter and between 50nm and 200nm in height. EDX analysis indicates that these are some kind of oxide. Perhaps they are spots where some impurity nucleated the rapid growth of the oxide, or maybe they were spots where droplets of water were left to dry. Either way these particulates are a potential problem for analyzing our results so they should be removed. Furthermore the thin oxide coating the surface of the substrate is not well defined since it was formed during the final mechanical polishing step, which occurred in aqueous solution, where the oxide structure is very much pH dependant. Therefore, the structure of the oxide may vary from sample to sample. For these reasons it was decided to use a few more cleaning steps.

First, any possible carbon contamination was removed using a H_2/O_2 plasma. Then the samples were sputter cleaned with Ar plasma. This involved bombarding the surface of the samples with Ar^+ ions with a potential of 3kV. This step caused whatever oxide and small particles present on the surface to be blasted away. It also caused etching of the underlying metal. The result of this step will likely cause the first few nanometers of metal at the surface to be highly-deformed or amorphous. This was not considered to be a significant problem, since the amorphous metal will easily form oxide upon exposure to atmosphere. All samples were exposed to atmosphere to re-grow the oxide. Re-growth of the native oxide is important for our study because we believe that PCAT acts on the oxide rather than the metal, since all previous studies showing corrosion

resistance were performed in ambient conditions, where a surface oxide will always be present. Since all our samples underwent the same plasma-etching treatment we assume they all had nearly the same surface oxide. Previous studies have shown that during ambient atmospheric oxidation of iron a thin oxide grows and its thickness saturates very rapidly.[51]

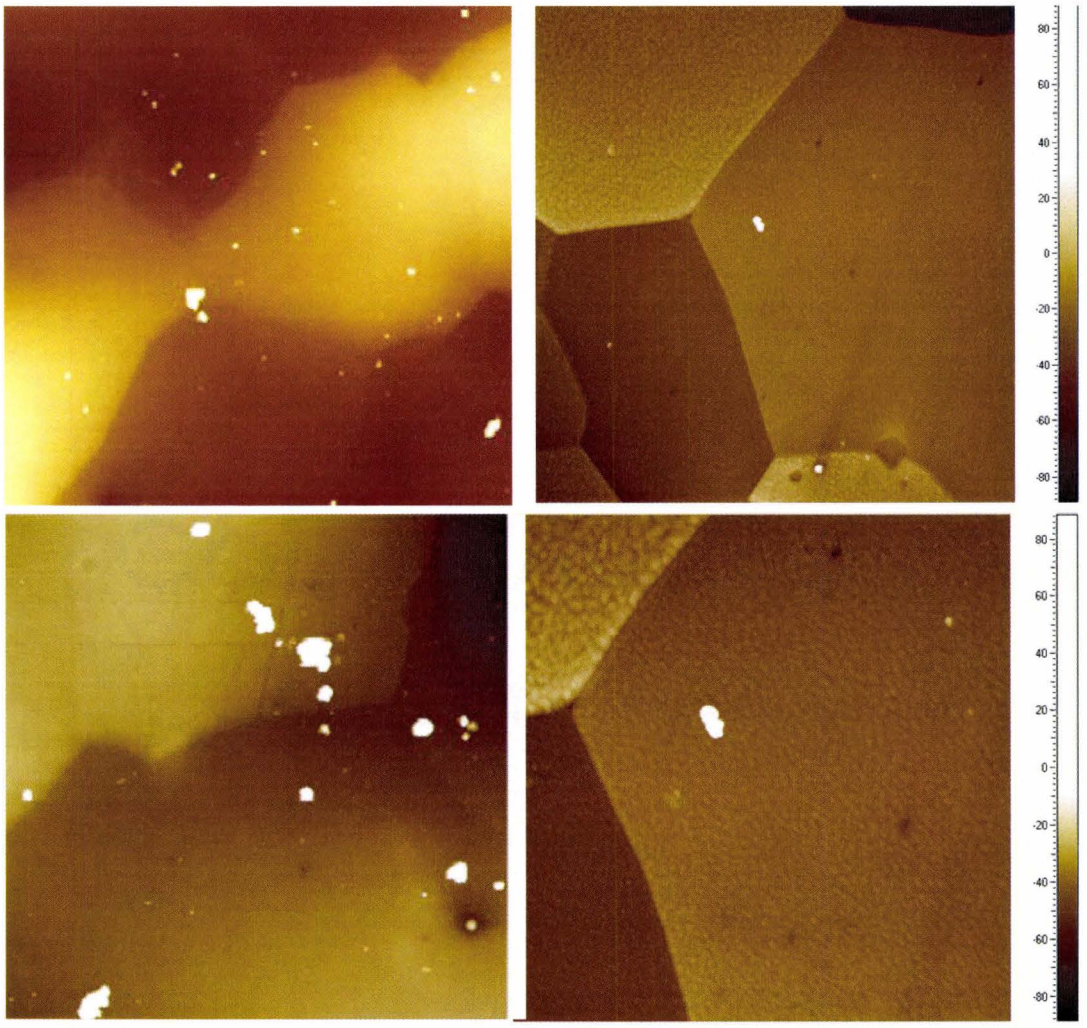

Figure 4.10 *– AFM images of pre-sputtered (left two images) and post-sputtered (right two images). The top two images have scan sizes of 20μm and the bottom two 10μm.*

In order to confirm that the sputtering treatment removed the particulates and did not do too much damage, the samples were investigated after sputtering treatment. The AFM images (figure 4.10) reveal that the majority of the particulates have been removed and the surfaces of the grains have been made more uniform. However the different crystallographic orientations have different sputtering rates, and while the difference in height from grain to grain did not change significantly from how they were before sputtering, the edge from grain to grain became sharper and more distinct. This was not expected to be a problem.

To confirm that we had removed the oxide we performed in-situ argon sputtering and examined with XPS (figure 4.11). After 5 minutes of sputtering the XPS spectra showed a major reduction in the oxygen 1s peak intensity and a complete disappearance of the carbon 1s peak. The Fe 2p peaks for oxidized Fe were replaced by the Fe 2p peak for metallic Fe.

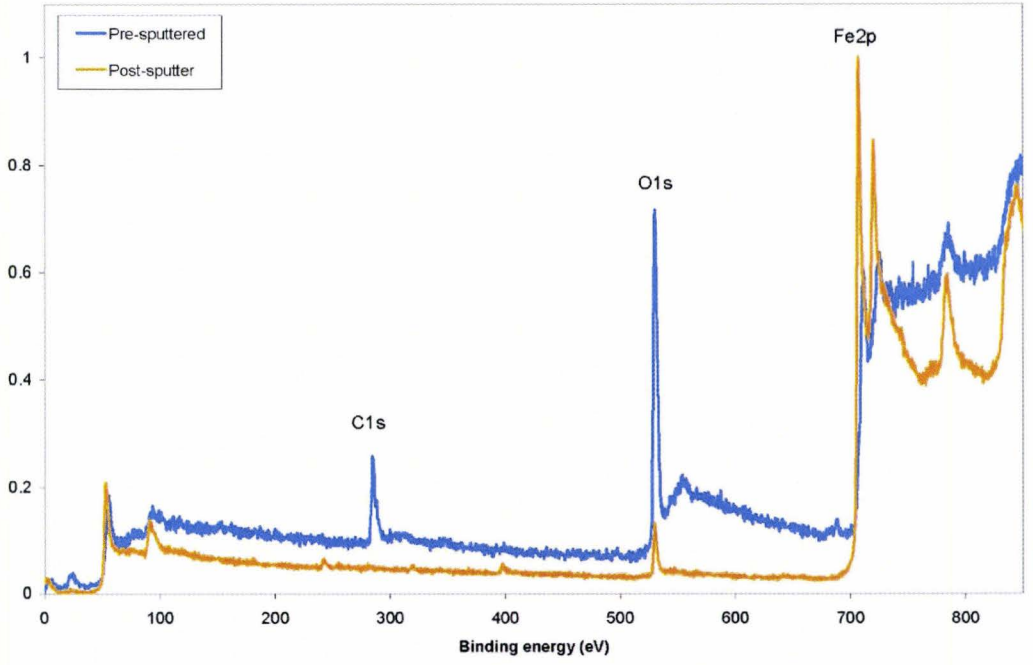

Figure 4.11 *– XPS survey spectrum for pre-sputtered (blue curve) and post-sputtered (orange curve) iron substrate.*

4.2 – PEEM experiments

The PEEM experiments were carried out using an Elmitec PEEM III, attached to the Plane-Grating Monochromator (PGM) beamline at the Canadian Light Source (CLS) in Saskatoon, Saskatchewan. The PGM is capable of delivering high-intensity, monochromated photons within the energy range of 5.5 to 250eV, which is considered ultraviolet to very-soft X-ray radiation.

The PEEM was equipped with a hemispherical band-pass electron energy analyzer in order to perform spectro-microscopy analysis. The microscope consisted of a main chamber, where the sample would be positioned during analysis. The base pressure of this chamber was in the 10^{-9} Torr range, being pumped on by an ion pump. The magnetic lenses, energy analyzer, channel multiplier and phosphore screen were housed in the 'imaging column', which was maintained at a pressure in the 10^{-10} Torr range. The main chamber was attached to a sample preparation chamber, which consisted of an argon sputter gun for sample cleaning as well as a K-cell and deposition monitor for performing in-situ depositions. This chamber was kept at around 10^{-8} Torr.

Samples were imaged using either the synchrotron as a photon source or a Hg-lamp, which was attached to the side of the main chamber and focused at the sample. When imaging with the Hg-lamp the microscope was in 'total yield' mode. No spectroscopy was performed using the Hg lamp. When using the synchrotron as the photon source imaging was performed in 'total yield' as well as 'energy filtered' mode.

A photon energy of 160eV was used in all experiments because it was found to give the sharpest valence features and was also capable of photo-ejecting from the Fe3p states. When using 'energy filtered' mode to perform spectroscopy an energy slit and

contrast aperture were inserted into the electron path to give an energy resolution of 0.5eV. All photoemission spectra scanned a kinetic energy range from 90 to 155eV, which on the binding energy scale is from -2 to 63eV.

Two types of analysis were performed; (1) imaging and spectroscopy of a PCAT film edge and (2) spectroscopy of in-situ, step-by-step deposition of a PCAT film. All substrates were polycrystalline iron, and were prepared as described in section 4.1.4. There were two of samples used for the 'film edge' study; a sample which was prepared ex-situ and one which was prepared in-situ.

The ex-situ 'film edge' sample was prepared in the stationary deposition chamber in Hamilton, which is described in section 4.1.2. The film edge was formed by using a piece of tantalum foil as a mask to cover half of the substrate surface during PCAT deposition. The PCAT film thickness for this sample was approximately 10nm thick. This sample had been exposed to atmospheric conditions for several weeks before analysis at the CLS. Imaging and photoemission spectroscopy was performed according to the routine mentioned above (i.e. $h\nu$ = 160eV, kinetic energy from 90 to 155eV)

The in-situ 'film edge' sample was prepared in the deposition chamber attached to the PEEM. The film edge was accomplished by placing a thin molybdenum washer over the substrate surface and depositing approximately 15 to 20nm of PCAT. The sample had to be briefly exposed to atmosphere in order to remove the molybdenum washer. Imaging and spectroscopy were performed on this sample as described above.

The second set of analyses performed on the PEEM was the in-situ, step-by-step deposition. Before any PCAT was deposited, the blank substrate was placed into the microscope to acquire photoemission spectra. The sample was then moved to the

deposition chamber, and a thin (between 5 to 10Å) film of PCAT was deposited, by heating the K-cell to ~240°C and holding the sample in front of the K-cell aperture for about 1 second. The sample was then transferred back to the main chamber for spectroscopic analysis. Four more layers of PACT were deposited in this manner, with spectra acquired after each deposition. After the last spectrum, a sixth deposition was performed in order to achieve bulk PCAT. This was done by exposing the sample to the PCAT vapor for two minutes. The sample was once again analyzed.

4.3 – XPS and UPS analysis of PCAT films using lab-based photon sources

In order to obtain high-resolution UPS and XPS spectra as well as work-function measurements, an in-situ step-by-step PCAT deposition was performed on a lab-based photoemission spectrometer. This experiment was carried out at the Toronto Microanalysis Center at the University of Toronto. The spectrometer was a PHI 5500, using a hemispherical energy analyzer with an energy resolution of 0.05eV. For XPS analysis, a monochromated Al Kα photon source ($h\nu$ = 1486.3eV) was used and for UPS analysis a He lamp ($h\nu$ = 21.2eV) was used.

In order to perform in-situ depositions, a portable deposition chamber was attached to the transfer chamber of the spectrometer. The substrates were polished, poly-crystalline iron, as described in section 4.1.4. Once the samples were placed into the spectrometer they were sputter cleaned for 15 minutes with 3kV Ar^+. An XPS survey spectrum was taken to ensure cleanliness of the substrate. The sample was then placed into the loadlock and re-oxidized by exposure to atmosphere; however a flow of dry

nitrogen was flushed over the sample during re-oxidation in order to minimize the amount of carbon contamination.

Core and valence photoelectron spectra were then obtained for the clean substrate. Three deposition steps were performed. The first two depositions were thin layers, and the third deposition was a thick layer. Spectra were obtained after each deposition. The spectra which were obtained are as follows; For XPS the Fe2p, C1s, N1s, O1s, and Fe3p core photoemission spectra were acquired. The energy resolution used for the XPS spectra was 0.125eV. For UPS spectra the valence and secondary cut-off were obtained by scanning energies from -3 to 16eV. The resolution for UPS spectra was 0.05eV.

Chapter 5 – Results and discussion

5.1 - Morphology of PCAT films

In order for spectroscopic investigation of the step-by-step depositions to be successful, so that one can observe peak shifting in the substrate and in the overlayer as the film thickens the film must form in a layer-by-layer fashion. If this is not the case, and the film grows as islands then the interface structure will not be probed by the spectroscopy. When growing thin films of metal or covalent solids, island growth is common and can be a problem for this type of study if the islands grow too fast in the direction perpendicular to the surface compared to how fast it grows in the directions parallel to the surface.[66] The reason why island growth often occurs in such systems is that there is lattice strain at the interface between the two materials when their lattices attempt to match.[66] The lattice strain can make the interfacial surface energy too great compared with the energy required to form more overlayer surface area so that uniform coverage of the substrate by the overlayer unfavorable.

Lattice strain however is not usually a problem for molecular organic films[89] because they do not form covalent solids, therefore the driving force for being a highly ordered lattice is not very strong. Molecular organics usually grow as amorphous films, or under certain conditions they can be crystalline,[90] but the organic lattice makes little attempt to match with the lattice of the substrate. For layer-by-layer growth of organic films it is more important that the polarities of the organic and the surface match, at least as much that the molecules do not have an overwhelming preference for inter-molecular bonding with its own molecules rather than the substrate.

The iron oxide surface is expected to have a large dipole,[91] while the dipole moments in PCAT are somewhat small. AFM investigation of vapor-deposited PCAT films showed uniform coverage and morphology that suggested the films were amorphous, and have no problem wetting the oxide surface. Below (figure 5.1) are AFM height images of a clean, oxide-covered iron substrate and a 5nm-thick PCAT film on such a substrate. One can see that the porous surface topography of the oxide is completely covered by the PCAT over-layer. This indicates that a PCAT film of 5nm thick will not de-wet from the oxide surface.

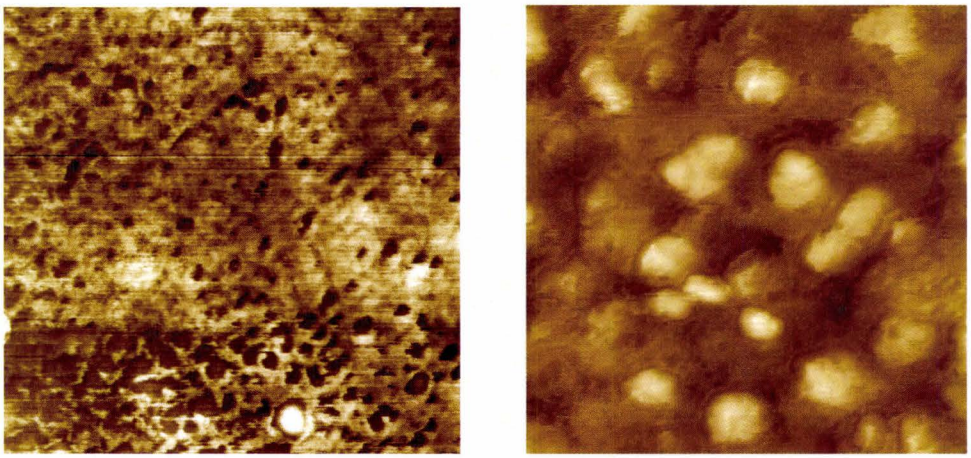

Figure 5.1 *– AFM height images of oxide-covered iron substrate (left) and 5nm-thick PCAT film (right). Both images are 750nm×750nm.*

As thicker films were deposited the surface morphology changed, as seen in figure 5.2. The root-mean-squared roughness (R_{rms}) of the 5nm film was ~1.2nm, while the R_{rms} of 10nm and 100nm films was ~2.5nm and ~5.8nm, respectively. Root-mean-squared surface roughness values however often do not adequately represent the surface morphology, so a qualitative description is often more valuable. The 10nm film consisted of two types of surface features, bumps of ~80nm diameter and ~4nm high and bumps of ~80nm diameter and 20-25nm high. The 100nm film also consisted of two types of

surface features, bumps of 160nm diameter and 16nm height, and bumps of ~250nm diameter and ~50nm height.

Based on these observations the following growth mechanism is proposed. The first few mono-layers of PCAT completely cover the substrate surface. These first few Ångstroms of overlayer are not of perfect uniform thickness, but good enough for electron spectroscopy of the interface. As PCAT is continually deposited the film becomes less uniform. Some sites on the surface nucleate into growing spherical globules of amorphous PCAT. As the film continues to thicken, some of these globules grow faster than others, causing a coarsening and roughening of the film morphology.

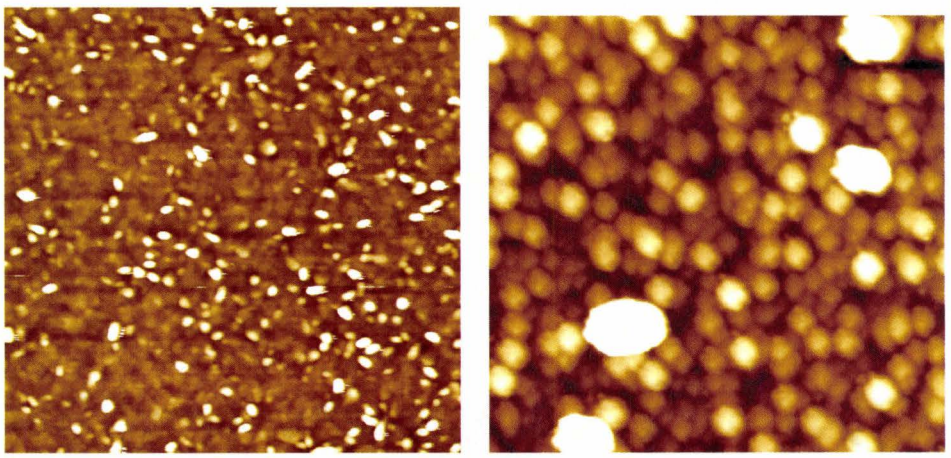

Figure 5.2 *– AFM height images of 10nm-thick (left) and 100nm-thick (right) PCAT films on iron substrates. Both images are 2μm×2μm.*

5.2 - Morphology of PCAT films edges

In order to examine the possibility of the 'remote effect' with PEEM, samples had been prepared where a mask was applied to the substrate, so only half the substrate was coated. This way the samples had a distinct film edge which could be viewed with PEEM and the substrate's photoelectron spectra could be acquired close to the termination of the

film. When investigating the edge of the films with AFM it was found that PCAT had a different morphology at the film edge than in the center of the film, and that the film extended a few microns past the edge of the mask (See figure 5.3).

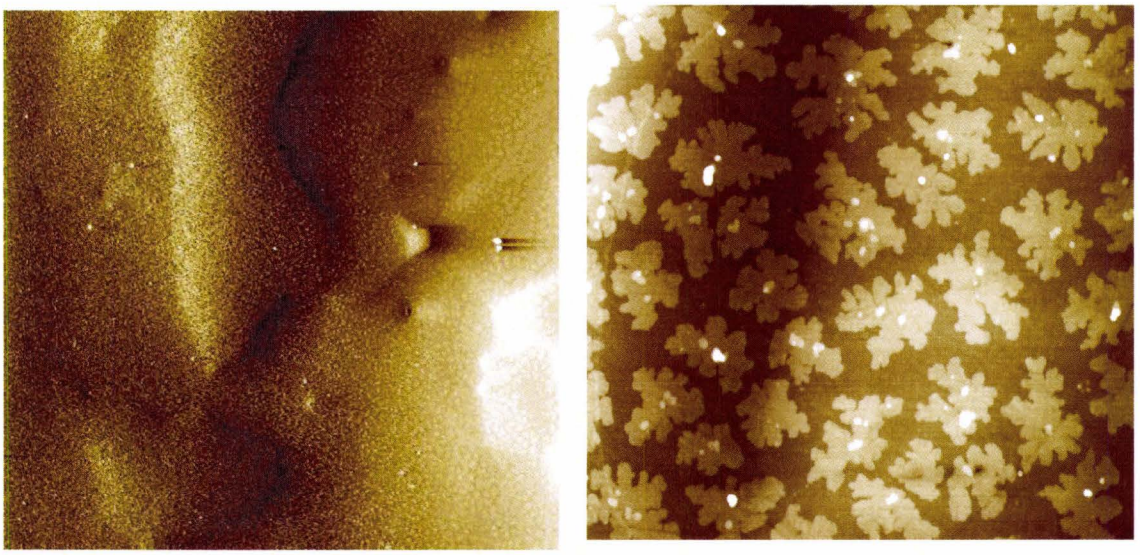

Figure 5.3 *– AFM images of 100nm-thick PCAT film near the film edge. The left image is 40μm×40μm. Substrate on the right-half of the image was covered by a mask during deposition. The image on the right is a zoom in of the image on the left. It is 4μm×4μm.*

In figure 5.3, at 40μm scan size both film morphologies can be seen. On the left half of the image there was no mask during deposition, and it has the amorphous morphology discussed above. The substrate on the right half of the image was covered by the mask during deposition. It has a more coarse structure than the amorphous film. Closer investigation of the coarse film revealed that it consisted of dendritic islands. The dendritic morphology indicates some degree of crystallinity, although probably still somewhat amorphous since the islands lack symmetry.

The reason for spreading of the film underneath the mask is likely due to thermal migration of PCAT molecules along the substrate surface. The different film morphology

for the film underneath the mask is a result of the fact that no PCAT molecules are impinging on the surface from the vapor phase underneath the mask. The film underneath the mask nucleates and grows based on surface migration kinetics.

Due to their high kinetic energies of the PCAT molecules diffusing under the mask and due to the lower flux of molecules underneath the mask causes the film under the mask to be more crystalline than the film directly exposed to the PCAT vapor, which is amorphous. Dendritic islands are formed instead of polyhedral islands because the growth of the islands was diffusion limited.

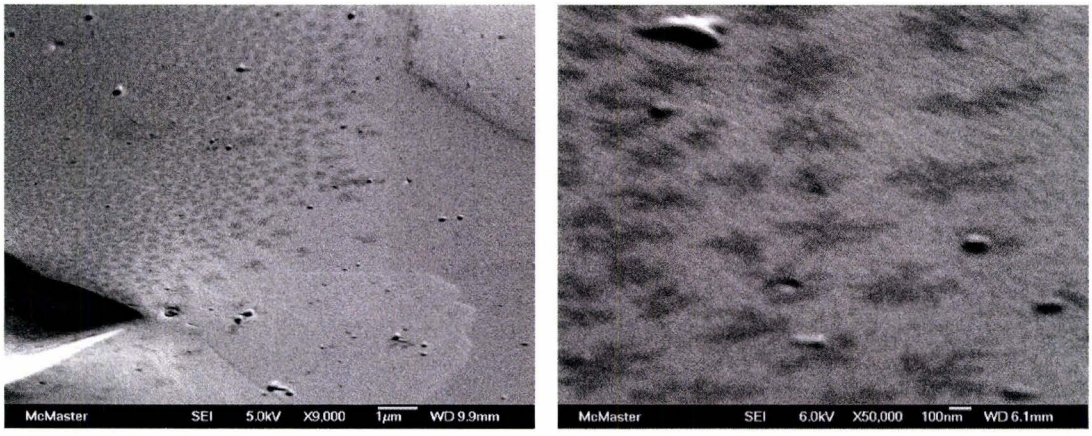

Figure 5.4 *– SEM images of dendritic islands at the film edge of a 10nm-thick PCAT film on iron.*

The film was also investigated with SEM (see figure 5.4), however the dendrites were much more difficult to resolve with SEM than with AFM. This is because AFM is more sensitive to changes in height on a surface, while SEM is more sensitive to changes in surface angles. Furthermore, the SEM signal comes from dozens of nanometers into the bulk of a sample,[93] so it is not very surface sensitive. The dendritic islands were only about 3.5nm thick, so the signal probing the islands was convoluted with a more intense signal from the bulk, making them somewhat difficult to observe with SEM.

5.3 - PEEM study of photoemission intensity near PCAT film edges

The purpose of using PEEM to studying PCAT films was to examine how the photoemission features of the iron substrate may change in proximity to the PCAT film. Therefore samples were examined close to the film edges. To begin with, it was important to become familiar with the photoemission features of the clean substrate. Figure 5.5 shows PEEM images of a polished, sputtered and re-oxidized iron substrate at 100μm FOV. At this FOV, when the polished substrates were illuminated with a mercury

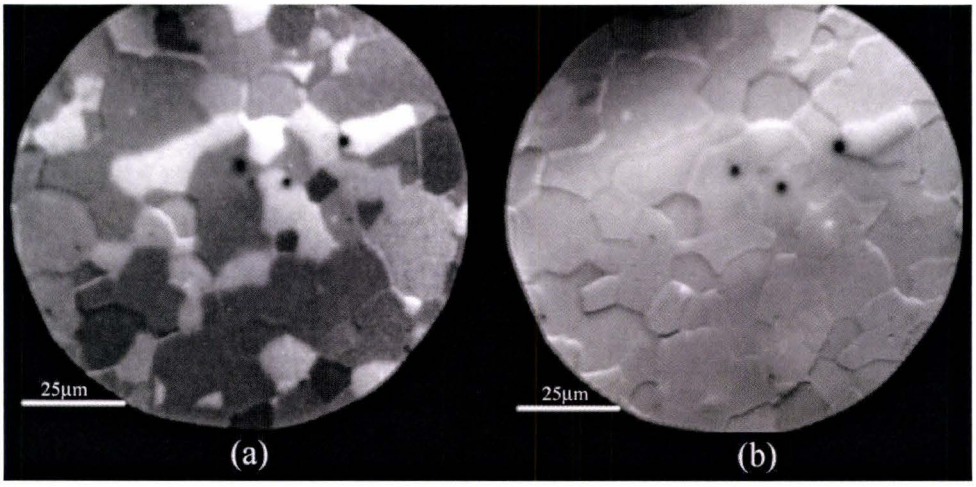

Figure 5.5 *– PEEM image of polished Fe sample illuminated by (a) Hg lamp (b) synchrotron radiation of 160eV*

lamp (maximum excitation energy ~4.9eV) the substrates looked like a mosaic of grains (see figure 5.5a), with a strong contrast between the various orientations. When the sample was illuminated with synchrotron radiation of higher energy (we used 160eV) the grains could still be discerned due to the topography difference between them, however the work function contrast was not as prominent (see figure 5.5b). This is due to the fact that when illuminating with higher energy light the secondary electrons no longer

dominate the spectrum, and therefore changes in work function no longer have as large an effect on total electron yield.

Once the appearance of the clean substrate was known, a sample with a distinct film edge was investigated. Since it is not really certain on what length scale the 'remote effect' spans (some have claimed it is in the microns range, while others in the hundreds-of-microns range[92] and others even the millimeter range[5]) we began the study with the largest field of view (FOV) the PEEM was capable of, which was 100μm.

The sample about to be discussed was prepared in-situ, and analyzed immediately after preparation; however it had to be briefly exposed to atmosphere in order to remove the mask to see the film edge. The edge of the film was easy to locate with PEEM since its appearance was distinctly different from the substrate. When the Hg lamp was used to

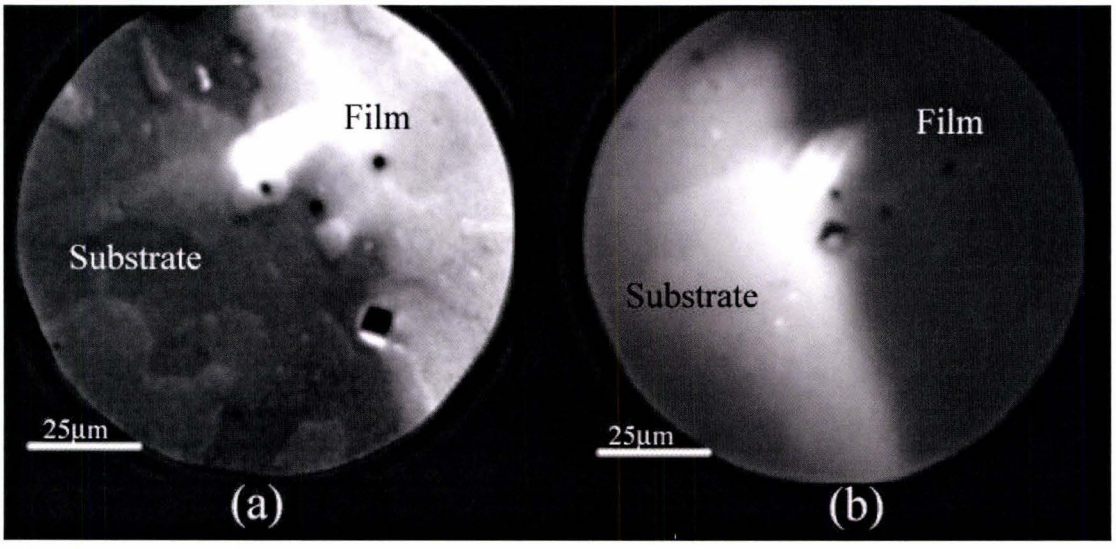

Figure 5.6 *– PEEM images of PCAT film edge illuminated (a) with Hg lamp and (b) with 160eV synchrotron radiation.*

illuminate the sample the substrate would always show the mosaic of contrast from the grains while the film had a uniform brightness (see figure 5.6a). The fact that the film appeared uniform was because the film had a uniform work function and was thick

enough to bury the signal from the substrate. With the Hg lamp the film also appeared brighter than the substrate. This would indicate that either the film has smaller work function than the substrate, or that the film has a larger photoemission yield than the substrate. When illuminated with 160eV synchrotron radiation however the film appeared darker than the substrate (figure 5.6b). Since the images taken when the sample is illuminated with 160eV are more sensitive to total photoelectron yield than to work function difference it is clear that the photoemission yield for the film is actually lower than that of the substrate, which would also imply that the reason why the film appears dark in the Hg-lamp image is because the film does in fact have a smaller work function than the substrate.

It makes sense that the PCAT film should have a lower work function than the substrate since work function is a surface property, and the surface of the substrate is the termination of a covalent solid (the oxide), while the surface of the PCAT film is the termination of a molecular solid. Therefore the oxide will have a large surface dipole, leading to a large surface-to-vacuum energy barrier, while the PCAT film will have a smaller surface dipole due to the fact that it is a molecular solid and the surface does not require the termination of covalent bonds.

In order to confirm that the film edge being seen in PEEM was in fact the PCAT film edge X-ray absorption spectroscopy (XAS) was performed in conjunction with the PEEM. This was done on the Spectro-Microscopy (SM) beamline at the CLS. X-ray absorption spectra are achieved by measuring the photoemission intensity while scanning the photon energy. We scanned energies from 360eV to 820eV, which allowed observation of the nitrogen K-edge (~410eV), the oxygen K-edge (~543eV) and the iron L-edge (~707eV). By using the PEEM as the photoemission intensity detector we were able to obtain spatially resolved spectra. A spectrum and PEEM image for the edge of a 10nm film is shown in figure 5.7. It can be seen that off the film there are only O and Fe signals, while on the film there is only signal from the nitrogen, and the O and Fe signals are buried. This evidence supports the belief that the film edge is that of the PCAT film.

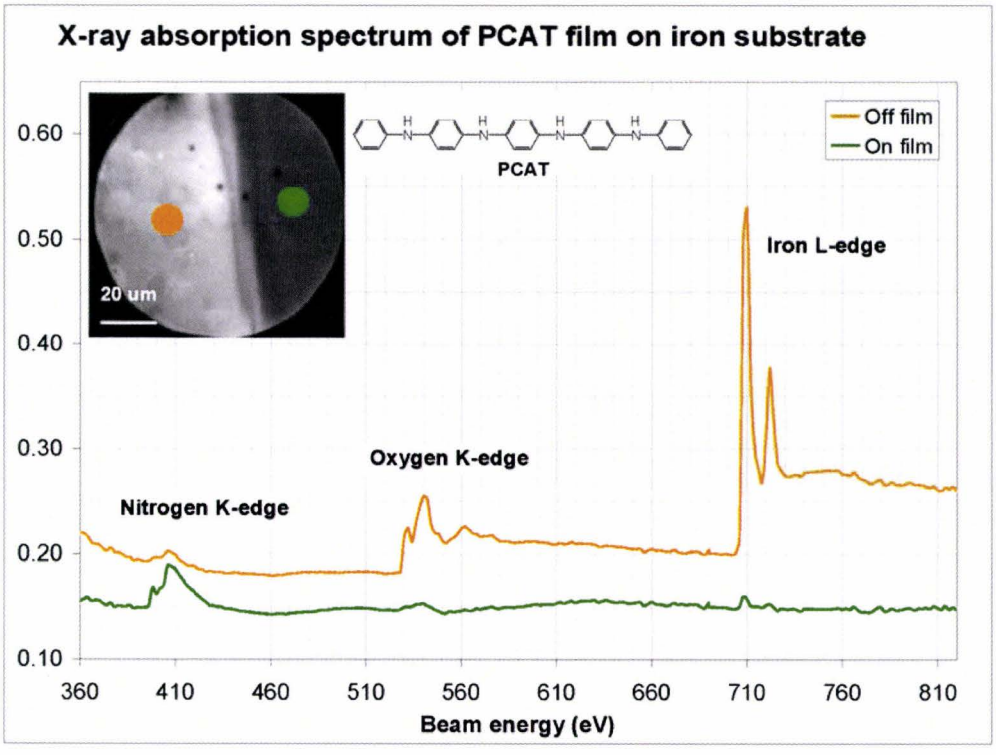

***Figure 5.7** – XAS of PCAT film edge*

Once the film edge had been located, spectro-microscopy stacks were acquired. A beam energy of 160eV was chosen because it was found to give sharp valence features

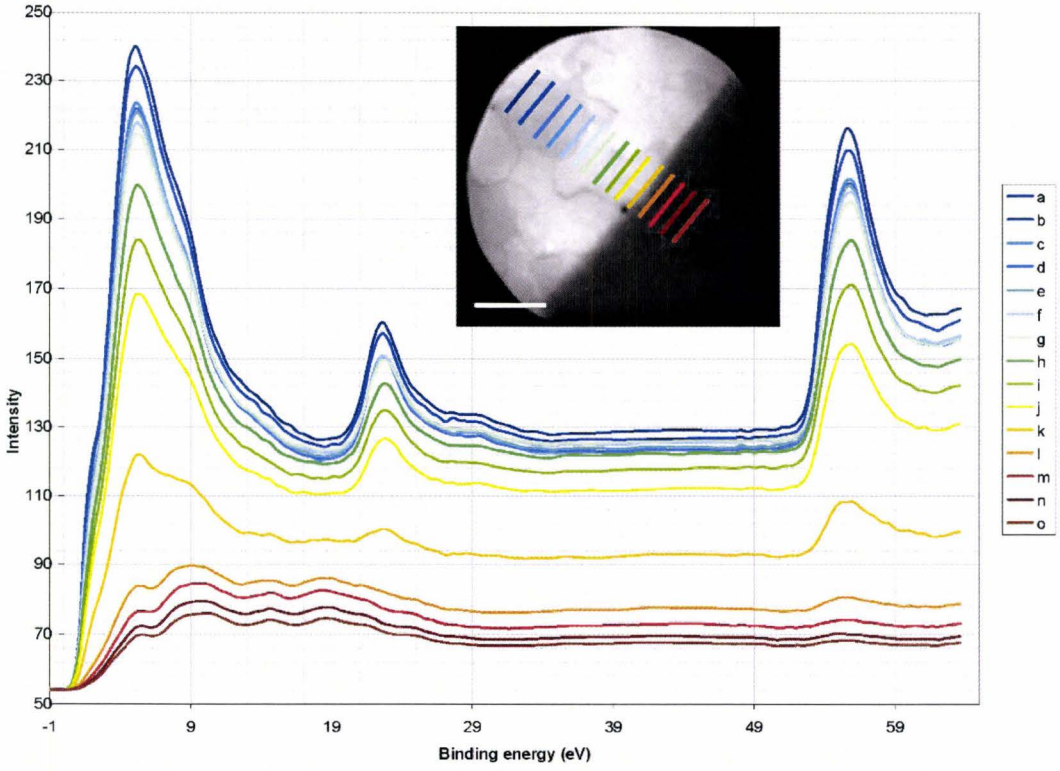

Figure 5.8 *– Photoemission spectra (hv = 160eV) and PEEM image (FOV = 100μm) near a PCAT film edge. The more intense spectra are from the substrate.*

and was also of high enough energy to include the Fe3p photo-emission peak into the spectra. A series of spectra taken near the film edge are shown in figure 5.8.

These spectra have not been normalized, so their relative intensities are as collected from the PEEM. They confirm that the PCAT film has a lower photoemission yield than the substrate since the intensity of the PCAT spectra are overall about 1/4 the intensity of the substrate spectra. The difference in photoemission yield is likely due to

the higher density of valence states near the Fermi level of the substrate compared to the PCAT film. Since iron and Fe_3O_4 have significant band dispersion they will have a somewhat high density of states near the Fermi level. PCAT however is a molecular solid, so if there is dispersion (there is still some debate as to whether molecular solids form dispersion bands) then it is likely very narrow. If there is no dispersion then electrons are being photo-emitted from discrete valence states, which makes the effective density of states for each photo-emission event lower than in the substrate.

Since the purpose of this investigation was to look for evidence of a remote effect we wanted to see whether the spectrum of the substrate changes close to the PCAT film. From figure 5.8 it seems like the photo-emission yield of the substrate diminishes close to the film edge. However, there is a problem with the current design of PEEM microscopes; a flat surface of uniform composition will not appear with uniform brightness in the PEEM image. For the microscope we were using there was always some 'pinching' in the image. Pinching means that certain areas near the edges of the image would appear darker than the rest as seen in the in figure 5.6(b) at the bottom-left portion of the image. The pinching leads to artifacts in the intensity of spectra taken from across the image.

In the PEEM image of figure 5.8 one can see that the substrate appears slightly darker near the top-right and bottom left of the image. The spectra shown in figure 5.8 were obtained by averaging over rectangular strips parallel to the film edge as shown in figure 5.9. Since these pinching regions are coincidentally close to the film edge, averaging the spectra over the strips may lead to a decrease in intensity close to the film edge, which is actually an artifact of the microscope.

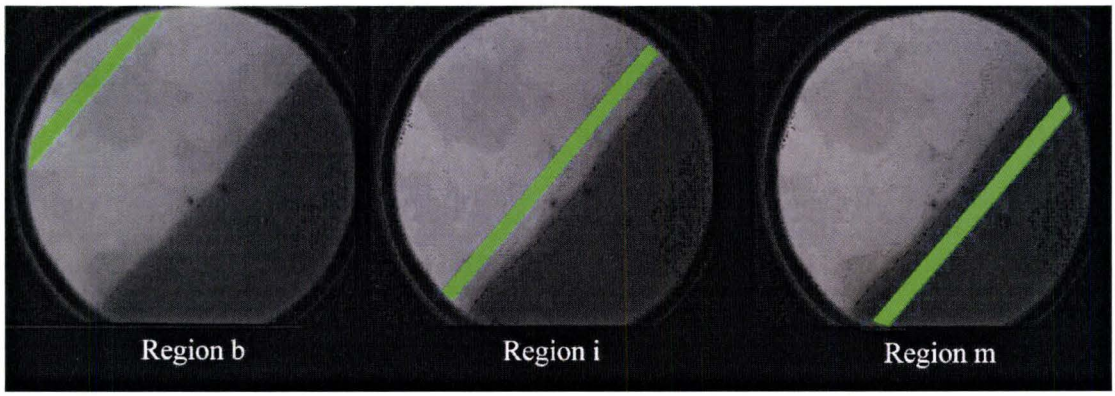

Figure 5.9 *– PEEM images showing some regions where spectra were averaged from for the curves in figure 5.8. Images are energy filtered mode, FOV = 100μ, hv = 160eV*

In order to determine whether the intensity attenuation close to the film is an artifact or not the spectral average was taken from smaller regions (i.e. squares instead of long strips). This way the effect of uneven brightness across the image will be minimized. Spectra were averaged over smaller regions according to figure 5.10(left). These regions were chosen because there was the least pinching of the image in that area. Even with the effect of pinching minimized still there is contrast between grains, which is an effect that might convolute with any dimming of the intensity near the film edge. Figure 5.10(right) shows a plot of the Fe3p peak intensity with distance from the film edge. Here the changes in intensity between 30-45μm is due to the difference in intensity between different grains. Close to the film edge (from 0 to 15μm) there is a rapid drop in intensity.

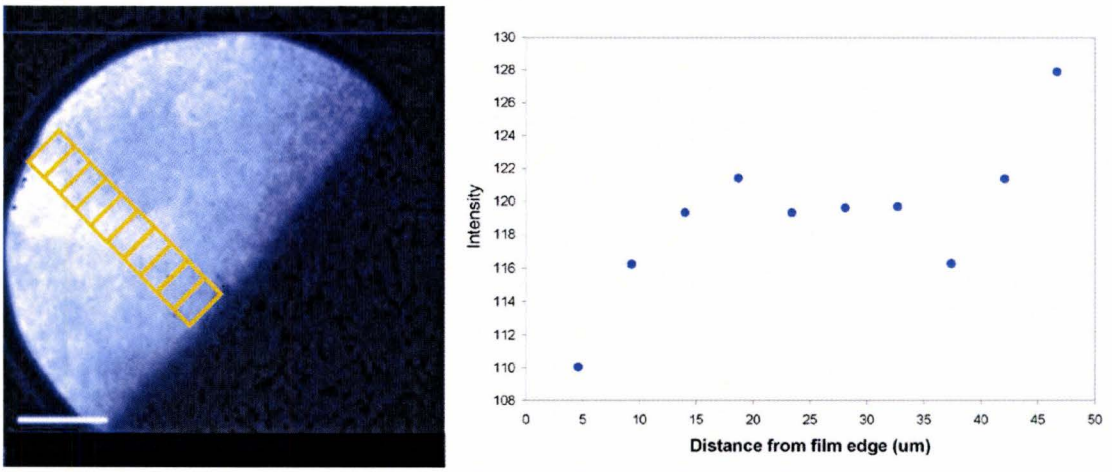

Figure 5.10 *– (left) PEEM image showing regions where spectral intensity was averaged.*
(right) plot of spectral intensity vs. distance

Due to the convolution of effects of image pinching and grain contrast any conclusions about this drop in intensity near the film edge are not necessarily reliable. However assuming the effect is real then there are a few possible causes for such an effect. It could be caused by small amounts of PCAT on the substrate close to the film edge. PCAT has a lower photoemission yield than iron oxide and therefore its presence even in sub-monolayer amounts would make the image darker. As was discussed in section 5.1, PCAT was found to be capable of spreading underneath the deposition mask. However the spectra close to the film edge did not show any signature of the PCAT valence band, although such signatures may not be apparent in a spectrum if the amount of PCAT there is very low.

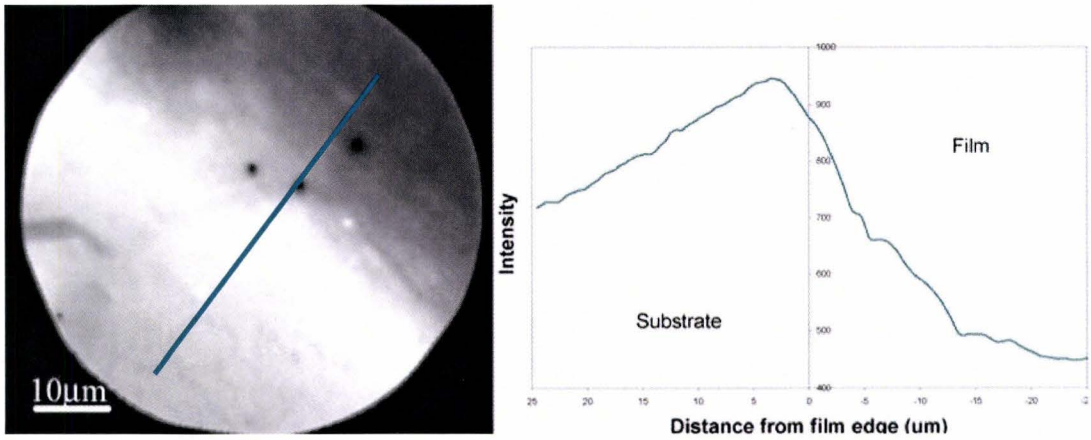

Figure 5.11 *– (left) PEEM image (FOV = 50µm, hv = 160eV) in 'total yield' mode of PCAT film edge. (right) intensity vs. distance profile for direction perpendicular to the film edge.*

The above analysis of image intensity near the film edge was for energy-filtered images, so the work-function does not play a part in the image intensity. In order to see whether there is a change in intensity near the film due to a work function change one needs to analyze the images from total electron yield mode. An image of the film edge using 'total yield' mode is shown in figure 5.11, along with an intensity profile for the direction perpendicular to the film edge.

Here one can see that the intensity increases close to the film edge, which is opposite to what was observed the 'energy filtered' image. An increase in intensity near the film edge in 'total yield' mode would indicate that the work function of the substrate is decreasing close to the film. Since adsorption of molecules onto a surface generally decreases a substrate's work function by stabilizing the surface dipole, a change in work function close to the film edge seems like a reasonable explanation for the change in image intensity close to the film edge. It is also possible that the work function of the substrate is reduced due to downward band bending caused by the presence of the PCAT molecule.

If a reduction in work function is in fact the reason why the image in 'total yield' mode appears brighter near the film edge, while the images in 'energy filtered' mode appear darker near the film edge then it would imply that there is a small amount of PCAT extending away from the film. Since the spectra corresponding to the bright region near the film edge does not show any apparent PCAT signal this would imply that any PCAT extending past the film's edge is an extremely thin layer.

To summarize the observations of the change in photoemission intensity near the PCAT film edge, the following conclusions are made. A very small amount of PCAT extends past the edge of the film. This was concluded by the fact that photoemission intensity decreases near the film edge in 'energy filtered' mode, which reflects the lower photoemission yield of PCAT compared to the substrate. Also, the photoemission intensity increased near the film edge in 'total yield' mode, which was an indication that PCAT lowered the work function of the substrate.

Aside from the spatial variation of photoelectron yield, any binding energy shifts close to the film edge were also of interest, since they could indicate localized chemical interactions or long-range charge rearrangement, such as band bending. Localized chemical interactions would show up in the spectra as an additional peak, while band bending would show up as a shifting of peaks.

In order analyze the spectra they were normalized to enhance the features. The resulting series of spectra are shown in figure 5.12, where main features of these spectra have been highlighted. The energy scale was calibrated by setting the Fe3p peak to 55.6eV, which is what it should be for the oxide. The substrate spectrum is similar to what has been observed by previous groups. By using 160eV excitation energy we were

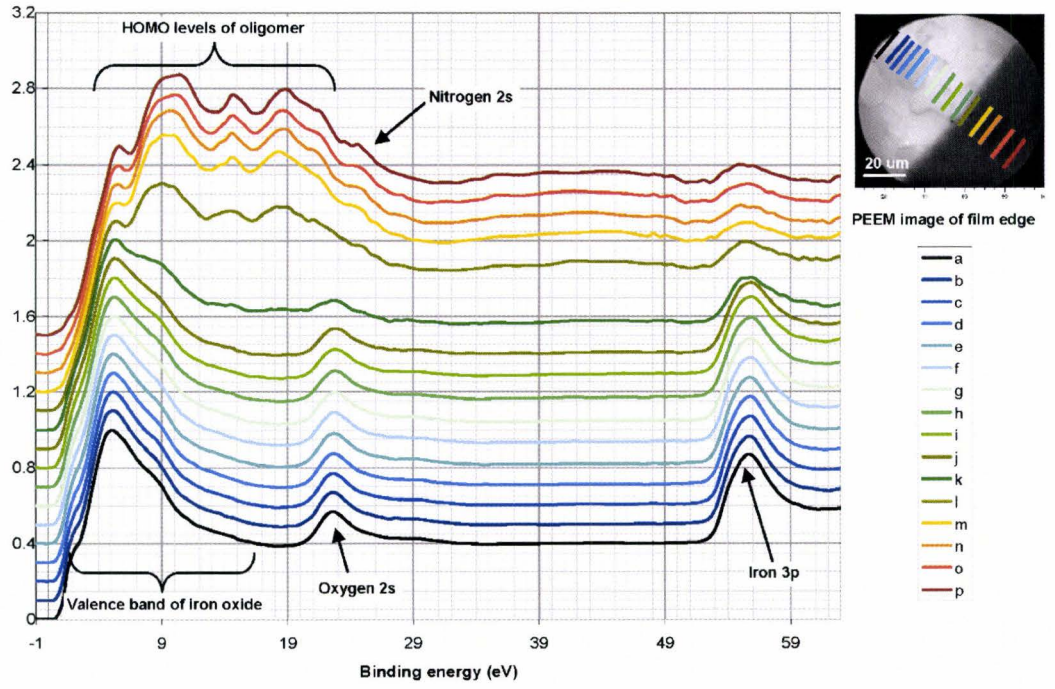

Figure 5.12 *– Normalized photoemission spectra near the edge of a PCAT film (hv = 160eV).*

able to have the full valence bands as well as a few low-binding-energy core levels (such as O2s, N2s and Fe3p) in the same spectrum. There were not obvious shifts in any of the photoemission peaks, however the valence peaks are highly convoluted and the energy resolution of the analyzer was only 0.5eV, so these results do not rule out the possibility of small peak shifts. Due to the low resolution of the spectra, no attempt was made to deconvolute the spectra and assign the peaks.

One feature which was curious was the fact that the large valence peak of the substrate at around 5eV was aligned very well with a shoulder in the PCAT valence band. Whether this is significant or just coincidence is not certain, however the fact that a valence state in PCAT and in iron oxide have the same energy might be important.

In order to investigate the 'remote effect' closer, the sample which exhibited the dendritic PCAT islands was investigated. This sample had been prepared in Hamilton and

was analyzed in Saskatoon, so it had been exposed to ambient atmosphere for quite some time. Using smaller FOV's the dendritic islands could be resolved with the PEEM as shown in figure 5.13.

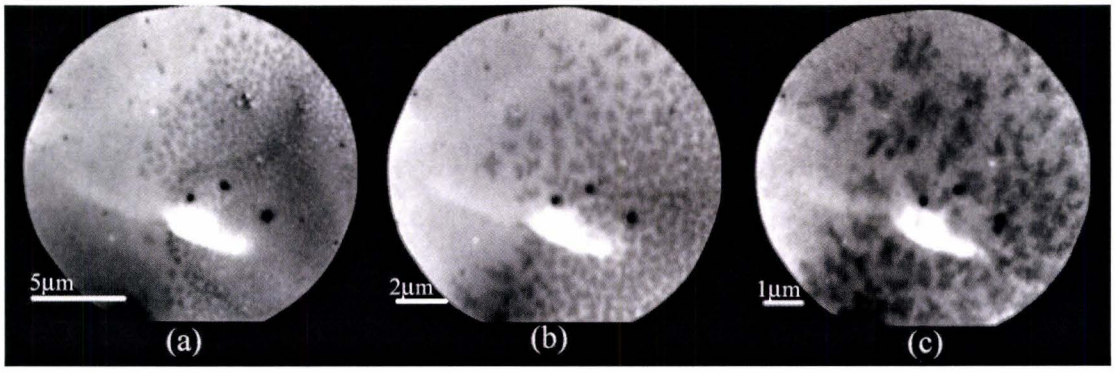

Figure 5.13 *– PEEM images of dendritic islands of PCAT film (a) FOV = 20μm (b) FOV = 10μm (c) FOV = 5μm. All images are taken in 'total yield' mode and using 160eV synchrotron radiation*

Spectra were attempted for these FOV's however we found that the signal intensity for such magnified images was too small to collect spectra. In order to get a good signal-to-noise ratio, one spectrum would take about 12 hours to collect. During the 12 hours, the sample position would drift which eliminates the benefit of spatial resolution since spectra would be smeared across the image

. Alternatively, spectra were obtained at the 100μm FOV for this sample. In these spectra we saw that the PCAT valence features were appearing far past the edge of the film. In fact they only stopped showing up in spectra taken about 800μm away from the film edge. This implies that the PCAT molecules had migrated a large distance away from the film edge. It was already concluded from the AFM images PCAT had spread underneath the mask, and this was believed to be the result of surface migration due to large kinetic energies of physisorbed molecules after deposition however it is unexpected that physisorbed molecules could move as far as 800μm underneath the mask due to

kinetic energy. They would most likely collide and lose most of their kinetic energy long before 800μm was reached.

Since this sample was exposed to atmosphere for several days it is possible that atmospheric components such as oxygen or water assisted PCAT migration across the substrate. The sample prepared in-situ did not show any PCAT signal past the edge of the film. Whether or not atmospheric components assisted in surface migration PCAT, the reason why the PCAT signal was observed so far from the film edge is unknown.

5.4 - Photoemission characterization of in-situ deposition using PEEM

In order obtain electron spectroscopy of the interface and to see how the substrate and overlayer signals might change with increasing overlayer thickness, an in-situ step-by-step deposition was performed, where spectra were collected after each deposition. Although the spatial resolution of the PEEM was not necessary for this study since there was no film edge to look at and it is incapable of obtaining spatially resolved spectra at very high magnifications, the PEEM was still useful for relocating the same area on the sample after each deposition. The sample had to be moved to a different chamber for deposition and moved back for spectroscopy so the same area on the sample is not automatically obtained. We had previously made a coordinate grid on the sample using a Vicker's indenter, so we were easily able to relocate the same spot with the PEEM. By obtaining the same spot for each spectrum we avoid any inhomogeneities on the sample surface which may cause irreproducibility in the spectra.

Before performing the depositions, the sample surface was cleaned of its native oxide and any carbon contamination by argon sputtering. Once the spectra had shown

that all the oxide had been removed the sample was re-exposed to air in order to re-grow a new oxide. By doing this we ensure the oxide layers on all of our in-situ-prepared samples have a controlled starting point.

The photoemission spectra before argon sputtering, after sputtering, and after re-oxidation are shown in figure 5.14.

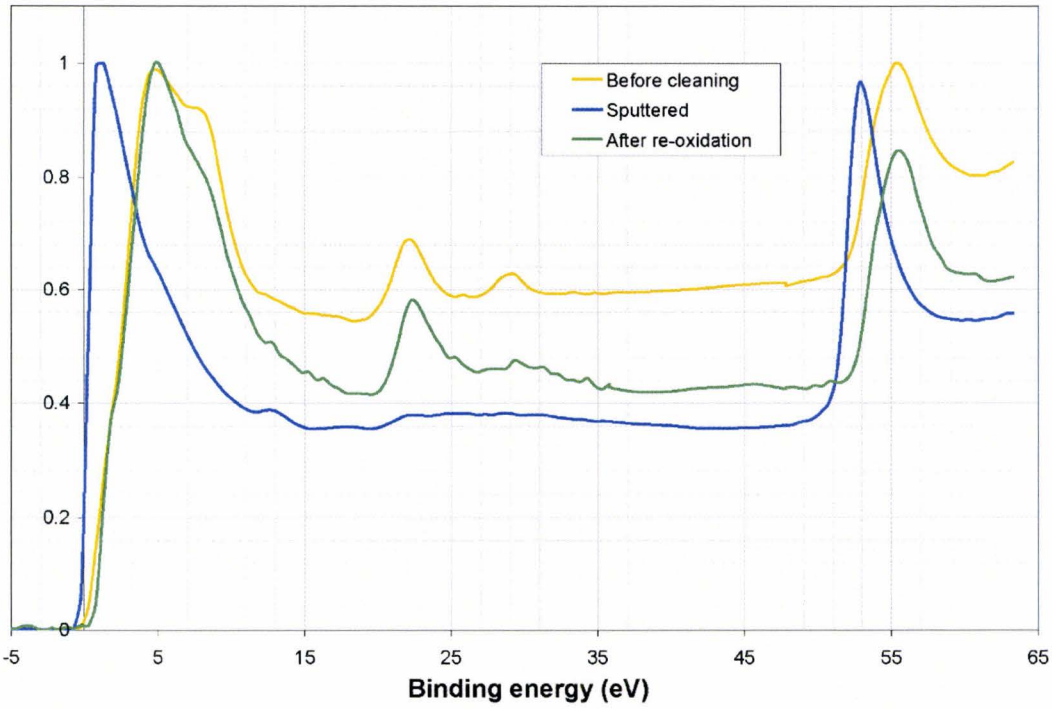

Figure 5.14 *– Photoemission spectra (hv = 160eV) of iron substrate before and after sputter cleaning and after re-oxidation.*

These spectra were used for energy calibration, by setting metallic iron valence band maximum to the Fermi level (0eV). This adjustment put the Fe3p peak for metallic iron was at 52.8eV as had been reported previously.[94] In these spectra we can see that the Fe3p peaks for the oxidized samples are at 55.6eV, which is 2.8eV higher binding energy than metallic iron. Also the valence band maxima for the oxidized samples are about 1.3eV below the Fermi level. For the oxidized samples there is an O2s peak at around

22.3eV and this peak disappears after sputtering. There was also a peak at 22.8eV and a shoulder in the valence band at 7.8eV in the spectrum of the sample before cleaning, which were attributed to carbon contamination, since they disappeared after sputter cleaning and did not return after re-oxidation.

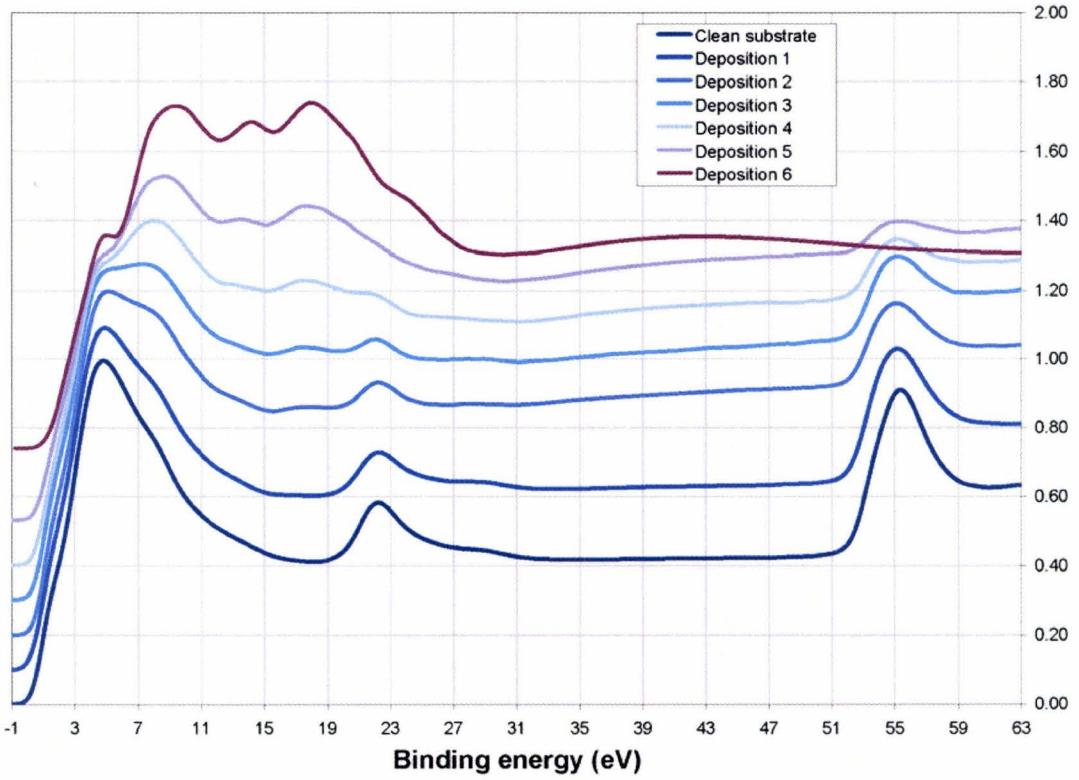

Figure 5.15 *– Photoemission spectrum (hv = 160eV) of in-situ PCAT deposition series.*

PCAT was then deposited in about 1Å increments for five deposition steps. Then a thick PCAT film of about 150Å was deposited to obtain the bulk PCAT spectrum. The deposition series is shown in figure 5.15. From these spectra one can see that the Fe3p (at ~55eV) and O2s (at ~22.5eV) signals attenuate as the overlayer thickens, and for the bulk PCAT spectrum (deposition 6) the Fe3p and O2s signals are completely buried.

As the overlayer grows the PCAT peaks become superimposed over the substrate peaks. There does not appear to be any shifting of peaks during the deposition, however it is difficult to conclude this for certain based on these spectra because of the poor energy resolution ($\Delta E = 0.5eV$) and the fact that the valence peaks are highly convoluted.

If the spectra for thin overlayer thicknesses (i.e. spectra 1 to 5 in figure 5.15) are merely the superposition of substrate and overlayer spectra then this would imply that there is no observable change in valence levels at the interface. If this is the case then it should be possible to simulate any of the spectra using a linear combination of the substrate and bulk overlayer spectra (i.e. using the substrate and spectrum 6). If the spectra cannot be reproduced then it implies that there is something different happening at the interface.

Figure 5.16 shows the original and reconstructed spectra for depositions three and four. As can be seen from the figure, the spectra cannot be reconstructed exactly using the reference spectra. The largest discrepancies between the re-constructed and the original spectra are: (1) The intensity of the background signal between 30 and 50eV is more intense in the original spectra. (2) The shoulder of the PCAT valence band at 5.5eV is less distinct in the real spectra than it is predicted to be by the re-constructed spectra.

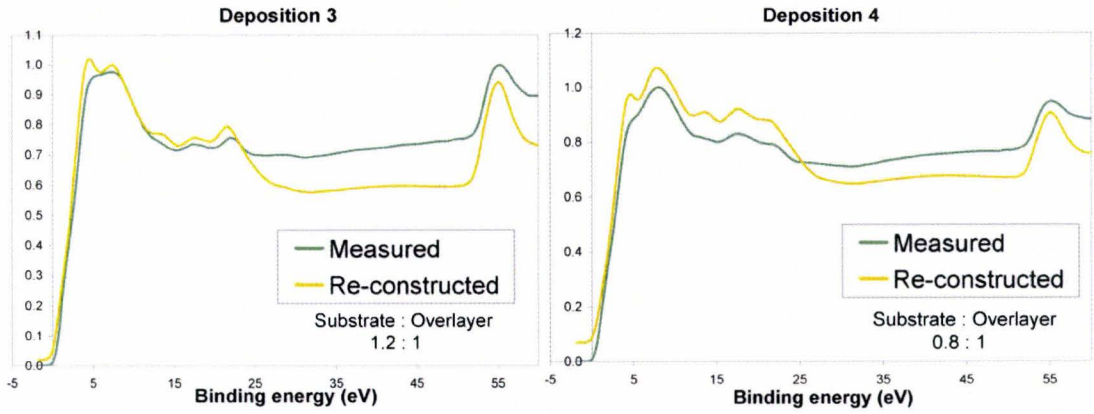

Figure 5.16 *– Original spectra and spectra reconstructed from the substrate and bulk PCAT spectra for depositions 3 and 4.*

With regards to the first discrepancy, it is known that modeling of inelastic background intensity is a complex matter and very difficult to do especially in layered materials,[95,96] so it is expected that the background intensity will not be merely a linear combination of background intensity from reference spectra. Since these spectra are normalized, it is the relative intensity of the background compared to the resonant photoemission peaks which are of interest. Since resonant photoelectron signals attenuate with depth faster than inelastic photoelectron signals do, the large inelastic signal from the substrate would require a thicker film to bury it than would the resonant photoelectrons. As a result the relative intensity of the inelastic background to the resonant peaks appears larger than would be predicted by a simple linear combination of reference spectra.

The second discrepancy between the spectra seems to imply a change in the relative intensities of certain resonant photoemission peaks near the interface, or possibly a shift in one of the peaks. The shoulder at 5.5eV in the PCAT bulk spectrum is rather distinct. For the spectra of deposition three and four the shoulder is not as distinct, whereas it would be according to the linear combination of reference spectra. This could

imply that the resonant photoemission process giving rise to that peak is less intense and more broad close to the interface, or possibly that it has shifted to slightly higher binding energy.

Due to the poor resolution of these spectra and the high convolution of the valence region, conclusions from this observation can only remain as speculations, however if this is a real effect then one could imagine that it might be caused by polarization of the PCAT molecules close to the interface. Since this photoemission feature is coincidentally at the same energy as a peak in the substrate it is possible that the orbitals or states responsible for these peaks interact strongly. It is after all, according to molecular orbital theory, required that orbitals have similar energies in order for strong interactions to occur. It is possible then that the oxide surface polarizes the PCAT molecule at the interface by re-arranging some of the PCAT valence electrons, such that the corresponding photoemission peaks for PCAT molecules at the interface broaden or shift in energy.

5.5 – XPS/UPS characterization of deposition using laboratory photon sources

The spectra obtained at the synchrotron using PEEM gave some interesting results; however higher resolution valence spectra as well as core-level spectra were required in order to detect possible changes in valence features or core level shifts at the interface. Therefore an in-situ deposition was characterized using a laboratory XPS/UPS system. The spectrometer on this system had a much higher energy resolution than the energy analyzer on the PEEM, but it lacked spatial resolution. The spot size of the excitation source on the sample was $400\mu m^2$, so the spectra represent the average signal over whole $400\mu m^2$ area. The benefit of this instrumental set-up was that XPS and UPS characterization of the sample was possible in the same instrument. We were therefore able to monitor the Fe2p, O1s, C1s, N1s and Fe3p XPS peaks, as well as the valence bands and secondary electron cut-off position of the sample for each step of the deposition. Furthermore, the spectrometer was capable of a 0.05eV energy resolution, which is useful for examining the valence features.

After sputter cleaning and re-oxidation of the sample the full set of spectra were obtained for the substrate. The core photoemission spectra for the main elements in the substrate are shown in figure 5.17. Peaks were fit to the spectrum in order for peak assignments to be made. A Shirley-type inelastic background was used. A Tougaard-type background would have been more accurate for peak integration,[97] however the Shirley background was used for simplicity, and is adequate for qualitative peak assignments.

The Fe2p spectrum (figure 5.17, a) exhibits two sets of peaks, $2p_{1/2}$ and $2p_{3/2}$ separated by 13eV. The fact that there are two sets of peaks is a result of exchange

splitting, caused by coupling of the core photo-hole with the overall spin of the valence electrons.[98,99]

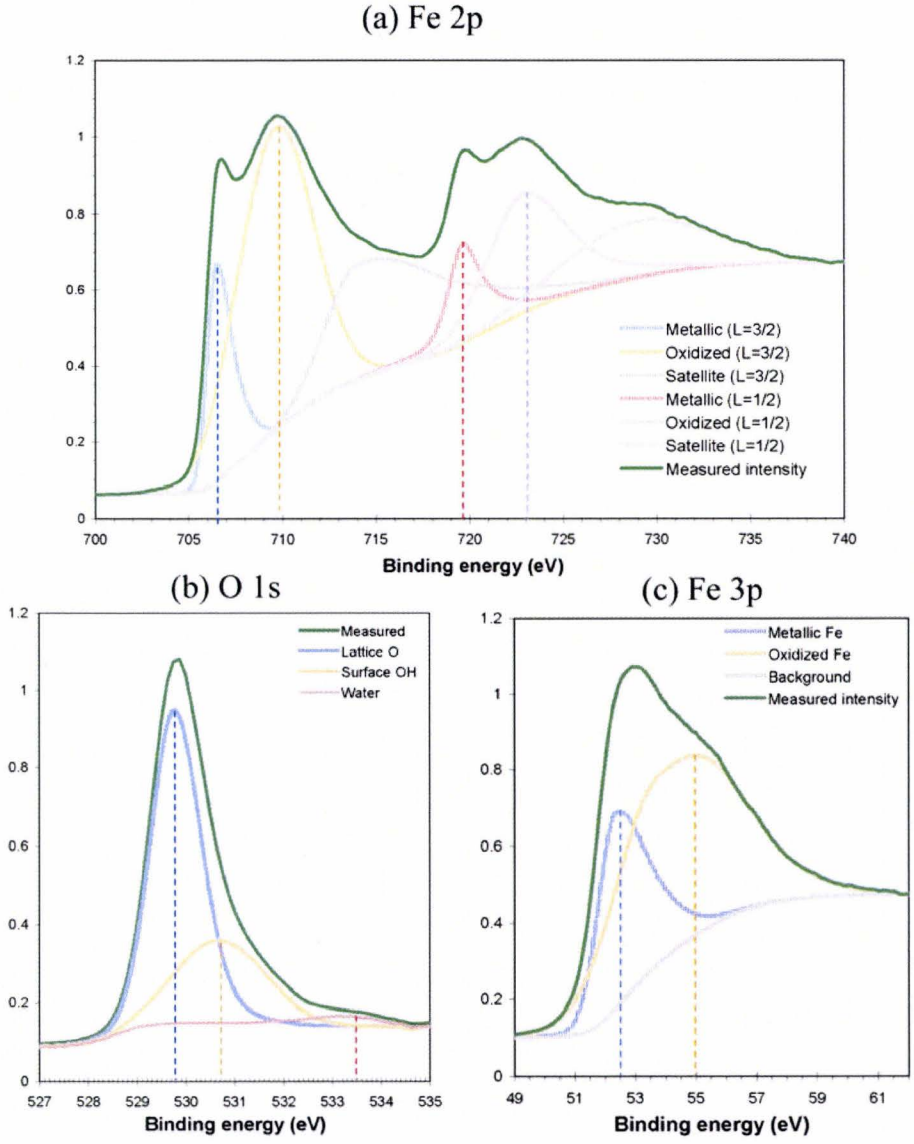

Figure 5.17 *– XPS spectra of iron substrate prior to deposition. Included are peak fits, using a Shirley-type background.*

There is a peak at around 709.6eV which results from the oxidized form of Fe in the oxide. This peak is actually a convolution of two peaks, one for Fe^{2+} and one for Fe^{3+}.

There is also a peak at 706.6eV, which is cause by photoemission from metallic Fe. The fact that metallic iron is still observable in the spectrum implies that the oxide film is extremely thin, probably around 2nm thick.

In the Fe3p spectrum, a metallic iron peak is also present (52.3eV); however it is not as pronounced as in the Fe2p spectrum. The oxidized iron shows up in the Fe3p spectrum as an asymmetric peak at around 54.9eV; however this peak is actually believed to be a convolution of several peaks,[57,94,100] which result from the many possible final states of Fe3p photo-ionization.[100] Depending on whether one models the spectrum using highly asymmetric peaks or using several convoluted peaks the chemical shifts will differ. Therefore determining the type of oxide based on the Fe3p peak is unreliable. These peak assignments would be consistent with any of the possible oxides (FeO, Fe_3O_4, α-Fe_2O_3 or γ-Fe_2O_3).

The O1s spectrum was composed of one large peak at 529.8eV, with a broad shoulder at 530.6eV and a broad peak of very weak intensity at 533.4eV. According to previously reported O1s spectra of iron oxides,[101] the peak at 529.8eV was attributed to lattice oxygen species, while the peak at 530.6eV was chemisorbed OH species, and the peak at 533.4eV was attributed to water.

Previously reported photoemission spectra of various iron oxides can be used to estimate the composition of the oxide. A summary of peak shifts for various iron oxides is given in table 5.1.[94,101]

Table 5.1 – XPS shifts for several iron oxides[94,101]

	Binding energies (eV)		
	Fe $2p_{3/2}$	**Fe 3p**	**O 1s**
Fe (metallic)	706.9	53.0	N/A
FeO	709.5	54.9	530.0
Fe_3O_4	708.3	53.9	530.2
α-Fe_2O_3	711.0	55.7	529.8
γ-Fe_2O_3	711.9	55.7	530.0

According to these shifts, the oxide on our sample was composed of mainly FeO, while the oxide formed on the samples in the PEEM study was mainly Fe_2O_3. The reason why the two samples had different oxides is probably due to the fact that the current sample was oxidized under a flow of nitrogen in order to reduce the carbon contamination from atmosphere-borne carbon, however the PEEM sample was oxidized in an un-controlled atmosphere. This fact would also explain why the oxide is so thin on the current sample according to the Fe2p XPS spectrum, since under a flow of nitrogen the oxygen partial pressure would have been less.

The C1s and N1s core level photoemission spectra for the thick PCAT overlayer are shown in figure 5.18. The C1s spectrum had two peaks; one sharp peak at 284.1eV and one broad peak at 285.2eV. The peak at 285.2eV was assigned to the carbon atoms directly bonded to the nitrogen atoms, while the peak at 284.1eV was attributed to the carbon atoms not directly bonded to the nitrogen atoms. These chemical shifts are consistent with those previously observed in core level spectra of polyanilines.[102,103] The N 1s spectrum of the thick PCAT film showed only one peak, positioned at 399.2eV,

which corresponds to polyaniline nitrogen in its amine form, according to previously reported XPS spectra.[102-104]

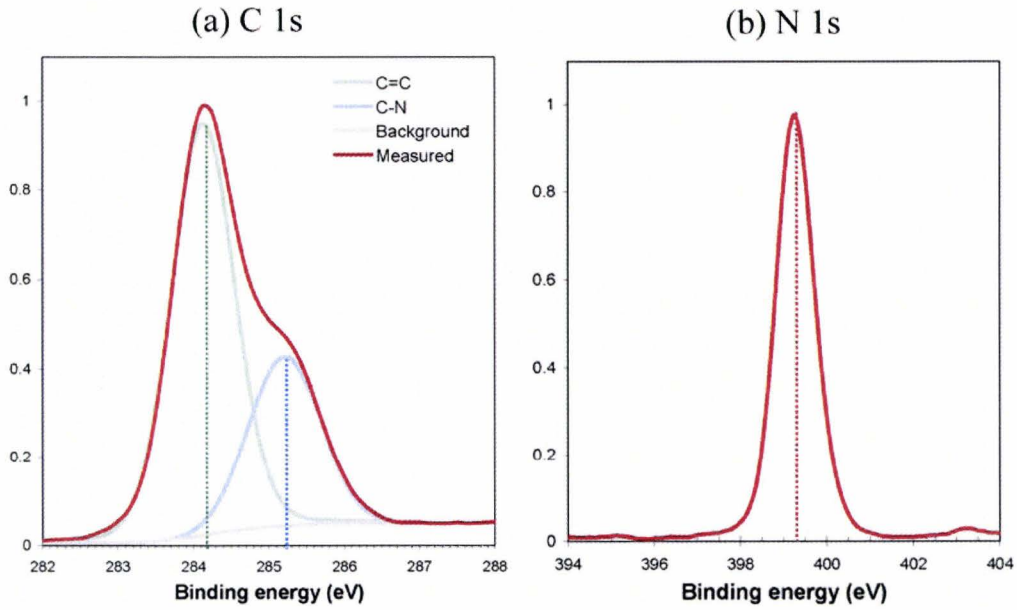

Figure 5.18 *– Core level photoemission spectra for a thick PCAT film.*

Since XPS is a quantitative technique,[57] the areas under the carbon and nitrogen peaks can be integrated to find the carbon-to-nitrogen ratio to see if it corresponds to that expected for PCAT. The molecular formula of PCAT is $C_{30}H_{22}N_4$, which gives a C:N ratio of 7.5:1. The ratio of carbon-to-nitrogen peak areas was 4.18:1. The carbon-to-nitrogen sensitivity factor is 0.571, [ref. 105] which gives a C:N mole ratio of 7.35:1. This is reasonably good agreement with what is expected, and the discrepancy is likely due to nitrogen contamination present on the substrate (as will be discussed with figure 5.20).

The full set of core photoemission spectra for the deposition series is shown in figures 5.19 and 5.20.

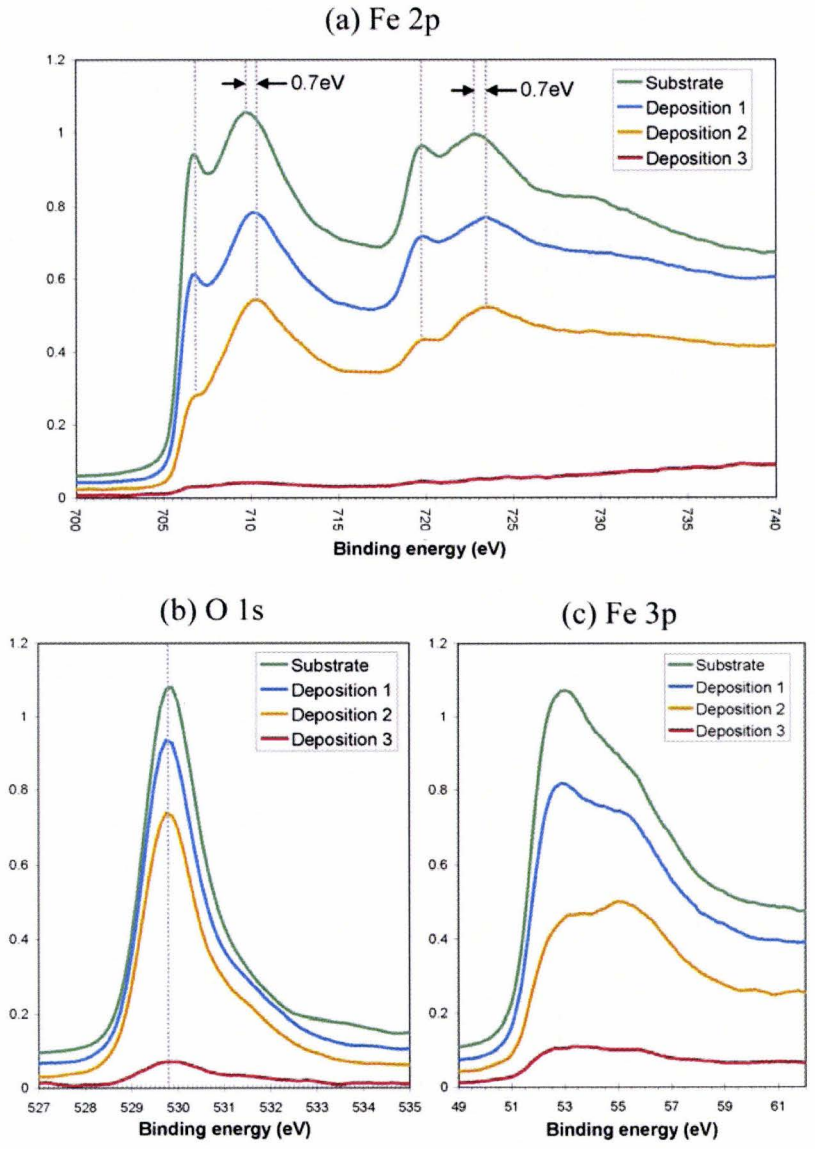

Figure 5.19 *– Fe 2p, O 1s and Fe 3p XPS spectra for in-situ deposition series of PCAT on iron.*

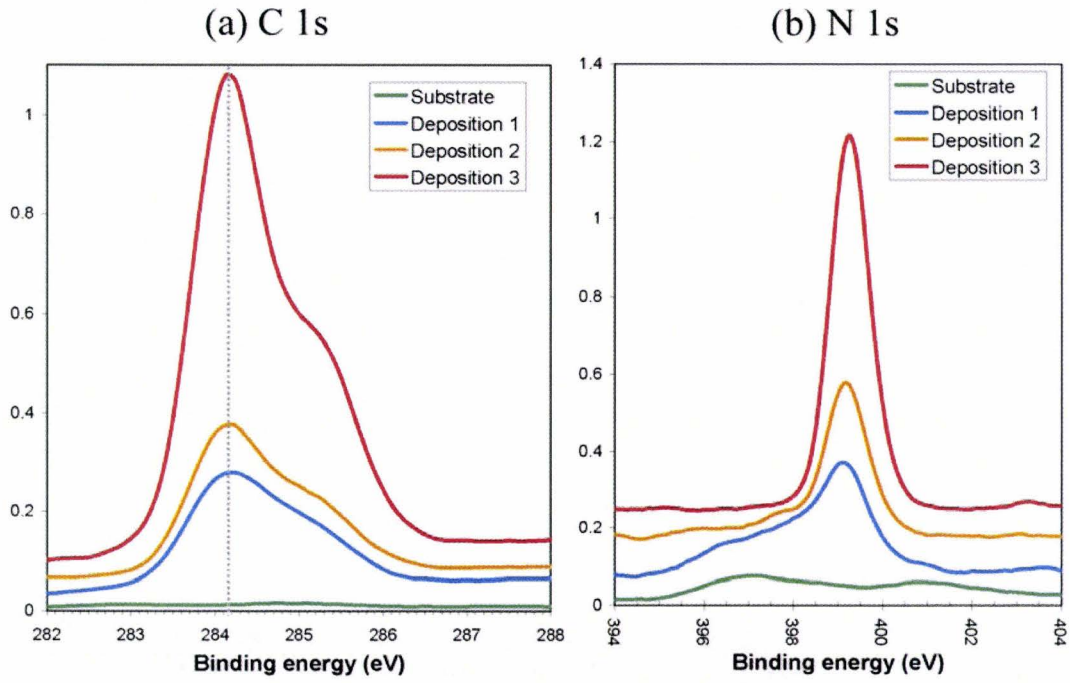

Figure 5.20 *– C 1s and N 1s XPS spectra for in-situ deposition series of PCAT on iron*

The spectra in figure 5.19 are the core photoemission spectra for elements present in the substrate. It can be seen that the oxygen and iron signals become attenuated during the deposition, although a small amount of substrate signal is still visible in the spectra after the third deposition, which implies that the total PCAT film thickness in the end was only about 5nm thick. As discussed above, the Fe2p spectrum consists of both metallic and oxidized iron peaks. The metallic signal attenuates faster than the oxidized signal does, which implies that the metallic iron is underneath the oxide, as expected.

After the first layer of PCAT is deposited, there is a peculiar change in the Fe2p spectrum. The oxidized iron peaks shift by about 0.5eV to higher binding energy, while the metallic iron peaks exhibit no shift. This observation is believed to be an indication of the interaction between the PCAT molecules and the oxide, and will be discussed in more detail after the UPS data has been shown.

In the O1s spectrum, the lattice oxygen peak attenuates before the surface OH peak does, which is consistent with the assignments of these peaks, and that the OH signal is more superficial than the lattice O signal. There is no observed shift in the oxygen peaks during the deposition, which implies that the shift observed in the Fe2p spectra is unique to oxidized Fe.

The Fe3p spectra also show a more rapid attenuation of the metallic peak than the oxidized peak, which is consistent with the fact that the oxide is more superficial than the metal. Since the Fe2p spectra showed a shift in the oxidized peak, it is expected that there would also be a peak shift in the Fe3p spectra; however these spectra are highly convoluted, so a peak shift is not obvious. With some curve fitting, a peak shift of 0.5eV can be seen, however conclusions from such a peak-fitting routine are not necessarily reliable.

Figure 5.20 shows how the overlayer signals change during deposition. From figure 5.20 (a) one can see that the substrate was clear of carbon contamination before deposition, but from figure 5.20 (b) one can see some sort of nitrogen species present on the substrate, as evidenced by the two low-intensity peaks at 397.0 and 401.0eV. These nitrogen species are of unknown origin, and only showed-up in the spectra after sputtering of the substrate.

As the PCAT film is deposited the main carbon and nitrogen peaks grow in intensity, without any observable binding energy shifts. In the N1s spectra for the first and second deposition there are some extra bumps in the spectra; however these cannot be discerned from the background substrate contamination with any certainty.

In summary of the XPS data from the in-situ deposition, a peak shift was observed for the oxidized iron peaks in the Fe2p spectra by about 0.5eV to higher binding energy; however there was no observed shift for the metallic iron or the oxygen peaks. This indicates that only the oxidized iron is affected by the presence of PCAT. There are no observed shifts in the PCAT core spectra.

These spectra indicate that the interaction between PCAT and iron oxide is not a localized interaction (i.e. not a localized chemical bond) since a localized interaction would be evident by the appearance of a new peak in the spectra after the first deposition, which would become attenuated after further depositions (see figure 3.13). No additional peaks were observed in any of the spectra; however the possibility of an additional peak in the N1s spectra cannot be completely ruled out because of the convolution with substrate contamination.

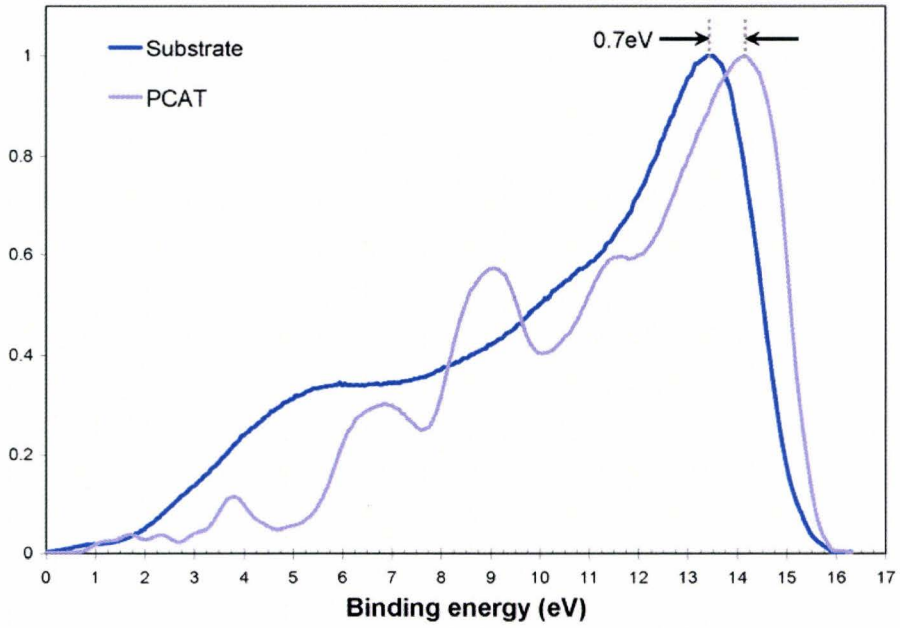

Figure 5.21 *– UPS spectra of clean substrate and thick PCAT film*

In order to monitor the valence states and the work function of the sample throughout the deposition, UPS spectra were obtained. The spectra for the substrate and the thick PCAT overlayer are shown in figure 5.21.

The valence peaks in the substrate are broad, reflecting its band-like electronic structure, while the PCAT valence peaks are sharp, reflecting it discrete valence orbitals. The valence band of the substrate appears to reach the Fermi level, which is not expected for the oxide, however the oxide is very thin and photoemission from the metallic iron had been observed in the core spectra, so the part of the valence band reaching the Fermi level is probably from the underlying metal. Due to spectrometer peak broadening it is difficult to say exactly where the HOMO and valence-band maximum (VBM) are however they can be estimated. The HOMO level of PCAT is approximately 1.1eV below the Fermi level, while the VBM of the substrate is approximately 0.2eV lower in binding energy. These values show that there is a reasonably good alignment between the HOMO of PCAT and the VBM of the substrate. This close alignment may coincidental or it may be due to Fermi level alignment between PCAT and Fe_2O_3 at the interface. If it is alignment at the interface then this would imply our PCAT film thickness was not large enough to reach the bulk value, and therefore bulk PCAT would have a different value for its HOMO level. It is certainly possibly (even likely) that the PCAT film did not have its bulk properties (i.e. properties unaffected by the interface), since it is known that semiconductors with very low charge carrier densities can have space-chare regions that can extend dozens of nanometers into the bulk.[56] Therefore, in order to be safely into the bulk properties of PCAT film, the experiment could be repeated with a very thick (upwards of 100nm) PCAT overlayer being formed.

From the secondary cut-off positions one can see that the substrate and overlayer have different work functions (see figure 5.21, the high-binding-energy region of the spectrum). The overlayer has a work function that is smaller than the substrate by about 0.7eV. The change in work function can be achieved by band bending or by adsorbate dipoles as depicted in figure 5.22. If the work function change is the result of band bending then all the photoemission features will shift in conjunction with the shift in work function, as depicted in figure 5.22 (a).

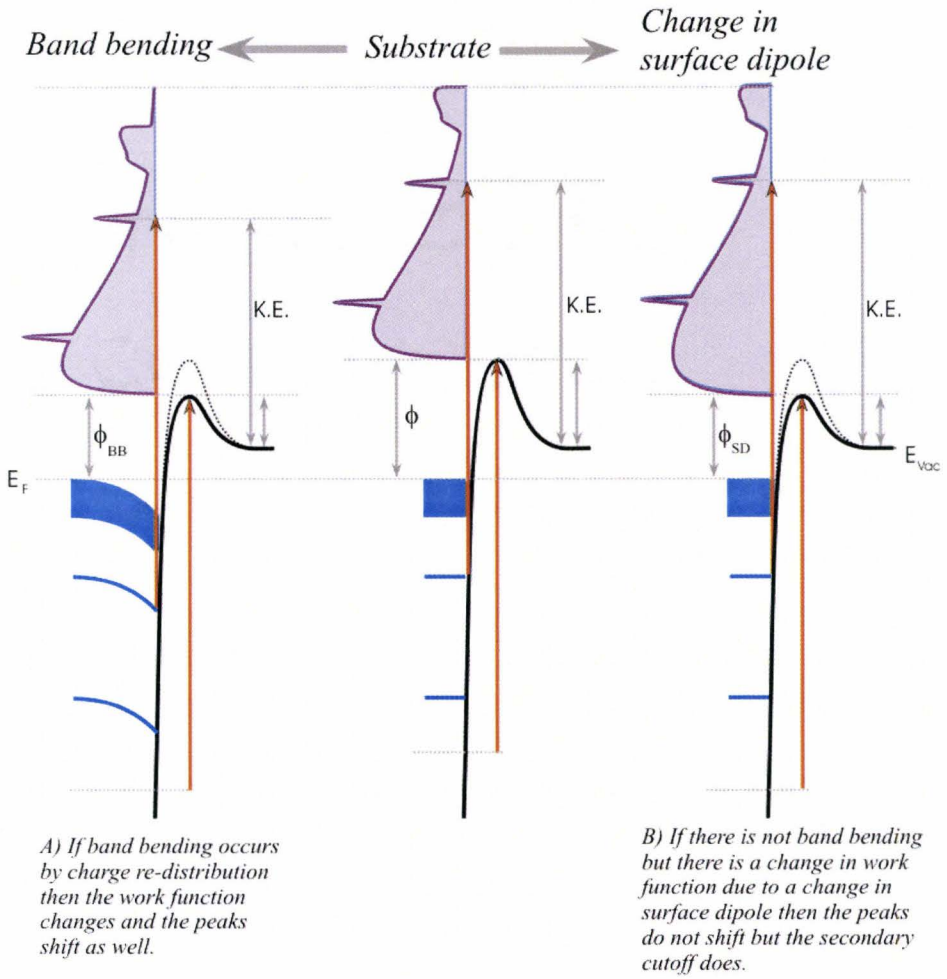

Figure 5.22 *– Schematic of how band bending (a) and adsorbate dipole formation (b) will affect photoemission spectra.*

If the work function change is the result of a reduction of the surface energy barrier of the substrate, due to stabilization from adsorbate dipoles (as depicted in figure 5.22, b) then there will be no shift in the other photoemission features, and only a shift in the work function.

Figure 5.23 shows the valence spectrum during the deposition sequence. One can see that the PCAT valence features do not shift during the deposition, while the work function changes after the first deposition. One cannot tell for sure whether the substrate valence features are shifting because they are not very distinct peaks.

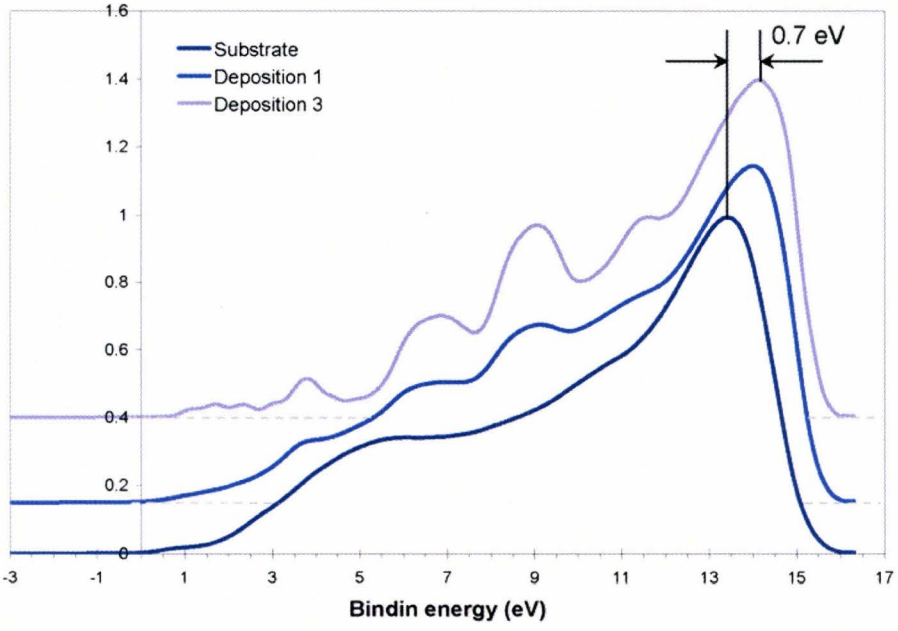

Figure 5.23 *– UPS spectra using He-lamp for in-situ deposition of PCAT on an iron substrate.*

While it is difficult to observe peak shifting with valence features due to the high convolution, XPS spectra can clearly show peak shifting. As was seen in figures 5.19 and 5.20, the only peaks that exhibited shifting during the deposition was the oxidized iron peaks. The oxygen, metallic iron, carbon and nitrogen peaks exhibited no shifting. This

observation indicates band bending in the oxide, but no band bending in the overlayer, although as mentioned earlier, it is possible that the PCAT film did not reach its bulk state and so no band bending would be observed in PCAT unless the spectra could be compared to the bulk value. Regardless of whether there is any band bending in the PCAT layer there is band bending in the oxide of about 0.5eV, while the work function changes by 0.7eV, which indicates an interface dipole of about 0.2eV.

One thing that is peculiar is that there is a shift in the oxidized iron peaks, but no shift in the oxygen peaks, and presuming there is band bending in the oxide one would assume the oxygen and iron peaks should both shift. If the shifting is in fact due to band bending then the reason it is not observed in the oxygen peaks may be related to the fact that the oxide is a Mott-Hubbard (or charge-transfer) insulator, and that the oxide does not necessarily exhibit bands in the classical sense. Therefore perhaps the iron states and the oxygen states are acting independently.

Another possibility is that the 'band bending' is just a bulk redistribution of iron ions. Band bending in semiconductors is achieved by bulk re-distribution of electrons or holes, so a bulk re-arrangement of iron ions might cause similar observations in the photoemission spectra. This hypothetical ion re-arrangement would cause a space-charge in the oxide. One would still assume however that any potential gradient in the oxide layer would show up in the oxygen spectra as well, unless the oxygen electrons for some reason were not very sensitive to the electric field.

In summary, UPS spectra showed a change in work function upon the first deposition of PCAT and alignment of the PCAT HOMO within 0.2eV of the substrate VBM. Results form XPS spectra of the deposition series showed that there is a peak shift

in the oxidized iron peaks of the Fe2p spectra, but no shift in the metallic iron peak or oxygen 1s peak. There was also not peak shifts observed for the carbon or nitrogen peaks. These collective results were interpreted as a band-bending-like behavior in the oxide film (possibly from iron ion re-arrangement) caused by the adsorption of PCAT. Whether or not these observations are related to the corrosion inhibiting power of PCAT is however inconclusive. Many of the fundamental questions of this system are still unanswered in the literature. For example there is no general consensus as to what makes a passive oxide passive[106], the exact structure of the passive films[106] and the theoretical description of the oxide electronic properties[32-34] are incomplete, and there is still dispute over whether PANI's actually causes by the formation of the passive oxide or whether there is some other cause to the passive oxide underneath PANI films.[107] Answers to these questions seem fundamental to understanding what happens at the PCAT-iron oxide interface and how this might cause the formation of a passive oxide. In spite of this, the PCAT-oxide system is interesting in its own right due to the technological importance of oxide films and molecular organic semiconductors. This current study made some steps in the direction of understanding such systems.

5.6 - Future directions

We have obtained evidence of some unique interactions between the PCAT molecule and the iron oxide surface, however in order to draw conclusions as to the exact nature of these interactions it is necessary to perform more controlled studies. To begin with, the studies should be carried out on an iron single crystal rather than a polycrystalline substrate. The polycrystallinity of sample causes problems for the work function of the sample, since it will not remain constant from sample to sample. It also

causes problems for control over the oxide structure. Different grains will have different oxide thicknesses and possibly different oxide crystal orientations and oxide compositions.

The mention of oxide structure brings about another improvement that needs to be made to the experiments, which is that there must be a reproducible method of forming the oxide, and the precise structure that this method yields should be well understood. For example, a polished single crystal iron substrate should be sputter cleaned and annealed in vacuum, followed by oxygen dosing at a defined pressure and a defined period of time, at room temperature. These parameters should be optimized to yield a layered oxide of approximately 5nm thick, and composed of an inner layer of Fe_3O_4 and Fe_2O_3. This condition should be set as the starting point for all depositions. If this starting point could be achieved then one could try different parameters, such as varying the oxide thickness for the deposition series, or dosing the substrate with a monolayer of water before deposition.

The next thing to consider for future experiments would be to repeat the experiments using the other oxidation forms of PCAT. One could also deposit the oxidized form of PCAT as a thin layer, then expose the sample to clean air and re-examine afterwards. In addition to the other oxidation forms, one should also perform the step-by-step depositions in smaller steps. In order to achieve smaller steps, one needs to use a slow deposition rate, which requires a very clean vacuum system, and also precise control over the evaporation temperature.

In addition to the improvements to the experiments already performed there are several other characterization methods that could be used. The structures and

compositions of the native oxide and the oxide underneath a PCAT film could be compared using high-resolution TEM with electron energy loss spectroscopy (EELS). With these methods combined the crystal structure of the oxide can be seem, as well as a profile of Fe^{3+} and Fe^{2+} composition through the oxide layer. The most difficult part of performing such experiments would be sample preparation, as TEM requires 100nm-thin slabs of sample in order for the sample to be transparent for the high-energy electrons used to probe the sample.

Another technique which could be used to compare the oxide structures of the air-formed oxide and the oxide underneath the PCAT film would be neutron reflectometry. This technique is similar to interferometry for film thickness measurements, except it uses low energy neutrons, which makes it capable of resolving sub-Ångstrom scale features. It only gives details of the structure of the oxide in the direction perpendicular to the surface, which is what is of most interest anyways. The main problem with using this technique again lies in the sample requirements. Neutron reflectometry requires extremely flat samples, and due to the low signal intensity it also requires quite large samples. Samples would need to be a few centimeters in diameter with a surface roughness of no more and 2nm. This kind of sample would be essentially impossible for a single crystal and would have to be prepared by evaporation of iron onto a flat substrate such as a sapphire wafer; however this sample would again be polycrystalline.

Another technique which could be used and would have less stringent sample requirements would be X-ray reflectometry and glancing-angle X-ray diffraction. These techniques would again give structural details of the oxide however X-ray diffraction would require the use of a synchrotron radiation source.

The exploration of this system could also be expanded to include scanning probe techniques. One could measure the change in surface potential when moving along the substrate away from the film by using scanning Kelvin-probe microscopy (SKPM).

With all the possible techniques to use and all the questions needed to be answered, even about the most basic questions such as 'what is the structure of the oxide' this project could be carried on for many years. The eventual goal would be to understand why PANI inhibits corrosion and how can molecules be designed such that corrosion inhibition is improved, or processing properties are more favorable, or the molecule is cheaper to synthesize. Given the complexity of the system and the special techniques required to study a system on a small scale, this end goal would likely be many years in the future.

6 - Conclusion

This study investigated the effects of PCAT films on oxide-covered iron substrates. PEEM experiments were aimed at understanding the 'remote effect' of PANI corrosion inhibition. These studies showed no spectroscopic features to indicate a remote effect, but did give evidence to support the theory that PCAT is capable of migrating across the iron surface, which may be the cause of the 'remote effect'. High-resolution XPS and UPS studies were performed for a step-by-step deposition of PCAT on oxide-covered iron. There experiments showed that the presence of PCAT reduces the work function of the substrate by 0.7eV. This change in work function was attributed to bulk charge redistribution in the oxide film and polarization of PCAT molecules at the interface. The results from these experiments lend insight into the interaction between PANI and native iron surfaces towards and understanding of how PANI may cause

corrosion inhibition. The results of these experiments may be valuable to a broad audience of surface scientists and modern device research because the techniques and theoretic principles used in this study were borrowed from solid-state device science, and the system under study involves thin oxide films and interfaces with molecular organic semiconductors, which are of modern technological interest.

References

1) D. W. DeBerry, *J. Electrochem. Soc.* (1985) **132**:1022-1026

2) G. M. Spinks, A. J. Dominis, G. G. Wallace, D. E. Tallman, *J. Solid State Electrochem.* (2002) **6**:85-100.

3) T. P. McAndrew, *Trends in Polym. Science.* (1997) **5**:7-12.

4) T. Van Schaftinghen, S. Joiret, C. Deslouis, H. Terryn, *J. Phys. Chem. C* (2007) **111**:14400-14409.

5) W.-K. Lu, R. L. Elsenbaumer, B. Wessling, *Synth. Met.* (1995) **71**:2163-2166.

6) T. Schauer, H. W. Greisiger, C. D. Eisenbach, *Polym. Preprints* (2000) **41**:1783.

7) B. C. Berry, A. U. Shaikh, T. Viswanathan, *Polym. Preprints* (2000) **41**:1739-1740.

8) P. J. Kinlen, V. Menon, Y. Ding, *J. Electrochem. Soc.* (1999) **146**:3690-3695.

9) S. Sathiyanarayanan, S. S. Azim, G. Venkatachari, *Elecrochim. Acta.* (2007) **52**:2068-2074.

10) L. L. Sheir, R. A. Jarman, G. T. Burstein, "Corrosion – Volume 2 Butterworth-Heinemann, (2000)

11) B. Wessling, *Adv. Mater.* (1994) **6**:226-228.

12) P. Zarras, N. Anderson, C. Webber, D. J. Irvin, J. A. Irvin, A. Guenthner, J. D. Stenger-Smith, *Rad. Phys. and Chem.* (2003) **68**:387-394.

13) A. Cook, A. Gabriel, D. Siew, N. Laycock, *Curr. Appl. Phys.* (2004) **4**:133-136.

14) A. Gabriel, N. Laycock, H. McMurray, G. Williams, A. Cook, *Electrochem. Solid-State Lett.* (2006) **9**:B57-B60.

15) R. M. Cornell, U. Schwertmann, The Iron Oxides – Structure, Properties, Occurrences and Uses second edition, Wiley, Weinheim, Germany (2003).

16) N. Perez, Electrochemistry and Corrosion Science Kluwer Academic Publishers, New York, (2004).

17) B. L. Maschhoff, N. R. Armstrong, *Langmuir* (1991) 7:693-703.

18) A. P. Grosvenor, B. A. Kobe, N. S. McIntyre, *Surf. Sci.* (2004) **572**:217-227.

19) A. P. Grosvenor, B. A. Kobe, N. S. McIntyre, S. Tougaard, W. N. Lennard, *Surf. Interface Anal.* (2004) **36**:632-639.

20) J. Weissenrieder, M. Göthelid, M. Månsson, H. von Schenk, O. Tjernberg, U. O. Karlsson, *Surf. Sci.* (2003) **527**:163-172.

21) G. W. R. Leibbrandt, G. Hoogers, F. H. Habracken, *Phys. Rev. Lett.* (1992) **68**:1947-1950.

22) A. Davenport, L. J. Oblonsky, M. P. Ryan, M. F. Toney, *J. Electrochem. Soc.* (2000) **147**:2162-2173.

23) E. E. Rees, M. P. Ryan, D. S. McPhail, *Electrochem. Solid-State Lett.* (2002) **5**:B21-B23.

24) H. Deng, P. Qian, N. Sanada, M. Yoneya, H. Nanjo, *J. Electrochem. Soc.* (2003) **150**:B336-B341.

25) A. J. Davenport, L. J. Oblonsky, M. P. Ryan, C. M. Vitus, *Phys. Rev. Lett.* (1997) **79**:4282-4285.

26) B. Wessling, *ACS Symposium Series*, (2003) **843**:35-73.

27) H. Lüth, "Solid Surfaces, Interfaces and Thin Films" fourth edition, Springer, Berlin (2001).

28) D. Cahen, A. Kahn, *Adv. Mater.* (2003) **15**:271-277.

29) N. Koch, *Chem. Phys. Chem.* (2007) **8**:1438-1455.

30) X.-Y. Zhu, *Surf. Sci. Rep.* (2004) **56**:1-83.

31) H. Ishii, K. Sugiyama, E. Ito, K. Seki, *Adv. Mater.* (1999) **11**:605-625.

32) L. M. Sandratskii, M. Uhl, J. Kübler, *J. Phys.: Condens. Matter* (1996) **8**:983-989.

33) A. Bandyopadhyay, J. Velev, W. H. Butler, S. K. Sarker, *Phys. Rev. B* (2004) **69**:174429

34) S. Hüfner, *Advances in Physics* (1994) **43**:183-356.

35) A. Fujimori, M. Saeki, N. Kimizuka, M. Taniguchi, S. Suga, *Phys. Rev. B* (1986) **34**:7318-7328.

36) Y. S. Kwok, X. X. Zhang, B. Qin, K. K. Fung, *Appl. Phys. Lett.* (2000) 77:3971-3973.

37) F. Qin, N. P. Magoto, M. Garza, J. A. Kelber, *Thin Solid Films* (2003) **444**:179-188

38) S. J. Roosendaal, B. van Asselen, J. W. Elsenaar, A. M. Vredenberg, F. H. Habraken, *Surf. Sci.* (1999) **442**:329-337.

39) F. P. Fehlner, N. F. Mott, *Oxid. of Met.* (1970) **2**:59-99.

40) S. Jain, A. O. Adeyeye, S. Y. Chan, C. B. Boothroyd, *J. Phys. D: Appl. Phys.* (2004) **37**:2720-2725.

41) M. Getzlaff, J. Bansmann, G. Schönhense, *Fresenius J. Anal. Chem.* (1995) **353**:743-747.

42) F. Schedin, L. Leung, C. A. Muryn, E. W. Hill, A. Scholl, G. Thorton, *J. Appl. Phys.* (2004) **95**:7450-7452.

43) H.-Q. Wang, E. I. Altman, V. E. Henrich, *Phys. Rev. B* (2006) **73**:235418.

44) S. K. Shaikhutdinov, Y. Joseph, C. Kuhrs, W. Ranke, W. Weiss, *Faraday Discuss.* (1999) **114**:363-380.

45) V. V. Roddatis, D. S. Su, C. Kuhrs, W. Ranke, R. Schlögl, *Thin Solid Films* (2001) **396**:78-83.

46) J. A. Bardwell, B. MacDougall, M. J. Graham, *J. Electrochem. Soc.* (1988) **135**:413-418.

47) Y. Q. Cai, M. Ritter, W. Weiss, A. M. Brandshaw, *Phys. Rev. B* (1998) **58**:5043-5051.

48) A. P. Grosvenor, J. T. Francis, B. A. Kobe, N. S. McIntyre, *Surf. Interface Anal.* (2005) **37**:495-498.

49) N. Spiridis, B. Handke, T. Slezak, J. Barbasz, M. Zajac, J. Haber, J. Korecki, *J. Phys. Chem. B* (2004) **108**:14356-14361.

50) N. Spiridis, J. Barbasz, Z. Lodziana, J. Korecki, *Phys. Rev. B* (2006) **74**:155423.

51) S. J. Roosendaal, A. M. Vredenberg, F. H. Habraken, *Phys. Rev. Lett.* (2000) **84**:3366-3369.

52) M. P. Ryan, R. C. Newman, G. E. Thompson, *J. Electrochem. Soc.* (1995) **142**:L177-L179.

53) B. MacDougall, J. A. Bardwell, *j. Electrochem. Soc.* (1998) **135**:2437-2441.

54) H.-J. Freund, *Faraday Discuss.* (1999) **114**:1-31.

55) D. P. Woodruff, T. A. Delchar, "Modern Techniques of Surface Science" second edition, Cambridge University Press, (1994).

56) W. Mönch, "Semiconductor Surfaces and Interfaces" third edition, Springer, (2001).

57) S. Hüfner, "Photoelectron Spectroscopy: Principles and Applications" second edition, Springer-Verlag, Heidelberg, Germany, (1996).

58) P. J. Cumpson, M. P. Seah, *Surf. Interface Anal.* (1997) **25**:430-446.

59) S. Tougaard, *Surf. Interface Anal.* (1997) **25**:137-154.

60) C. Kittel, "Introduction to Solid State Physics" seventh edition, John Wiley & Sons, Inc., New York, (1996).

61) A. Jablonski, C. J. Powell, *Surf. Sci. Rep.* (2002) **47**:33-91.

62) N. S. McIntyre, D. G. Zetaruk, *Anal. Chem.* (1977) **49**:1521-1529.

63) S. Günther, B. Kaulich, L. Gregoratti, M. Kiskinova, *Prog. Surf. Sci.* (2002) **70**:187-260.

64) J. Stöhr, S. Anders, *IBM J. Res. Develop.* (2000) **44**:535-551.

65) Omicron Focus PEEM 402-V04 brochure, Omecron Nanotechnology GmbH, (2004).

66) M. Ohring, "The Materials Science of Thin Films" Academic Press, New York, (1992).

67) K. Uvdal, M. Lögdlund, P. Dannetun, L. Bertilsson, S. Stafström, W. R. Salaneck, A. G. MacDiarmid, A. Ray, E. M. Scherr, T. Hjertberg, A. J. Epstein, *Synth. Met.* (1989) **29**:E451-E456.

68) T. R. Dillingham, D. M. Cornelison, E. Bullock, *J. Vac. Sci. Technol. A* (1994) **12**:2436-2440.

69) H. Qiu, H. Li, K. Fang, J. Li, W. Mao, S. Luo, *Synth. Met.* (2005) **148**:71-74.

70) D. M. Cornilison, T. R. Dillingham, E. Bullock, N. T. Benally, S. W. Townsend, *Surf. Sci.* (1995) **343**:87-94.

71) R. V. Plank, N. J. DiNaro, J. M. Vohs, *Synth. Met.* (1997) **89**:1-9.

72) R. V. Plank, N. J. DiNaro, J. M. Vohs, *J. Vac. Sci. Technol. A* (1997) **15**:538-543.

73) S. C. K. Misra, M. K. Ram, S. S. Pandey, B. D. Malhotra, S. Chandra, *Appl. Phys. Lett.* (1992) **61**:1219-1221.

74) G. A. Zaharias, H. H. Shi, S. F. Bent, *Thin Solid Films* (2006) **501**:341-345.

75) F. Chen, C. Nuckolls, S. Lindsay, *Chem. Phys.* (2006) **324**:236-243.

76) B. Corraze, S. Quillard, H. Morvan M. I. Boyer, *Thin Solid Films* (2000) **372**:54-59

77) A. Riul, C. A. Mills, D. M. Taylor, *J. Mater. Chem.* (1999) **10**:91-97.

78) S. K. Pisharady, C. S. Menon, *J. Phys. Chem. Sol.* (2006) **67**:1830-1834.

79) S. Folch, A. Régis, A. Gruger, P. Colomban, *Synth. Met.* (2000) **110**:219-227.

80) Y. Wei, H. Jamasbi, S. Li, S. Cheng, S. A. Jansen, L. T. Sein, W. Zhang, C. Wang, *ACS Symposium Series* (2003) **843**:208-227.

81) M. Poncet, B. Corraze, S. Quillard, W. Wang, A. G. MacDiarmid, *Thin Solid Films* (2004) **458**:32-36.

82) W. Zhang, Y. Yu, L. Chen, H. Mao, C. Wang, Y. Wei, *ACS Symposium Series* (2003) **843**:156-165.

83) M. Evain, S. Quillard, B. Corraze, W. Wang, A. G. MacDiarmid, *Acta. Cryst.* (2002) **E58**:o343-o344.

84) W. Wang, A. G. MacDiarmid, *Synth. Met.* (2002) **129**:199-205.

85) L. Chen, Y. Yu, H. Mao, X. Lu, W. Zhang, Y. Wei, *Synth. Met.* (2005) **149**:129-134.

86) R. Schlaf, B. A. Parkinson, P. A. Lee, K. W. Nebesny, N. R. Armstrong, *J. Phys. Chem. B* (1999) **103**:2984-2992.

87) R. Schlaf, P. G. Schroeder, M. W. Nelson, B. A. Parkinson, P. A. Lee, K. W. Nebesny, N. R. Armstrong, *J. Appl. Phys.* (1999) **86**:1499-1509.

88) R. Schlaf, C. D. Merritt, L. C. Picciolo, Z. H. Kafafi, *J. Appl. Phys.* (2001) **90**:1903-1910.

89) C. Shen, A. Kahn, I. Hill, "Organic Molecular Interfaces" in Conjugated Polymer and Molecular Interfaces, Marcel Dekker, Inc., New York, (2002).

90) G. Koller, S. Berkebile, M. Oehzelt, P. Puschnig, C. Ambrosch-Draxl, F. P. Netzer, M. G. Ramsey, *Science* (2007) **317**:351-355.

91) D. Cappus, M. Haβel, E. Neuhaus, M. Heber, F. Rohr, H.-J. Freund, *Surf. Sci.* (1995) **337**:268-277.

92) P. J. Kinlen, V. Menon, Y. Ding, *J. Electrochem. Soc.* (1999) **146**:3690-3695.

93) P. J. Goodhew, J. Humphreys, R. Beanland, Electron Miscroscopy and Analysis third edition, Taylor & Francis, New York, (2001).

94) N. S. McIntyre, D. G. Zetaruk, *Anal. Chem.* (1977) **49**:1521-1529.

95) S. Tougaard, *Surf. Inerface Anal.* (1997) **25**:137-154.

96) M. P. Seah, *Surf. Sci.* (1999) **420**:285-294.

97) M. Aronniemi, J. Sainio, J. Lahtinen, *Surf. Sci.* (2005) **578**:108-123.

98) H. Höchst, A. Goldmann, S. Hüfner, *Zeit. Physik B* (1976) **24**:245-250.

99) G. K. Wertheim, S. Hüfner, H. J. Guggenheim, *Phys. Rev. B* (1973) 7:556-558.

100) E. Paparazzo, *J. Electron Spectroscopy Related Phenomena* (2006) **154**:38-40.

101) N. S. McIntyre, *Surf. Sci.* (2004) **572**:217-227.

102) P. Spellane, *Chem. Mater.* (1997) **9**:1949-1953.

103) Y. Chen, *Colloid Polym. Sci.* (2001) **279**:73-76.

104) E. Bullock, *J. Vac. Sci. Technol. A* (1994) **12**:2436-2440.

105) H. Konno, M. Inagaki, *Anal. Sci.* (1999) **15**:799-801.

106) P. Schmuki, *J. Solid State Electrochem.* (2002) **6**:145-164.

107) A. Cook, A. Gabriel, D. Siew, N. Laycock, *Curr. Appl. Phys.* (2004) **4**:133-136.